

AN ABSTRACT OF THE THESIS OF

Alexander de Moor for the degree of Master of Science in Geology presented on December 10, 2015.

Title: Local Seismicity Recorded by ChilePEPPER: Implications for Dynamic Accretionary Prism Response and Long-term Prism Evolution

Abstract approved:

Anne M. Tréhu

To investigate the dynamic response of the outer accretionary wedge updip from the patch of greatest slip during the Mw8.8 2010 Maule earthquake, 10 Ocean Bottom Seismometers (OBS) were deployed from May 2012 to March 2013 in a small array with an inter-instrument spacing of ~10 km. Nine instruments were recovered, with 4 recording data on 3 intermediate-band 3-component seismometers and a differential pressure gauge and 5 recording data from absolute pressure gauges. All instruments were also equipped with fluid flow meters to monitor the hydrologic response to fluid pressure changes within the wedge. Here we present hypocenters for 569 local events that have S-P times less than 17 seconds (i.e. within ~125 km of the array) using hand-picked arrival times and 1D velocity models derived from a 2D seismic refraction profile through the region (Moscoso et al 2011, EPSL). We analyze the distribution of seismicity in the context of published slip models, high resolution swath bathymetry, ChilePEPPER seismic reflection data, critical taper analysis done by Cubas et al 2013 (EPSL), and offshore gravity data. Based on a lack of seismicity in the outer wedge, steady state fluid flow rates at < 0.01 cm/yr, and no indications of anomalous styles of rupture such as very low frequency earthquakes, we suggest that in the study region the outer wedge is in a stable state due to localized slip to the trench that transported this region of the forearc to the west during the 2010 earthquake. This local phenomenon is probably due to the velocity weakening properties of sediments within the subduction channel at high slip rates. Based on distinct changes in the morphology of the wedge as seen in the bathymetry data and critical taper, this may be a persistent feature of this section of the margin.

© Copyright by Alexander de Moor

December 10, 2015

All Rights Reserved

Local Seismicity Recorded by ChilePEPPER: Implications for Dynamic Accretionary Prism
Response and Long-term Prism Evolution

by
Alexander de Moor

A THESIS

submitted to

Oregon State University

in partial fulfillment of
the requirements for the
degree of

Master of Science

Presented December 10, 2015

Commencement June 2016

Master of Science thesis of Alexander de Moor presented on December 10, 2015

APPROVED:

Major Professor, representing Geology

Dean of the College of Earth, Ocean and Atmospheric Sciences

Dean of the Graduate School

I understand that my thesis will become part of the permanent collection of Oregon State University libraries. My signature below authorizes release of my thesis to any reader upon request.

Alexander de Moor, Author

ACKNOWLEDGMENTS

The work presented in this thesis is due in large part to a team effort of professors, friends and family, without whom completion of this thesis would have been impossible. Firstly I would like to thank Anne Tréhu for providing the opportunity to work on this project, funding and continued guidance and support. I also need to thank Rob Harris and Eric Kirby for serving on my committee and providing me with valuable insight and discussion. In particular Rob, thank you for keeping your door open and providing support at every turn. Additionally, thank you to Vrushali Bokil for acting as my GCR.

My office mates were also crucial in my thesis efforts, both in terms of providing insight and knowledge as well as making coming into work every day an enjoyable experience. In particular Ben Murphy, Vaclav Kuna and Paria Ghorbani thank you for providing such an amazing work environment.

To all of my friends in Corvallis, thank you for making my time here incredible. I couldn't have asked for a better group of friends. I've enjoyed every second of my time with you from July 4th weekends rafting to spirited discussions around the dinner table. You have all kept me going during the hard times and smiled with me in the best times. I couldn't have done this without you.

Finally to my family, Mom, Dad, Emily and Maarten, you have always been there and I love you all. Especially to my brother Maarten who has always been a constant source of inspiration, support, knowledge and patience. Thank you for everything, I love you all.

TABLE OF CONTENTS

	<u>PAGE</u>
1 INTRODUCTION TO THE MAULE REGION AND CHILEPEPPER PROJECT	1
1.1 ChilePEPPER	1
1.1.1 Instrumentation	2
1.2 Regional Geology and Tectonics.....	2
1.3 Previous Studies	4
1.3.1 Review of slip models	4
1.3.2 Aftershock studies	5
1.4 Purpose of Study.....	6
2 LOCAL SEISMICITY	15
2.1 Introduction.....	15
2.2 Verification of OBS timing and polarity	15
2.3 Velocity model and station delays	15
2.4 V _p /V _s ratios.....	16
2.5 Hypocenter Locations.....	16
2.6 Bias in Catalog locations.....	18
2.7 T-phases	19
2.8 Development of a Relative Magnitude Scale using Coda Lengths	19
2.9 Magnitude of Completeness and b-value.....	21
2.10 Very Low Frequency Events	21
2.11 Fluid Flow Measurements	22
3 ANALYSIS OF BATHYMETRY IN THE NORTH MAULE REGION	34
3.1 Introduction.....	34
3.1.1 Data.....	34
3.2 North Maule	34
4 GRAVITY.....	43
4.1 Introduction.....	43
4.2 Method	43
4.2.1 Grid Preparation	44

TABLE OF CONTENTS (CONTINUED)

	<u>PAGE</u>
4.2.2 PRISM Code.....	44
4.3 Case Study: Maule Region.....	45
5 DISCUSSION AND CONCLUSIONS.....	50
6 BIBLIOGRAPHY.....	58
7 APPENDIX A.....	64
8 APPENDIX B.....	76
9 APPENDIX C.....	78

LIST OF FIGURES

	<u>PAGE</u>
Figure 1-1: A) ChilePEPPER array with approximate inter-instrument spacing of 10 km.	8
Figure 1-2: Top panel: Simplified sketch of morphology of the accretionary prism adapted from Lieser (2015).....	9
Figure 1-3: Station locations for ChilePEPPER (red and white triangles) and CGO05 (blue triangle) overlain on bathymetry (A) and free air gravity (B) with 10m and 15m slip contours from Moreno et al (gray).....	10
Figure 1-4: Three types of models for the Maule region.	11
Figure 1-5: Structure and P-wave velocities of the Maule Accretionary wedge from Moscoso et al (2011) with the 1-D velocity model inputs for Hypo71 (from red lines) for events in the outer rise (left) and events in the accretionary wedge (right).....	12
Figure 2-1: Cross correlation of waveforms for events from Colombia.....	24
Figure 2-2: Plot of CP10 residuals during the ChilePEPPER deployment.	24
Figure 2-3 Number of picks used for locations. Of the 569 events presented, 386 events had < 6 picks.....	25
Figure 2-4: V_p/V_s , depth, RMS plot for the September 15th 00:40 (ML 4.7 event).....	25
Figure 2-5 All events located by the ChilePEPPER array (events with < 5 picks shown as open circles) scaled by coda length magnitude.....	26
Figure 2-6 Well constrained events from the ChilePEPPER deployment.	26
Figure 2-7 Events showing systematic depth bias in the NEIC (gray dots) and local (red dots) catalogs.	27
Figure 2-8 First motion plots for the September 15 th sequence.	27
Figure 2-9: A: Events with well-defined t-phases colored by the number of picks used in the location.	28

LIST OF FIGURES (CONTINUED)

	<u>PAGE</u>
Figure 2-10 Method of magnitude calculation. Upper panel shows unfiltered seismogram from which coda start time is recorded.....	29
Figure 2-11: Coda Magnitude calibration from GO05. Coda Lengths (s) plotted against bulletin magnitudes. $R^2 = 0.84$	30
Figure 2-12 Magnitude of completeness calculated from the goodness of fit test shows a M_c of 3.6 (left) while the frequency magnitude distribution, and associated b-value is shown on the right.....	30
Figure 2-13: Haida Gwaii tsunami captured on ChilePEPPER Absolute Pressure Gauges.....	31
Figure 2-14 Flow meter results from the ChilePEPPER deployment.....	32
Figure 3-1 High resolution swath bathymetry of the North Mule area.....	37
Figure 3-2 Examples of features seen along the Chilean margin.	38
Figure 3-3 (Top panel) Close up of study area with features in the bathymetry outlined.	39
Figure 3-4 Morphology of incision in deformation front at -35S (top panel).	40
Figure 3-5 Multi Channel Seismic reflection data showing transition from sediment accretion (top panel) to sediment subduction (bottom panel) over the course of a few kilometers.....	41
Figure 3-6 Same as 4-1 with features outlined in the North Maule segment.....	42
Figure 4-1: 2-D Schematic of the topographic correction applied onshore and offshore (A).	47
Figure 4-2: a) Original free-air gravity data downloaded from Geomapapp.	48
Figure 4-3 A) Terrain and slab corrected bouguer gravity anomalies for the Maule region.	49
Figure 5-1 Distribution of seismicity from Lieser (2015) on TCBGA (A) and bathymetry (C) with critically tapered sections of the outer accretionary wedge from Cubas et al., (2013) highlighted in red.....	55
Figure 5-2 Topographically and slab corrected gravity anomalies with overlain slip contours from Moreno et al., (2010).....	56

LIST OF FIGURES (CONTINUED)

	<u>PAGE</u>
Figure 5-3: Comparison of Complete gravity correction (left) and high resolution swath bathymetry (right).....	57
Figure 7-1 Two events $> M_{\text{coda}} 3$ recorded on the ChilePEPPER array not previously described in the Chilean seismic bulletin.	66
Figure 7-2 Signal quality problems at site CP08 on the horizontal (A) and vertical (B) components during an event occurring on Jan 27.	67
Figure 7-3 Showing P and S-wave arrivals at station CP08.....	68
Figure 7-4 Event on September 15 th recorded at station CP06.....	70
Figure 7-6 Typical waveform of event located in the outer rise that excites a high frequency T-phase.	71
Figure 7-7 M_L 3.4 event located below the ChilePEPPER array.....	72
Figure 7-8 Spectrum from earthquake shown in figure 7-6.	73
Figure 7-9 Example of distantly sourced Rayleigh waves from a M4.7 event in Tonga at the same frequency band of Very Low Frequency events.....	74
Figure 7-10: Vertical components and APG recordings of September 15th 00:40 event low-pass filtered at 1Hz	74
Figure 7-11 Vertical components and APG recordings of September 15th 00:50 event low-pass filtered at 1Hz	75

LIST OF TABLES

	<u>PAGE</u>
Table 1-1 Summary of data recovery for the ChilePEPPER deployment (Tréhu and Tryon 2012)..	13
Table 2-1 Events used to determine if timing issues were present in well recording stations.....	32
Table 2-2 Results from cross-correlation of waveforms relative to CP06. For CP01, CP04, and CP09 correlation stays the same for all events.	33
Table 2-3: Locations and depths of well-located events from the National Earthquake Information Center (NEIC), Chilean Seismic Network (CSN) and ChilePEPPER (CPEPP) demonstrating differences in hypocentral locations.....	33
Table 8-1: List of all events with identifiable T-phases seen in ChilePEPPER data set.....	77
Table 9-1 Table describing where in the dataset VLF waveforms were seen.....	79

1 INTRODUCTION TO THE MAULE REGION AND CHILEPEPPER PROJECT

1.1 ChilePEPPER

On February 27, 2010 a M_w 8.8 earthquake ruptured the central Chilean margin. This event filled a well-documented seismic gap between $\sim 38^\circ\text{S}$ and 32.5°S . The data available for this event have led to a number of possible slip models. While the models differ in details, a common feature of the models is that the patch of highest slip ($\sim 16\text{m}$) occurred to the NW of the epicenter (Figure 1-1). A point of debate, however, is whether slip propagated to the trench [Yue *et al.*, 2014] or halted prior to reaching the trench [e.g. Moreno *et al.*, 2010; Lay *et al.*, 2010, Delouis *et al.*, 2010; Tong *et al.*, 2010; Lorito *et al.*, 2011]. Failure of the rupture to reach the trench is suggested by a lack of aftershocks in a band between 0 and 25 km downdip of the trench, as well as inverse modeling of onshore GPS and InSAR data. Absence of seismic activity within the prism during the aftermath of the earthquake, in conjunction with a lack of detectable bathymetric change (within 5m of error) of the accretionary wedge a month after the event [Chadwell *et al.*, 2010] suggested alternate methods of strain release within the sedimentary prism.

It has generally been thought that slip does not propagate all the way to the deformation front due to the velocity strengthening rheology of the plate boundary beneath the outer accretionary wedge (figure 1-2) and internal prism strength [Lallemant *et al.*, 1994; Wang and Hu, 2006]. This results in a co-seismic stress drop on the plate boundary along the downdip velocity weakening regime and a stress state increase within the outer accretionary wedge (figure 1-2). The state of stress within the outer wedge should slowly decrease during the interseismic in the form of dynamic deformation. This led to the main hypothesis of ChilePEPPER (Project Evaluating Prism Post-Earthquake Response) that the wedge accommodates increased stress from the $\sim 16\text{m}$ of slip down dip through deformation by slow earthquakes, micro-seismicity, and fluid expulsion, to redistribute pore-fluid and fluid pressure [Tréhu & Tyron., 2011]. It was hypothesized that the post-earthquake change in the stress state of the prism would induce pore pressure variations resulting in fluid flow within near surface sediments. If measured, this could provide a first order estimation of local strain that, when coupled with local seismicity, could constrain spatial and temporal variations within the prism as it accommodated the sudden change in stress state.

In order to capture the dynamic response, 10 Ocean Bottom Seismometers (OBS) equipped with 3 intermediate-band 3-component seismometers, pressure gauges and Chemical Aqueous Transport (CAT) meters were deployed up-dip of the region of greatest slip (figure 1-1). Instruments were arranged in a small array with an inter-instrument spacing of ~10km and recorded data from May 2012 to March 2013 as part of ChilePEPPER. High-resolution bathymetric and multi-channels subsurface imaging data were also acquired.

1.1.1 Instrumentation

ChilePEPPER utilized 10 instruments from the Lamont-Doherty Earth Observatory (LDEO) group as part of the Ocean Bottom Seismograph Instrument Pool (OBSIP). 5 OBS packages (SL-OBS) were outfitted with a 3-component L4C 1 Hz geophone with a low-noise amplifier and a differential pressure gauge (DPG). The other 5 (CI-OBS) each contained a Trillium Compact seismometers and Paroscientific absolute pressure gauges (APG). Seismometers and DPGs recorded at 40sps while the APGs recorded at 125 sps. Of the 10 OBS packages, all but CP05 were recovered during cruise PS1306 from March 15-21, 2013. The SL-OBS (sites CP06-CP09) performed generally well. Estimated data recovery for these instruments was ~75% with stations CP06 and CP09 operating 100% of the time, with sites CP07 and CP08 recording sporadically ~50% of the deployment (Figure 1-1).

For the CI-OBS data (sites CP01-CP04 and CP10), overall data recovery was ~25% for the ChilePEPPER objectives because of a systematic error in the leveling of the seismometers which led to no data recorded on the trillium compact seismometers. Additionally, APGs at sites CP02 and CP03 became clogged and lost sensitivity to seismic frequencies at day 100 (CP02) and day 10 (CP03) of the deployment. APGs at sites CP01, CP04 and CP10 record well below 2Hz, which is adequate for large local earthquakes and teleseismic events, but smaller events fail to rise above the noise level for these instruments. A data summary is located in table 1-1.

1.2 Regional Geology and Tectonics

The western boundary of the South American plate is characterized by subduction of the Nazca plate below the South American plate, forming the Peru-Chile trench (Figure 1-3). Historically, it is

the most seismically active subduction zone in the world, typically nucleating events greater than magnitude 8 roughly every ten years [Campos *et al.* 2002] with three since 2010. The rapid seismic cycle and along trench variability in sediment subduction, strain partitioning, gravity anomalies and incoming plate topography make this region a natural laboratory for understanding seismogenesis. In addition, long historical records allow for the determination of seismic segments (zones that repeatedly rupture the same areas throughout time) [Lomnitz, 2004; Comte and Pardo, 1991]. While our understanding of seismic segmentation is still evolving, proposed causes include subducting ridges and seamounts [Contreras-Reyes *et al.*, 2011], significant features in the overriding plate (e.g. peninsulas and bends in the coastline) [Loveless *et al.*, 2010], and variations in sediment subduction and thickness [Ruff, 1989,]. Segmentation is sometimes inferred from trench parallel gravity anomalies [Song and Simon 2003., Wells *et al.* 2003], and gradients in the gravity field [Loveless *et al.* 2010].

The Constitución-Concepción segment in south central Chile is bounded to the south by the rupture zone of the 1960, Mw 9.5 event, and to the north by the rupture zones of the 1985 Valparaiso earthquake and, most recently, the September 16, 2015 Mw 8.3 Illapel earthquake. The 100 km x 500 km region that ruptured during the Maule earthquake was a well-documented, mature seismic gap with the last recorded large event (M ~8.5) occurring in 1835 [Ruegg *et al.*, 2009]. This region is characterized by subduction in a N78°E direction at a current rate of 66mm/yr [Angerman *et al.*, 1999]. High sedimentation rates linked to deglaciation and erosion of the Andes mountains since the Pliocene [e.g. Kukowski and Oncken, 2006] and blocking of sediment transport to the north by the Juan Fernandez ridge [Contreras-Reyes 2011] has led to the construction of an accretionary prism composed primarily of plagioclase, feldspar and quartz with occasional interbedded ash layers [Mix *et al.* 2003].

Episodic phases of trench sediment accretion and erosion along the south-central Chilean margin have led to along strike variability within the accretionary wedge, resulting in widths of 5-50km and thicknesses of up to 20 km [Contreras-Reyes *et al.*, 2010, Bangs and Cande, 1997]. A wedge approximate 20-50 km with a subduction channel thickness <1km characterizes the northern Maule prism [Moscoso *et al.*, 2011, Schewarth *et al.*, 2009]. Continental basement extending seaward from beneath the shelf, likely composed of a paleo-accretionary complex, acts as a backstop for the accretionary prism [Contreras-Reyes *et al.*, 2010, Moscoso *et al.*, 2011]. While regional scale along strike

variability in sediment accretion vs. subduction is typical of this section of the margin, more localized variations are also noted in seismic reflection data acquired during ChilePEPPER with transitions occurring over a few kms [Trébu and Tyron 2012].

On February 27, 2010 this segment ruptured in a Mw 8.8 low angle thrust earthquake that nucleated at $\sim 36^\circ\text{S}$ with rupture propagation to the north and south affecting nearly 500 km of the Chilean coast [Vigny *et al.*, 2011; Moreno *et al.*, 2012]. Most slip models agree that the main slip patch (up to 16m) occurred to the North between -34°S and -35.5°S [e.g. Delouis *et al.*, 2010; Tong *et al.*, 2010; Yue *et al.*, 2014]. This event triggered a tsunami, which reached the coast in less than 20 minutes with wave-heights reaching up to 14 m [Vargas *et al.*, 2011] leading to significant destruction throughout the Maule region. Due to the high societal impact and the extensive amount of data available for this event, multiple studies have been conducted to understand the dynamics of this event.

1.3 Previous Studies

1.3.1 Review of slip models

The M_w 9.0, 2011 Tohoku earthquake shed new light on the range of possible slip distributions along megathrust faults. Generally, modeled slip during megathrust events failed to propagate to the trench. However, the Japanese event demonstrated that slip to the trench is possible and poses a significant seismic hazard in the form of tsunami generation. This requires consideration of slip to the trench for older events, such as the 2010 Maule earthquake. Slip for the Mw 8.8 Maule event is fairly well constrained downdip based on continuous GPS and InSAR data and shows that ~ 500 km of the Chilean coastline ruptured bilaterally from the hypocenter, with main slip patches occurring to the north and the south [Tong *et al.*, 2010, Pollitz *et al.*, 2011, Vigny *et al.*, 2011, Moreno *et al.*, 2012]. For these geodetically derived models, patterns of slip distribution along strike are generally comparable. While most slip models show slip being arrested updip prior to reaching the trench, the extent of slip propagation is still strongly debated.

The model of Lin *et al.* (2013) embodies the first group of models, which show slip halting down dip of the trench (figure 1-4). Inverting seismic, geodetic and tsunami data they concluded that slip did not propagate through the shallowest 15-20 km of the megathrust. This was interpreted

to indicate that the upper portion of the fault slips aseismically during the interseismic period. The second group of models use geodetic data only and reveal slip propagating to within 5-10km of the trench [Moreno *et al.*, 2012, Tong *et al.*, 2010, Vigny *et al.*, 2011]. However, use of onshore data exclusively provides poor resolution near the trench.

The two models that predict >10m of slip to the trench locally along the portion of the slip plane updip from the patch of greatest slip are Koper *et al.* (2012) and Yue *et al.* (2014). The Koper *et al.* model uses only teleseismic body waves while the model by Yue *et al.* (figure 1-4) requires a complex correction to the tsunami Green's function in order to accurately approximate tsunami arrival times at DART buoys.

Heterogeneity in datasets used by different authors make slip models difficult to compare; however, most note that resolution near the trench is poor as demonstrated by checkerboard tests. Understanding whether slip propagated to the trench is important for understanding aftershock distribution, frictional properties of the megathrust, forearc structure of the region, effects of subducting topography, and future seismic hazard assessment. The disparity among slip models, especially near the trench, is one of the driving factors of the ChilePEPPER project. A description of the data used for each slip model is provided in table 1-2.

1.3.2 *Aftershock studies*

As part of a RAPID response to the Maule event, IRIS, in collaboration with seismologists from Europe and Chile, deployed a 164-station temporary array for seven months to monitor aftershock activity. These sensors included 48 short period and 91 broadband seismometers, along with 25 accelerometers installed along the entire rupture zone with station spacing less than 30 km [Russo *et al.*, 2011]. Additionally GEOMAR deployed 30 OBSs from September through December 2010 leading to an unprecedented amount of data for the immediate aftermath of the megathrust event. Over 100,000 aftershocks have been located and more than 400 focal mechanisms have been constructed for this time period [Beck *et al.*, 2014, Agurto *et al.*, 2012, Hayes *et al.*, 2013, Rietbrock *et al.*, 2012]. These events reveal that most seismic activity occurs either as outer rise normal faulting seaward of the deformation front or between 40 and 140 km landward of the deformation front, likely associated with inter-plate faulting as indicated by hypocentral depths and focal mechanisms

[*Rietbrock et al.*, 2012]. Aftershocks landward of the deformation front generally occurred in areas of high slip gradient (rapid transitions from high to low slip when compared to the slip model of *Moreno et al.* (2010)).

Some upper plate deformation in the region is interpreted from normal faulting (generally $M_w < 4$). Though most are correlated to the M_w 6.9 Pichilemu aftershock at the northern extent of the rupture zone [*Agurto et al* 2012]. This is further revealed in the study of *Lange et al* (2012), which provides normal faulting moment tensor solutions for intraplate events occurring in this area. *Lieser et al.* (2014) suggest that aftershock seismicity reveals splay fault activation in this area, although preliminary results from full waveform analysis suggest these events may occur on the plate interface (Sebastian Carrasco, Universidad de Chile).

A subducting seamount near the hypocenter of the earthquake has been interpreted from a high P-velocity anomaly near the coast [*Hicks et al.*, 2012]. This feature may have caused frictional heterogeneities on the plate interface that restricted localized slip but promoted the initial nucleation of the Maule event. Other local density and gravity anomalies have also been correlated to the highest slip patch suggesting that subducting or obducted seamounts may act as asperities [*Maksymowicz et al.*, 2015].

Cubas et al (2013), *Maksymowicz et al* (2015) and *Maksymowicz* (2015) have estimated the basal friction using Coloumb wedge theory and have concluded that the frictional coefficient was lower on the patch of highest slip. The hypothesis that high slip and low basal friction are correlated is consistent with studies along other subduction margins e.g. Hikurangi [*Fagerang et al* 2011] and Tohoku [*Cubas et al* 2013].

1.4 Purpose of Study

The primary objective of this study is to use local seismicity recorded on the ChilePEPPER OBS array to understand the dynamic response of an accretionary prism in the aftermath of a megathrust event. Additionally, we hope to place the seismicity into a geologic context using gravity data corrected for the effects of bathymetry and the subducting slab. Due to instrumental limitations for studying events offshore, many questions remain unanswered about the accretionary prism, its role in seismicity, and its interactions with the subducting plate. In this study we hope to add to the

scientific knowledge of megathrust events by addressing these questions: How does the accretionary wedge respond to the stress changes induced by a large megathrust event? How do small-scale variations in sediment subduction affect local seismicity? Is there a correlation between gravity anomalies, slip during an earthquake, and local seismicity? Did slip reach the trench during the 2010 Maule earthquake?

The instrumentation and data provided by ChilePEPPER allow insight into some of these questions. A small aperture array was deployed over the outer region of the accretionary wedge where the greatest post-earthquake stress perturbation was expected. The array included flow meters, seismometers, and pressure gauges. This provided the ability to locate 569 local events and place them into a geologic context to help understand this complex geologic system.

Section 2 focuses on the location methodology and distribution of hypocenters with S-P times less than 17 seconds (i.e. within ~ 125 km of the array). These events were located using handpicked arrival times and 1D velocity models derived from a 2D seismic refraction profile through the region (figure 1-5). Additionally, a search for anomalous styles of rupture was conducted by looking for low frequency events within the dataset to see if post-earthquake relaxation was being accommodated in this manner. In the low frequency bands the only recorded events were attributed to distantly sourced rayleigh waves from other circum-pacific earthquakes and the long period wave associated with the Haida Gwaii tsunami.

In order to place the distribution of events in a geologic context we provide an analysis of high-resolution bathymetry and of topographically corrected Bouguer gravity anomalies (TCBGA) [sections 3 and 4 respectively]. The TCBGA is a refined method for offshore gravity processing, which corrects for the effects bathymetry and removes long-wavelength gravity anomalies assumed to be produced by the subducting slab. The free-air gravity signal over the continental margin is dominated by these two effects, obscuring anomalies that result from structures within the upper plate or from topography on the subducting plate. By removing these effects the relationship between geologic structure, megathrust earthquake slip and local seismicity is highlighted. Using these datasets, along with published slip models and previous analyses of critical taper of the outer wedge, we demonstrate that in our study region slip likely propagated to the trench and that it may be a recurring feature in this section of the margin.

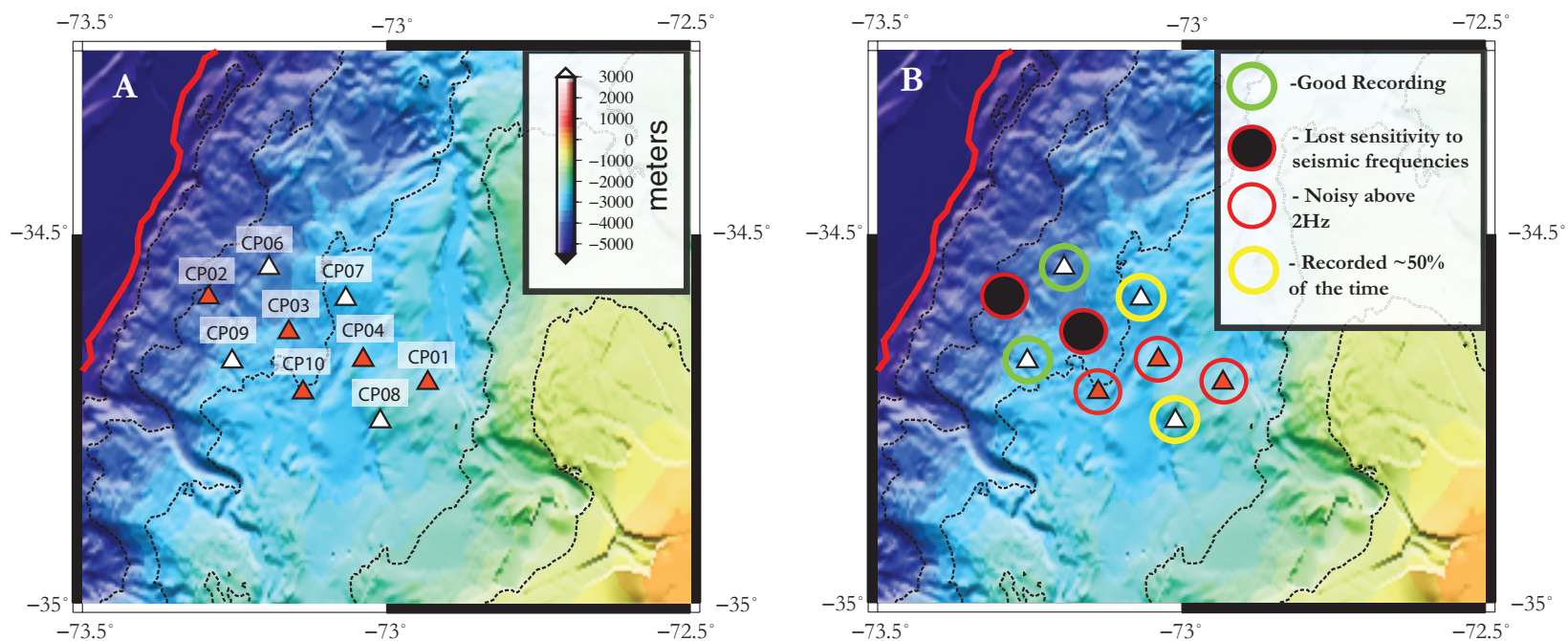


Figure 1-1: A) ChilePEPPER array with approximate inter-instrument spacing of 10 km. Two different types of OBS packages were used. The first were outfitted with a 3-component LAC 1 Hz geophone with a low-noise amplifier and a differential pressure gauge (DPG) [White triangles]. The others each contained a Trillium Compact seismometer and Paroscientific absolute pressure gauges (APG) [Red triangles]. B) Schematic showing approximate data recovery for each instrument. Note that the Trillium Compact seismometers (red circles) failed to record any data, and APGs were noisy above 2 Hz. OBS CP05 was not recovered and is not shown here. Over the course of deployment stations CP02 and CP03 became clogged and lost sensitivity to seismic frequencies. CP03 lost sensitivity ~10 days after deployment, while CP02 recorded for ~100 days. For a detailed description of data recovery see table 1-1.

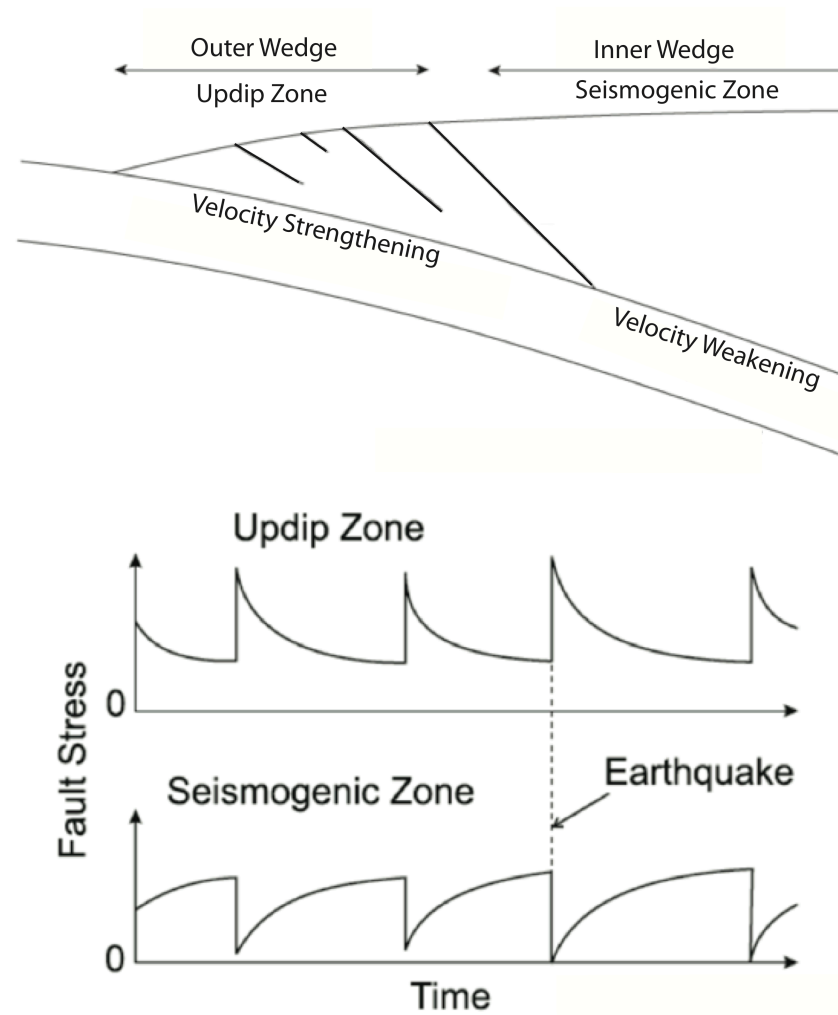


Figure 1-2: Top panel: Simplified sketch of morphology of the accretionary prism adapted from Lieser (2015). Bottom panel: Schematic of fault stress through multiple seismic cycles. The updip zone (outer wedge) demonstrates an increase in fault stress during/ immediately after an earthquake while the downdip seismogenic zone has a coseismic stress drop (from Hu and Wang 2006).

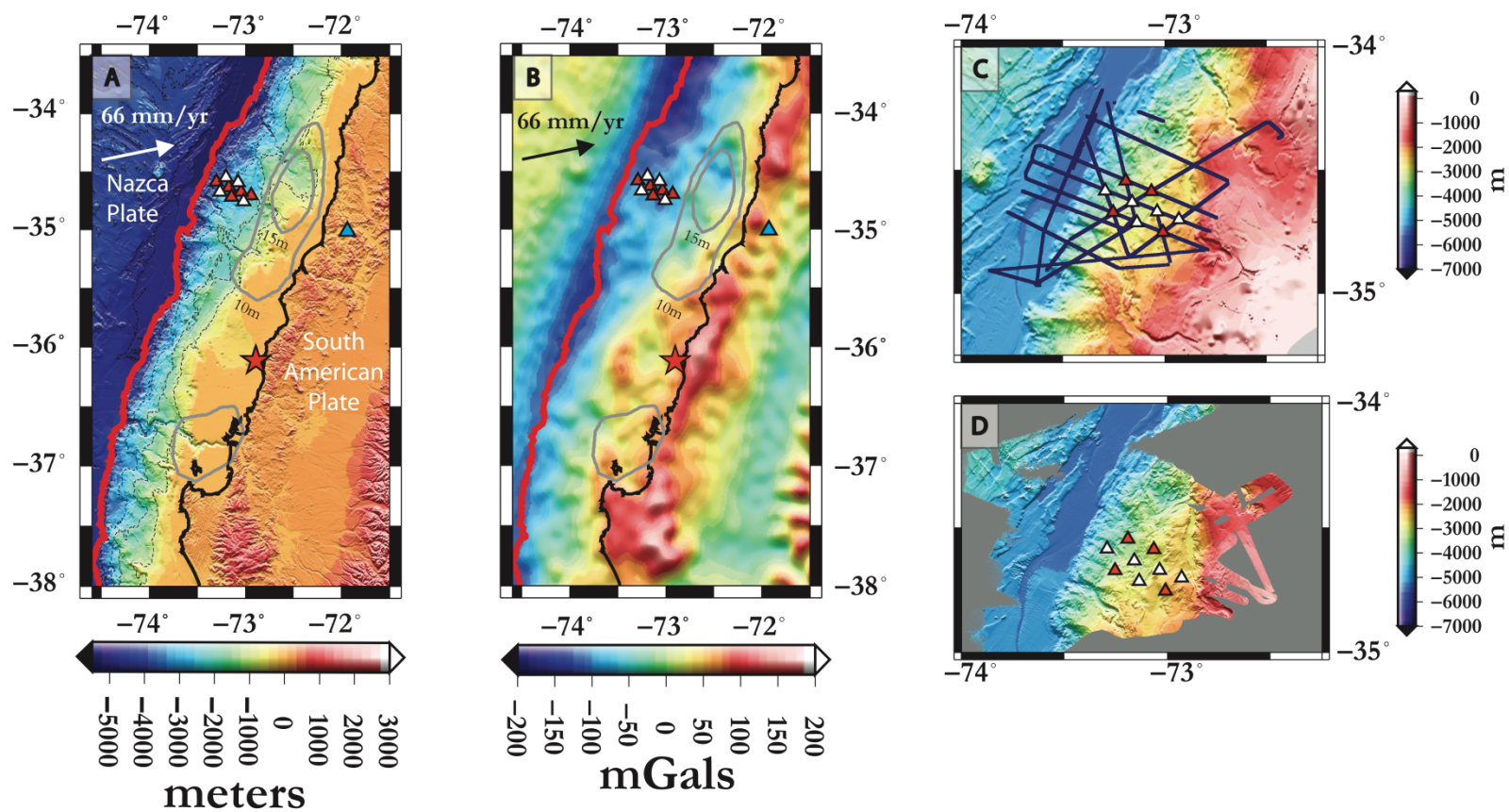


Figure 1-3: Station locations for ChilePEPPER (red and white triangles) and CGO05 (blue triangle) overlain on bathymetry (A) and free air gravity (B) with 10m and 15m slip contours from Moreno et al (gray). The red star designates NEIC epicenter. Black lines represent the coastline while bold red line represents the deformation front. Shot line locations are shown in (C) right and newly acquired swath bathymetry shown bottom right.

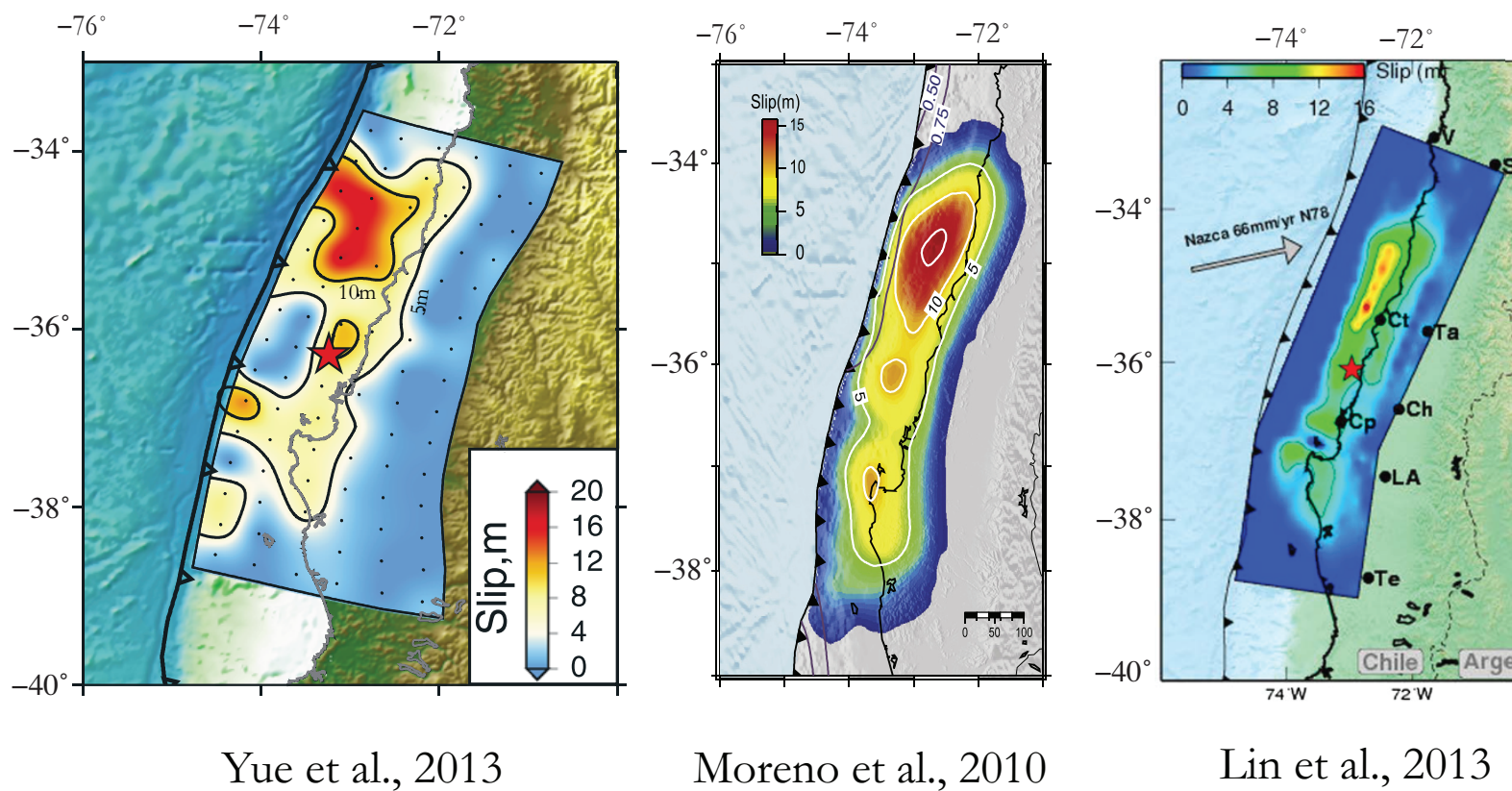


Figure 1-4: Three types of models for the Maule region. Left: Yue et al using geodetic, body wave and tsunami data showing 15 m of slip to the trench. Middle: Moreno et al showing <5m of slip to the trench and (right) Lin et al which shows slip stopping down dip of the trench.

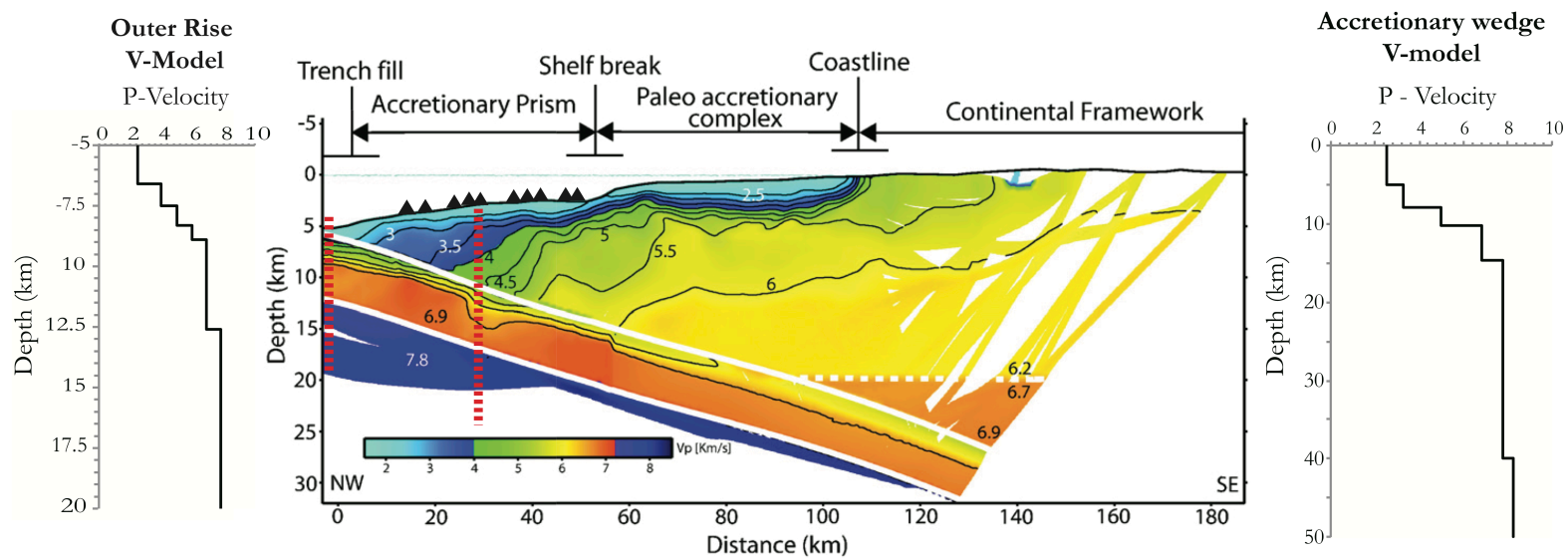


Figure 1-5: Structure and P-wave velocities of the Maule Accretionary wedge from Moscoso et al (2011) with the 1-D velocity model inputs for Hypo71 (from red lines) for events in the outer rise (left) and events in the accretionary wedge (right). ChilePEPPER OBS array in black triangles.

Site	Type	Z	H1	H2	APG	DPG	Comment
S01	CI	nd	nd	nd	50%	na	No seismometer data. APG data good for frequencies below 2 Hz.
S02	CI	nd	nd	nd	30%	na	No seismometer data. APG data not sensitive to seismic frequencies because of blocked tubing after day 230, 2012.
S03	CI	nd	nd	nd	10%	na	No seismometer data. APG data not sensitive to seismic frequencies because of blocked tubing after day 150, 2012
S04	CI	nd	nd	nd	50%	na	No seismometer data. APG data good for frequencies below 2 Hz.
S05	SL	nd	nd	nd	na	nd	Instrument not recovered.
S06	SL	100%	100%	100%	na	80%	Seismometer data quality is good. Quality of DPG signal deteriorates by day 048 2013.
S07	SL	50%	50%	50%	na	50%	Signal has intermittent offsets, drop outs and zeros on Z and DPG. Data quality deteriorates with time. Roughly 50% of the data are useful.
S08	SL	50%	50%	50%	na	80%	Sensor ball was partially flooded. Seismometer and DPG signal quality deteriorates with time.
S09	SL	100%	100%	100%	na	75%	Many data dropouts and offsets on the DPG data. Roughly 75% of the data are useful.
S10	CI	nd	nd	nd	50%	na	No seismometer data. APG data good for frequencies below 2 Hz.

CI - Cascadia Initiative design with Trillium Compact seismometers and APGs.

SL - "Standard" LDEO OBS with L4C seismometers and DPGs.

na - not applicable

nd - no data

Table 1-1Ta Summary of data recovery for the ChilePEPPER deployment (Trébu and Tryon 2012)

	hr-GPS	cGPS	Campaign GPS	InSAR	Teleseismic Body Waves	Coastal Leveling	Tsunami Modeling	Slip to Trench?
Author								
<i>Moreno et al 2012</i>		x	x	x		x		~5m above patch of greatest slip
<i>Yue et al 2014</i>	x		x	x	x		x	>12m
<i>Vigny et al 2011</i>		x	x			x		Unresolvable
<i>Lorito et al 2011</i>		x		x		x	x	No
<i>Delouis et al 2010</i>	x	x		x	x			<5m
<i>Lin et al 2013</i>		x	x	x	x	x	x	No
<i>Koper et al 2012</i>					x			>10 m
<i>Tong et al 2010</i>		x		x	x			No
<i>Pollitz et al 2011</i>		x		x				No

Table 1-2 : Summary of data used in slip models from multiple authors

2 LOCAL SEISMICITY

2.1 Introduction

Examples of seismic data recorded during deployment of the ChilePEPPER array, and discussions of some data quality issues faced are provided in Appendix A.

2.2 Verification of OBS timing and polarity

To verify timing on instruments we used four large, deep teleseismic events (Table 2.1). Deep events were chosen because of simple wave-forms and steep incident angles. These four events are paired, two from Argentina, two from Colombia with similar depths and span most of the duration of the ChilePEPPER deployment. Unfortunately only 5 stations recorded all four events, and well-recorded S-waves are present for only one event. Using cross-correlation of waveforms from these events, bandpass filtered at 0.1-1Hz (Figure 2-1), it was determined that APG CP10 contained a timing error (Table 2.2). This was confirmed by examining P-residuals at CP10 using Hypo71 (*Lee et al.*, 1972) and a preliminary set of hypocenter solutions. Clock drift for this instrument is calculated to be 0.4s every 100 days. This was corrected for by adding timing corrections to CP10 picks based on the equation in figure 2-2. Interestingly, station residuals decrease in time during the deployment. Possible causes for the initial 1.5s offset is human error when setting the timing during instrument deployment.

Average residuals for stations other than CP10 were checked from Hypo71 output based on monthly calculations and were seen to contain no systematic variability throughout the deployment and vary by less than < 0.2 s suggesting that there were no timing drifts for other stations. Instrumental polarity was checked using the same teleseismic events discussed above. All of the APGs had inverted polarities from the other instruments and have been multiplied by -1 to correct for this.

2.3 Velocity model and station delays

To correct for differences in station depth I applied station delays. In order to apply this method to the ChilePEPPER deployment, the top of the velocity model was placed at the mean depth of the stations (2870m). Station delays were then calculated by:

(mean station altitude - station altitude)/velocity of top layer (km/s)

For these station delays it is assumed that the incident angle for the ray paths is vertical. This imparts uncertainty to events that enter the array at low angles of incidence with few picks.

2.4 V_p/V_s ratios

While P-velocities are well constrained for the study area, little is known about S-wave velocities for the outer accretionary prism of the Maule region. As many of our events contained fewer than six phase picks (figure 2-3), generally composed of both P and S wave arrivals, constraining S-wave velocities within our array was necessary in order to limit uncertainty in hypocenter locations. In order to do this we used the September 15th 00:40 (M_L 4.7) event, which had a preliminary bulletin location below the ChilePEPPER array. This event was used because it had P and S-wave arrivals on all functioning stations (8 P -wave arrivals and 4 S-wave arrivals). This event was located in Hypo71 with fixed depths and varying V_p/V_s ratios. The absolute minimum RMS in the location for this event was determined at V_p/V_s 2.2 (Figure 2-4).

This ratio is qualitatively confirmed by corrections applied to stations located on the accretionary wedge by *Lieser* (2015), which required up to a full second of delay when using a standard V_p/V_s ratio of 1.67. This suggests that the array was distributed across a zone of poorly consolidated, highly saturated sediments, consistent with outer accretionary prism materials composed of silty clay. This is corroborated further by extremely low amplitude to negligible S-wave arrivals of small local events at most stations (e.g figure 7-4) and are consistent with V_p/V_s ratios found in cores from the Nankai accretionary wedge [*Hashimoto et al.*, 2011].

2.5 Hypocenter Locations

Using a 1D velocity model, a V_p/V_s ratio of 2.2 as determined from the previous analysis, and a starting depth of 8km (reasoning in section 2.6), we located 569 events within ~125 km of our array (figure 2-5). To help constrain hypocentral depths for the outer-rise, preliminary epicenters west of -73.2°W were extracted and re-run in Hypo71 using a 1-D velocity model better suited to that location (figure 1-3) and a V_p/V_s ratio of 1.78.

Events located outside of the array contain high degrees of uncertainty from effects of the 1D velocity model, poor azimuthal coverage and regional geologic structure. Using few picks for the location may exacerbate this error. The number of picks used for locations is shown in figure 2-3. Despite high uncertainty, epicentral locations produce the same pattern seen in aftershock locations [Lieser 2015] with an aseismic patch north of the array bounded to the north by a NW-SE trending zone of seismicity offshore of Pichilemu as well as a lack of well-constrained seismicity within the outer accretionary wedge. The fact that the patch of aseismicity persists for three years after the Maule earthquake is notable.

In order to determine well-located hypocenters, events were filtered based on Hypo71 output. Only events with greater than 5 picks, root mean square (RMS) error < 1.0 , and horizontal errors of < 20 km were used. To determine the stability of the solution these events were re-run using a starting depth of 13km to see if they would converge to the same locations. Events that converged to within 15km of the initial location were kept. These were then matched to coda length magnitudes, though $\sim 1/3$ of events were not recorded at station GO05, or had poorly formed codas and a magnitude could not be applied, and are plotted in figure 2-6.

Nine events cluster between -72.8°W and -73°W directly south east of the array (figure 2-6). The events range in magnitude from M_{CL} 1.7 to 4.3 and tend to cluster along the plate boundary, though some locate within the upper plate with hypocentral depths up to 5.5 km. It should be noted that events above the plate boundary contain five picks (four P and one S) and depth errors for these events exceeds 10 km.

28 well-constrained events locate within the outer rise with a maximum M_{CL} 3.6 associated with an event occurring on March 12th 2012. Due to the aperture and location of the array, uncertainty in hypocentral depths associated with these locations is high and lack of multiple S picks once again limits depth resolution. However, the March event has a depth error of < 4 km with multiple phase picks and will be discussed in section 2.6. Events in the outer rise are likely associated with normal faulting caused by bending of the subducting slab. Also notable is the lack of well-constrained seismicity between -73.1°W and -73.4°W , an extent of ~ 33 km downdip from the deformation front. This aseismic portion is consistent with the distribution of aftershocks as shown by *Moscoso et al* (2012) and *Lieser* (2015) that distinguished a 40km section downdip of the trench containing significantly fewer aftershocks than within the outer rise or further down-dip.

2.6 Bias in Catalog locations

It has been noted offshore of Oregon that hypocentral depths in published catalogs based only on onshore stations are systematically biased towards deeper depths [Williams *et al*, 2011, Trèbu *et al* 2015]. To test the accuracy of catalog events located in the outer wedge of Chile we used the ChilePEPPER array and a 1-D velocity model based on the seismic refraction line from Moscoso *et al* (2012) which best represents the structure below the mid-point of the array (figure 1-3). A pair of events occurring on 15 September at 00:40 (M_b 4.7) (figure 7-10) and at 00:50 (M_b 4.5) (figure 7-11) had preliminary locations in the NEIC catalog on the eastern edge of the array and were well recorded on ChilePEPPER instruments (table 2-3).

In order to constrain best initial conditions for locations for these events we ran the inversion with fixed depths and plotted RMS values (Figure 2-7). Local minima occurred for both events at 8km depths. They were then located allowing freedom in both depth and the horizontal at a starting depth of 8 km giving final depths of 7.42 km and 7.56 km respectively with an RMS of <0.1 . This represents a 40km shift to the SW and a decrease in depth of 26km for the 00:40 event and a 13 km shift SW and 18.84 km decrease in depth for the 00:50 event. S-P times from onshore station GO05 vary by less than 0.2s confirming that events should locate within a few kilometers of each other.

The local event catalog produced by the Chilean seismic network also lists two events well recorded by the ChilePEPPER array. They occurred at 18:15 (M_L 3.6) on 12 May and 02:31 (M_L 3.4) on 15 September. The September 15 event located near the cluster previously described while the May 12 event located within the outer rise. The same analysis was applied to these events to check accuracy of locations within the local catalog. Similarly to the events in the NEIC catalog these events also show a depth decrease of 20 km. The May event does not converge to a local minimum, however the RMS does decrease by half at shallower depths suggesting the hypocentral depth is likely shallow.

In order to constrain the rupture mechanics for the September events the first motion plots are shown in figure 2-8. The best fitting focal planes for the events were strike and dips of strike 348 and dip 10, and strike 122 and dip 70. First arrivals fit reasonably well with the mechanism of a low angle thrust of similar orientation and dip to the mechanism of the main thrust of the Maule earthquake. This provides a second line of evidence that the locations at, or near the plate boundary

are correct. The use of a simplified 1-D velocity model imparts some uncertainty on the takeoff angles for the rays that reach each station, which is likely the source of error in our focal mechanism solution. Figure 2-8a shows the first arrivals for the Mb 4.7 event occurring at 00:40 on September 15th. The best fitting mechanism for this solution corresponds to normal faulting. With a depth uncertainty of 1 km this could place the event within the subducting slab (suggesting a plate bending event) or within the inner wedge, which would suggest complex interactions between the corner of the inner wedge, outer wedge and subducting slab.

2.7 T-phases

T-phases are waves that are excited during an earthquake that enter the water column and travel through the SOFAR channel. These waves are usually high frequency (> 3 Hz) and travel at approximately 1.5 km/s, significantly slower than either P or S wave velocities, arriving at the instrument as the third large amplitude arrival. Examples of T-phases are presented in Appendix A (figure 7-6). Figure 2-9 shows the distribution of events with well-defined T-phases. Most events with evident T-phases plot within the outer rise and not within the accretionary prism, and only two events with greater than four picks plot within the wedge.

Understanding of this distribution is limited. The spectrum of the T-phase contains higher frequency energy than the S-wave coda, particularly in the 8-10 Hz range (figure 7-8). However, high frequency energy for events located below the accretionary wedge may be attenuated, limiting the ability for T-phase excitation within the SOFAR channel. A second plausible explanation for the distribution of events is that the excitation of T-phases near the continental margin is related to source mechanisms. However, with the data available here and the small aperture of the array this cannot be resolved. A complete list of source parameters for events that excite T-phases is provided in Appendix B (table 8-1).

2.8 Development of a Relative Magnitude Scale using Coda Lengths

Few events in our catalog had been assigned magnitudes by other institutions (37 events with assigned M_L from the Chilean Seismic Network). Here we attempt to use the method of coda-

length durations to determine local magnitudes. The stability of the coda, its magnitude independence from geologic structure, focal mechanism, or hypocentral distance from the station, [Crosson *et al.* 1972, Tsumura 1967, Mayeda *et al.*, 2003] make it ideal as a single station estimation of magnitude.

While it would have been preferable to apply the coda magnitude scale at a station within our network, data dropouts, high background noise levels, and the arrival of the T-phases limited our ability to apply this method on our OBS data. In order to overcome these factors, land station GO05 of the Chilean Seismic Network was used (figure 1-3). Due to the proximity of the station and its operating time during the deployment, GO05 recorded most of the seismicity seen in the ChilePEPPER dataset. Using a station on land solves the issue of T-phase arrival for two reasons. First, T-phases do not generally propagate into the crust, and if they do, they tend to attenuate very rapidly, allowing the full S-wave coda to be determined. Secondly, increased distance from the source allows adequate time for separation between the T and S phases. For our dataset, 362 events out of 569 were recorded at GO05. Using the method demonstrated by Mayeda *et al.* (1993, 1999, 2003), events were filtered at 3.0-3.2Hz. This frequency band was chosen because signal to noise ratios for lower frequencies were much lower for small magnitude earthquakes. Additionally S waves generally had the highest amplitude frequency between 3-3.5 Hz. We determined the coda envelope using a Hilbert transformation. A linear regression was then fit to the log-amplitude of the S-wave coda. The time at which this linear regression intercepted 0 was determined to be the end of the coda while the start of the coda was picked independently from the unfiltered seismogram (figure 2-10).

To calibrate the magnitude scale, we determined coda lengths for 37 well-recorded events with local magnitudes (M_L). Coda length vs. M_L was then plotted and a linear regression fit to the data (Figure 2-11). The correlation between coda length and local magnitude was calculated as:

$$M_{coda} = 5.7 * (\log(\text{filtered coda length})) - 8.9$$

The smallest coda magnitude (M_{CL}) recorded was a M_{CL} 1.1. The two largest M_{CL} applied were M_{CL} 4.4 and M_{CL} 4.2, which correspond to the M_b 4.7 and M_L 4.5 earthquakes on September 15th at 00:40 and 00:50. Average event magnitude was 2.8. Events smaller than 1.1 were probably too distant from the onshore station to rise above the noise level of that instrument. While this scale

may not be accurate for events smaller than M 2.9 it at least provides a relative magnitude scale for events detected during the ChilePEPPER deployment.

2.9 Magnitude of Completeness and b-value

The correlation between earthquake magnitude and frequency of occurrence is described by the Gutenberg-Richter law:

$$\log(N) = A - bM$$

Where N is the cumulative number of events with magnitude greater than M, and A and b are constants. In this equation the value b correlates to the number of smaller events relative to larger events. This means that the higher the value of b, the higher the number of smaller events there are relative to large events. The typical b-value in seismogenic zones is 1. Departure from this value can indicate that there is a systematic bias in magnitude calculations. B-values have also been used in other applications such as determining the stress state of the megathrust [e.g. *Nishikawa et al., 2014, Sobiesiak et al., 2004*].

Here we provide b-value calculation and magnitude of completeness as an independent check on the method of using coda magnitudes for events offshore. Following the methods of *Naylor et al (2010)* and *Mignan et al (2010)* [and references there in] we estimate the magnitude of completeness and b-value of the catalog of events produced by the ChilePEPPER deployment. Using the goodness of fit test it was determined that the catalog is complete for events above magnitude 3.6. Due to a two week recording gap during October at station GO05 and failure of some events to rise above background noise level limiting the number of calculated magnitudes, this is likely an underestimation. However, from these magnitudes the b-value was determined to be 1.00 with a 95% confidence interval of 0.27 (figure 2-12). This independent evaluation of the coda magnitude suggests that this is a robust method for events offshore of this region.

2.10 Very Low Frequency Events

In 2003 an anomalous style of seismic rupture was discovered within the Nankai trough in Japan [*Ishihara., 2003*]. These events are characterized by a very low frequency (VLF) content of

approximately 10 -100 seconds with little to no high frequency energy, preventing them from being detected by regional or global seismic arrays through conventional detection methods [Ishihara, 2003]. VLF earthquakes occasionally contain minor high-frequency wave-trains which indicate source properties distinctive from those of typical earthquakes [Obara *et al.*, 2005]. The spatial occurrence of these events typically overlaps documented aftershock areas in active subduction zones [Obara *et al.*, 2005]. These events are speculated to release overpressure through fluid expulsion along reverse faults within the accretionary wedge [Obara *et al.*, 2005] and have the potential to release significant amounts of stress without being observed in typical seismic studies.

In order to determine the possibility of the Maule prism responding in this manner, the data were bandpassed at 0.003-0.07 Hz and visually scanned on all instruments. 43 episodes of low frequency energy were noted (example figure 7-9). These events were then compared against times and locations of large seismic events within the ANSS catalog. Travel times of Rayleigh waves between these events and the ChilePEPPER array were calculated and found to account for 42 of the 43 events (Appendix C). While the 43rd event did not have a correlated event within the ANSS catalog, the similarity of its waveform to other Rayleigh waves suggests it is also a surface wave from an unpublished event, possibly of smaller magnitude but with a closer source. Other than the distantly sourced Rayleigh waves the only other long-period signal captured on the ChilePEPPER instrumentation was the Haida Gwaii tsunami, which had a period of over 20 minutes (figure 2-13). This leads to two possible conclusions. Either the wedge is not accommodating strain through this mechanism, or the dynamic response through slow slip and low frequency events occurred prior to the ChilePEPPER deployment.

2.11 Fluid Flow Measurements

According to the dynamic wedge theory as described by *Hu and Wang* (2006) stress should increase in the outer accretionary wedge after a great earthquake (figure 1-2). The increased fault stress subsequently increases pore-fluid pressure in the wedge and should induce fluid flow out at the sediment water interface. Fluid flow should exponentially decrease during the interseismic period as the wedge dynamically responds to the increased fault stress. This post earthquake relaxation has been noted in multiple subduction zones, most notably during the Nias-Simeulue earthquake of 2005 where direct cGPS on islands overlying the outer wedge captured the outer wedge deformation

[*Hsu et al 2006*]. In the Nanakai trough, gradual pore-pressure changes at the toe of the wedge suggest that pore-pressure re-equilibration may take more than 60 years [*Hsu et al 2006*].

In order to quantify the induced flow due to the hypothesized increased stress state of the outer wedge, all ten OBS packages were outfitted with CAT flow meters. Flow meters were attached to the base of the instruments with a collection chamber settling into the sea floor and capturing flow into or out of the sediment [*Tryon et al., 2001*]. Flow meter results showed that fluid discharge from the sediment, when equilibrated after the first order settling of the instrument, was < 0.005 cm/yr (figure 2-14). These flow rates are two to three orders of magnitude less than similar measurements taken along the Costa Rican margin [*Desbon et al., 2006*].

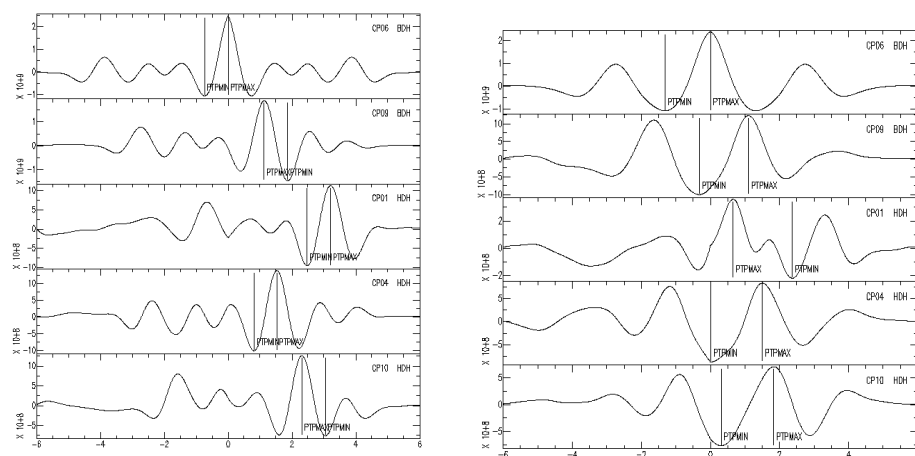


Figure 2-1: Cross correlation of waveforms for events from Colombia. The time shift is the same for all events except CP10. While the maximum correlation for CP01 (middle panel) is not quite correct the second maximum was chosen from looking at the original waveform and visually calculating estimated time lag.

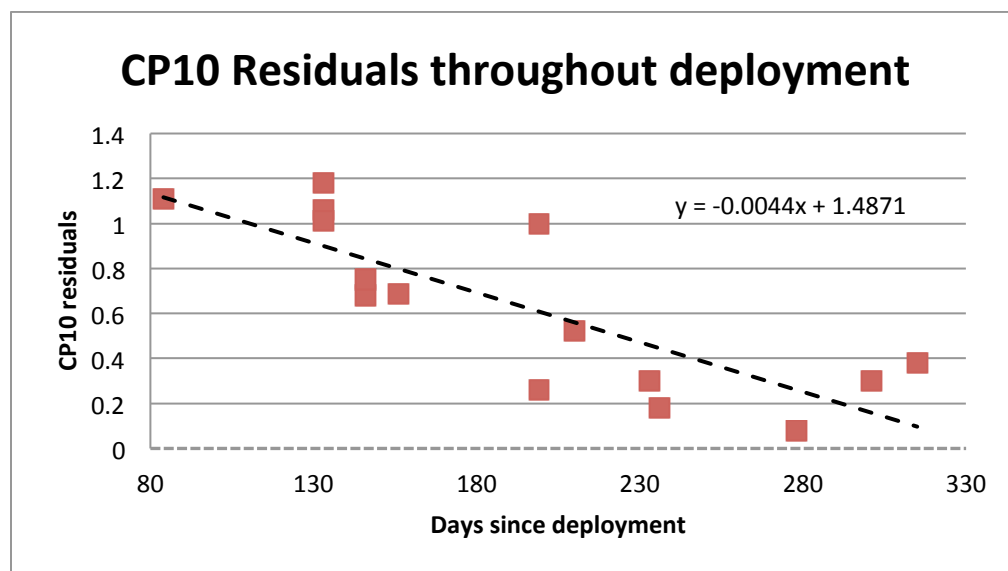


Figure 2-2: Plot of CP10 residuals during the ChilePEPPER deployment. Residuals decrease with time, which is unusual. The initial 1.5 second offset may be attributed to human error during deployment by entering the incorrect start time. In order to correct for this systematic time change, time was added to each individual CP10 pick based on the equation described above.

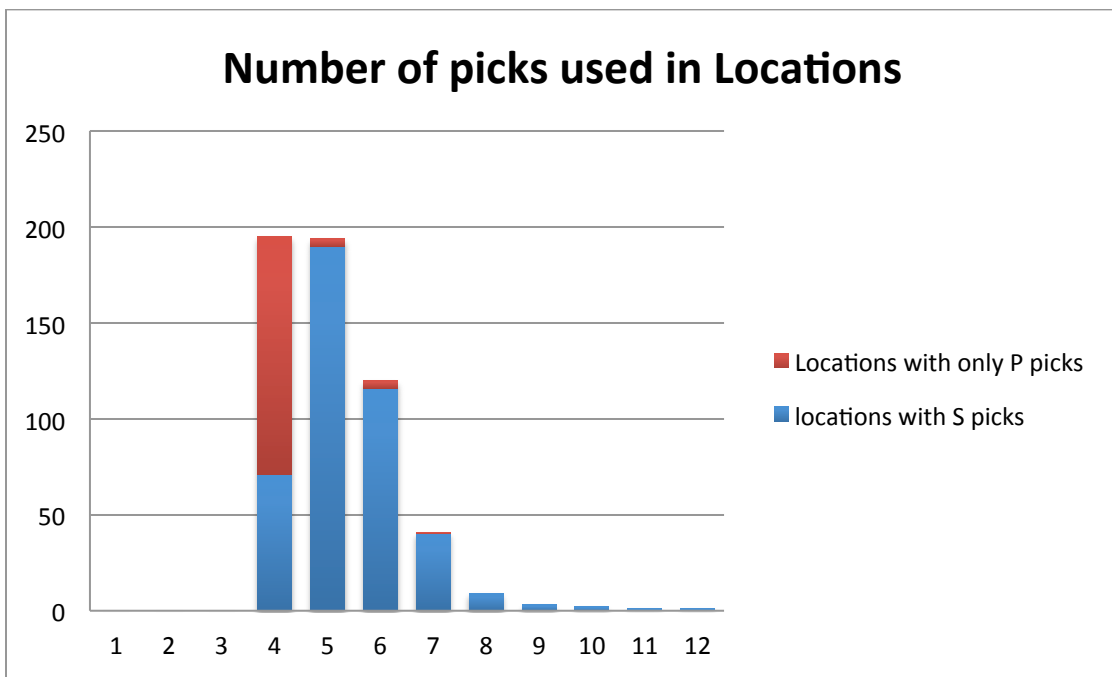


Figure 2-3 Number of picks used for locations. Of the 569 events presented, 386 events had < 6 picks.

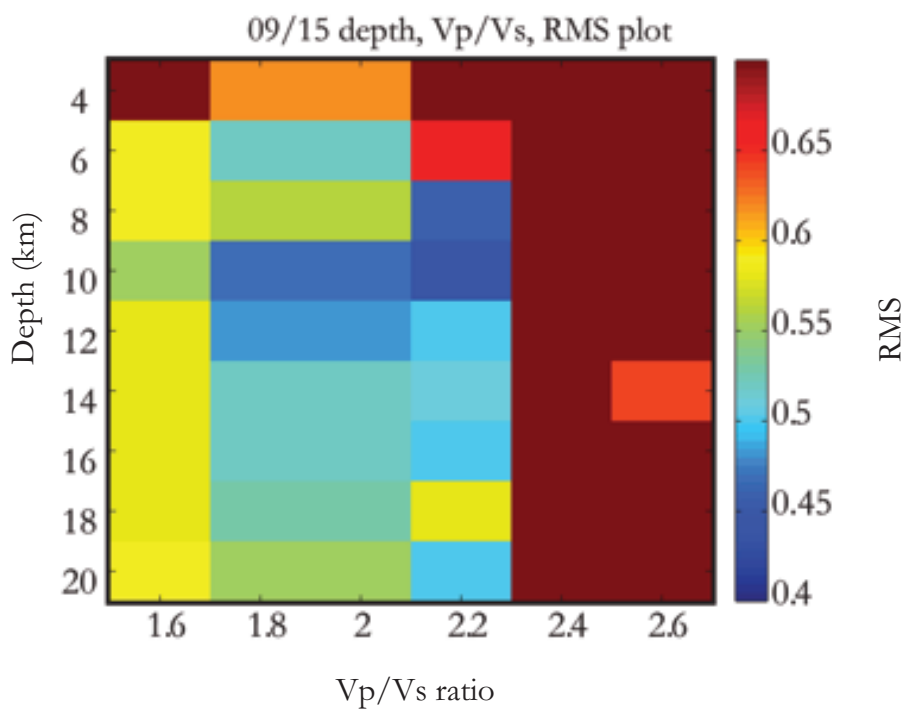


Figure 2-4: V_p/V_s , depth, RMS plot for the September 15th 00:40 (ML 4.7 event). Absolute minimum in RMS located at V_p/V_s ratio of 2.2.

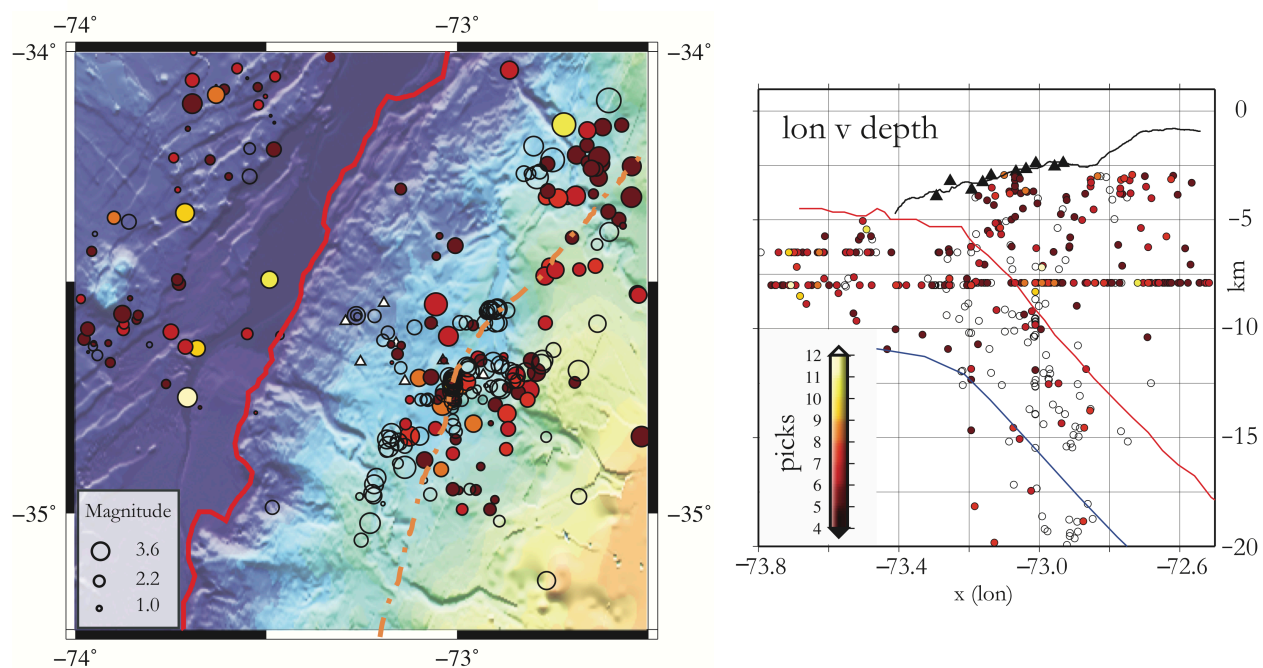


Figure 2-5 All events located by the ChilePEPPER array (events with < 5 picks shown as open circles) scaled by coda length magnitude. Lack of depth resolution is apparent as most earthquakes locate at the starting depth of the inversion (8 km). Events west of -73.2 are located using a velocity model for the outer rise, while events east of -73.2 are located using the 1-D velocity model for the accretionary wedge.

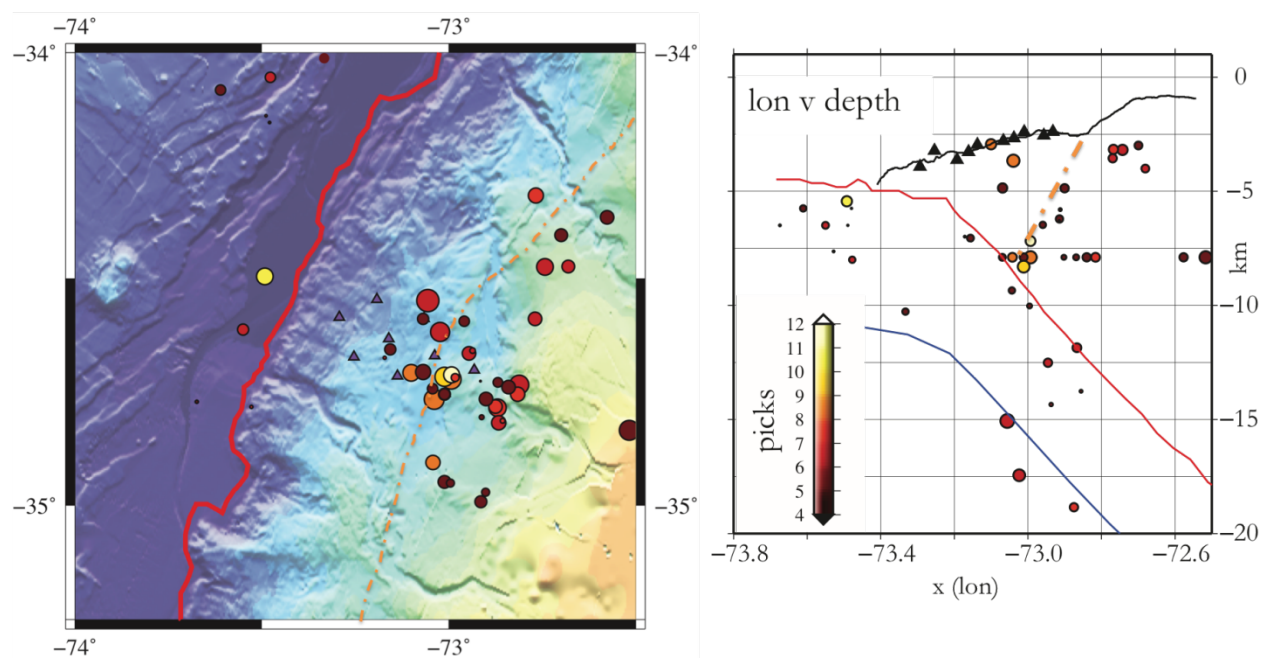


Figure 2-6 Well constrained events from the ChilePEPPER deployment. Events are color coded by number of picks used for the location, sized by magnitudes determined from coda lengths.

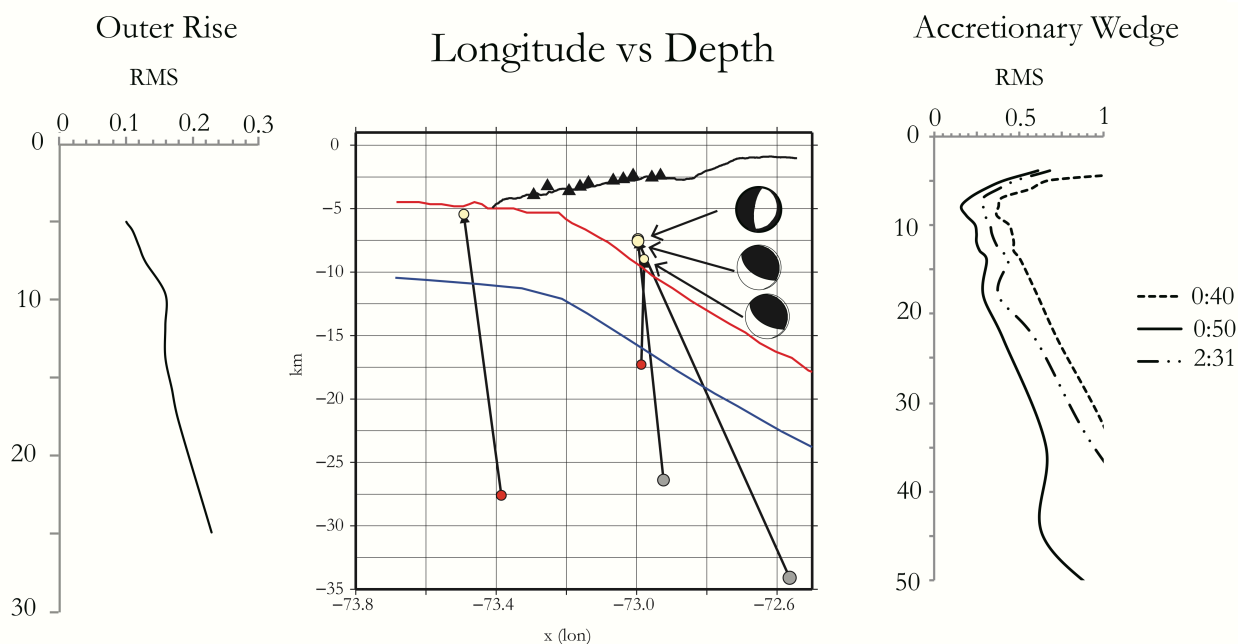


Figure 2-7 Events showing systematic depth bias in the NEIC (gray dots) and local (red dots) catalogs. Left panel: RMS vs. Depth plot for May 12th event in outer rise. Middle panel: longitude vs. depth plot of well located events by the ChilePEPPER array vs. NEIC and local catalog locations. Right: RMS vs depth plot for events occurring September 15th using the accretionary wedge velocity model.

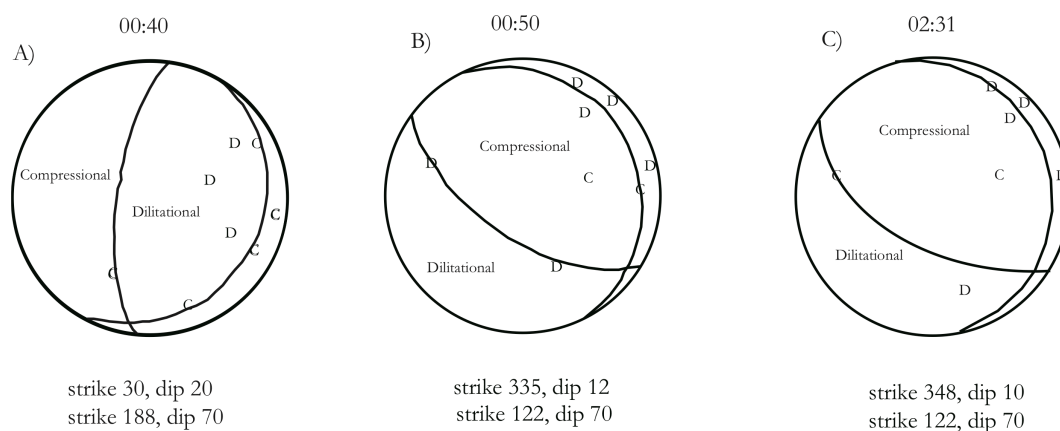


Figure 2-8 First motion plots for the September 15th sequence. The 00:50 (B) and 02:31 (C) events show mechanisms consistent with low angle thrusting. The event occurring at 00:40 demonstrates normal faulting.

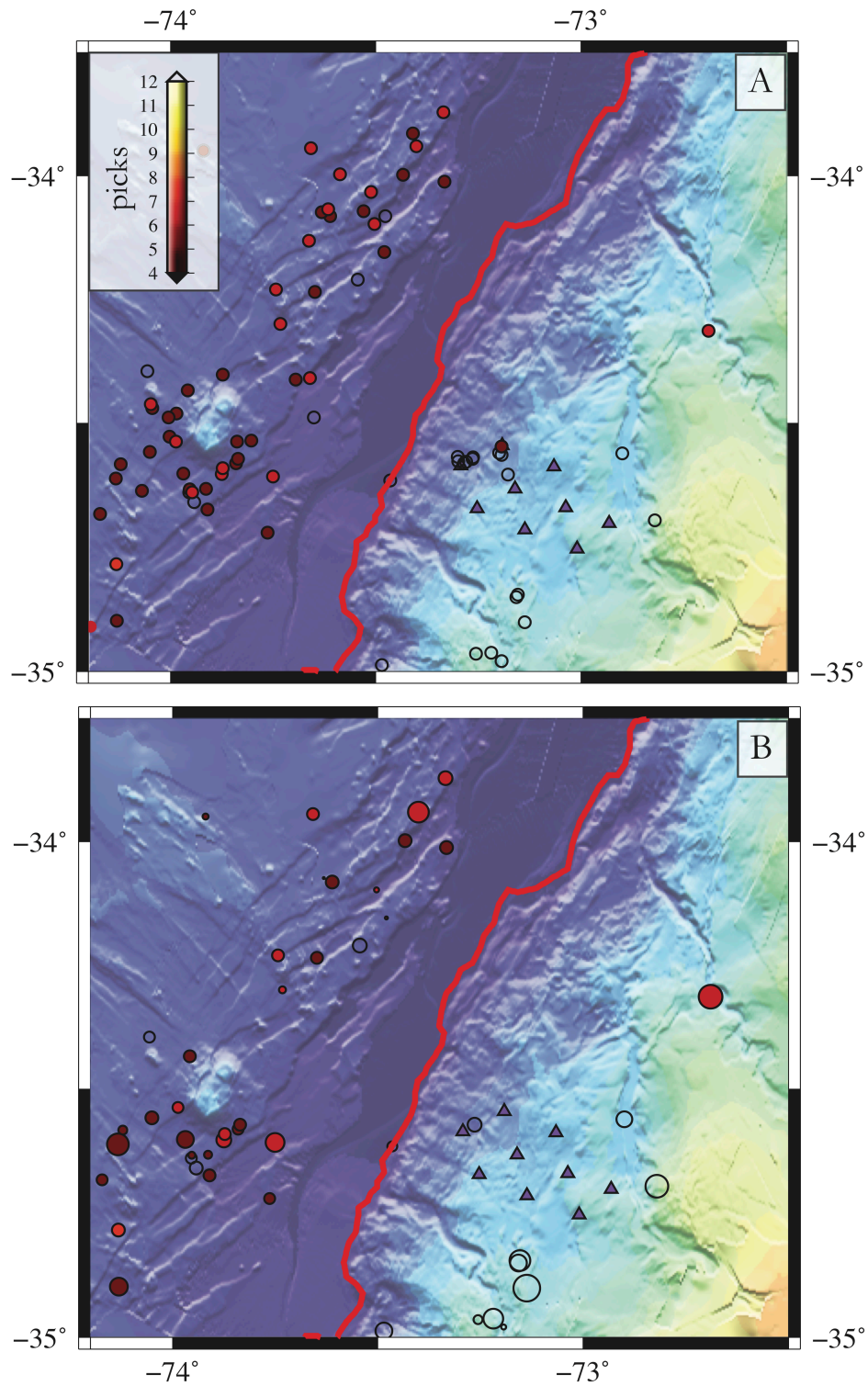


Figure 2-9: A: Events with well-defined t -phases colored by the number of picks used in the location. B: same as A but scaled by coda magnitude. Events that are not shown in B but are in A are events that did not have recorded coda magnitudes. Open circles represent events with < 5 picks associated with their location.

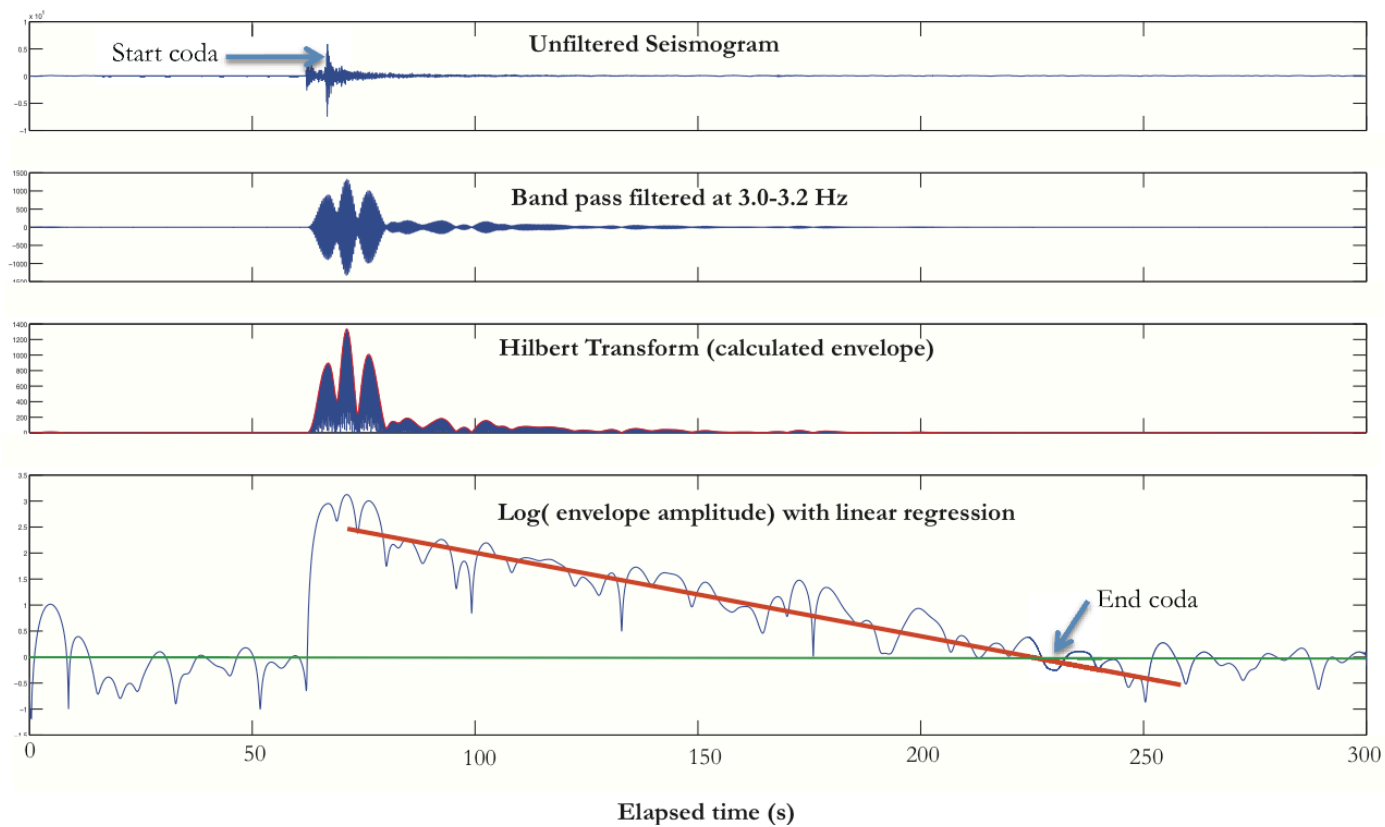


Figure 2-10 Method of magnitude calculation. Upper panel shows unfiltered seismogram from which coda start time is recorded. The log amplitude of the 3-3.2 Hz seismogram envelope is calculated and a linear regression fit (bottom panel).

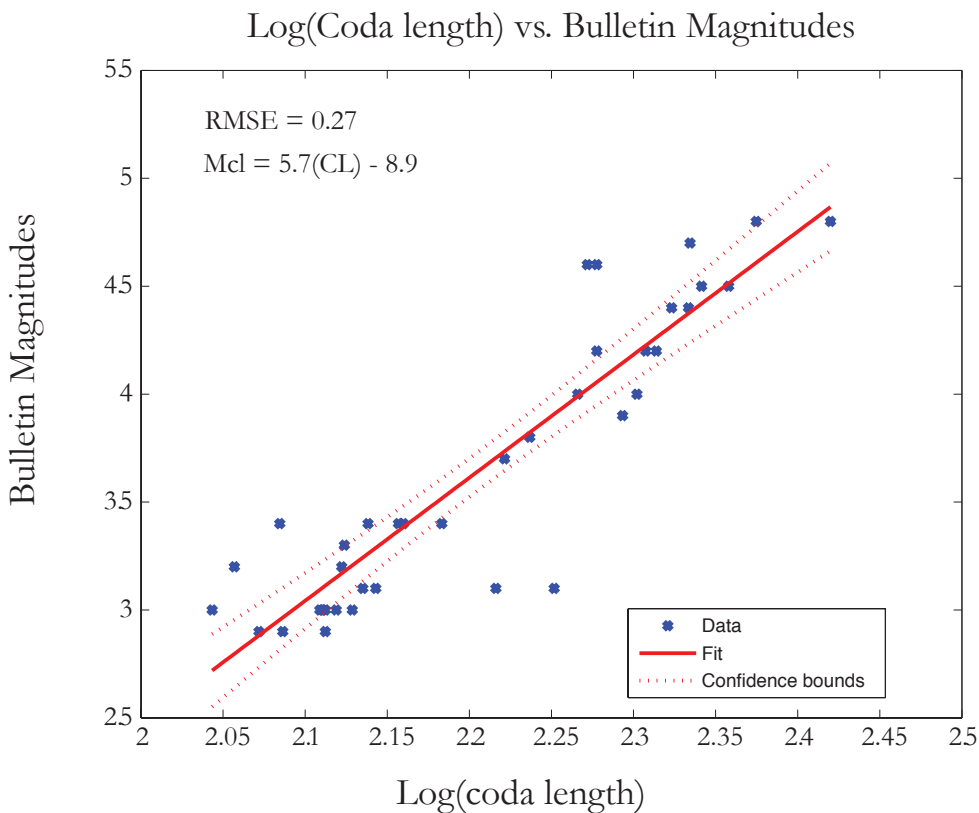


Figure 2-11: Coda Magnitude calibration from GO05. Coda Lengths (s) plotted against bulletin magnitudes. $R^2 = 0.84$. These values are extrapolated to lower magnitudes for events detected from the ChilePEPPER array.

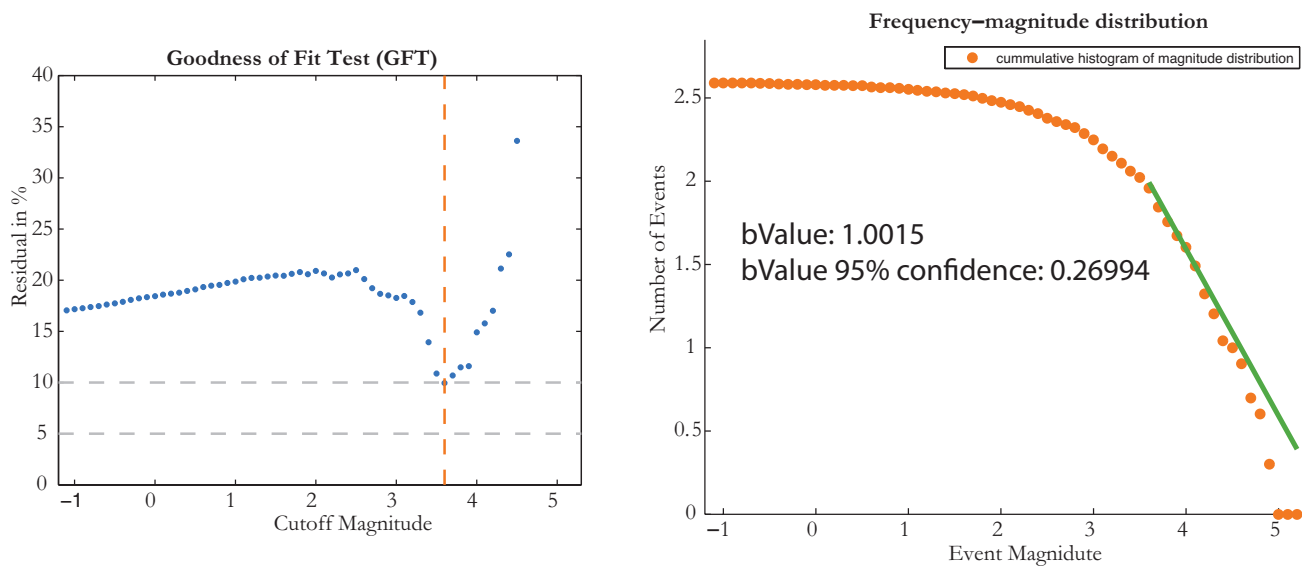


Figure 2-12 Magnitude of completeness calculated from the goodness of fit test shows a Mc of 3.6 (left) while the frequency magnitude distribution, and associated b-value is shown on the right.

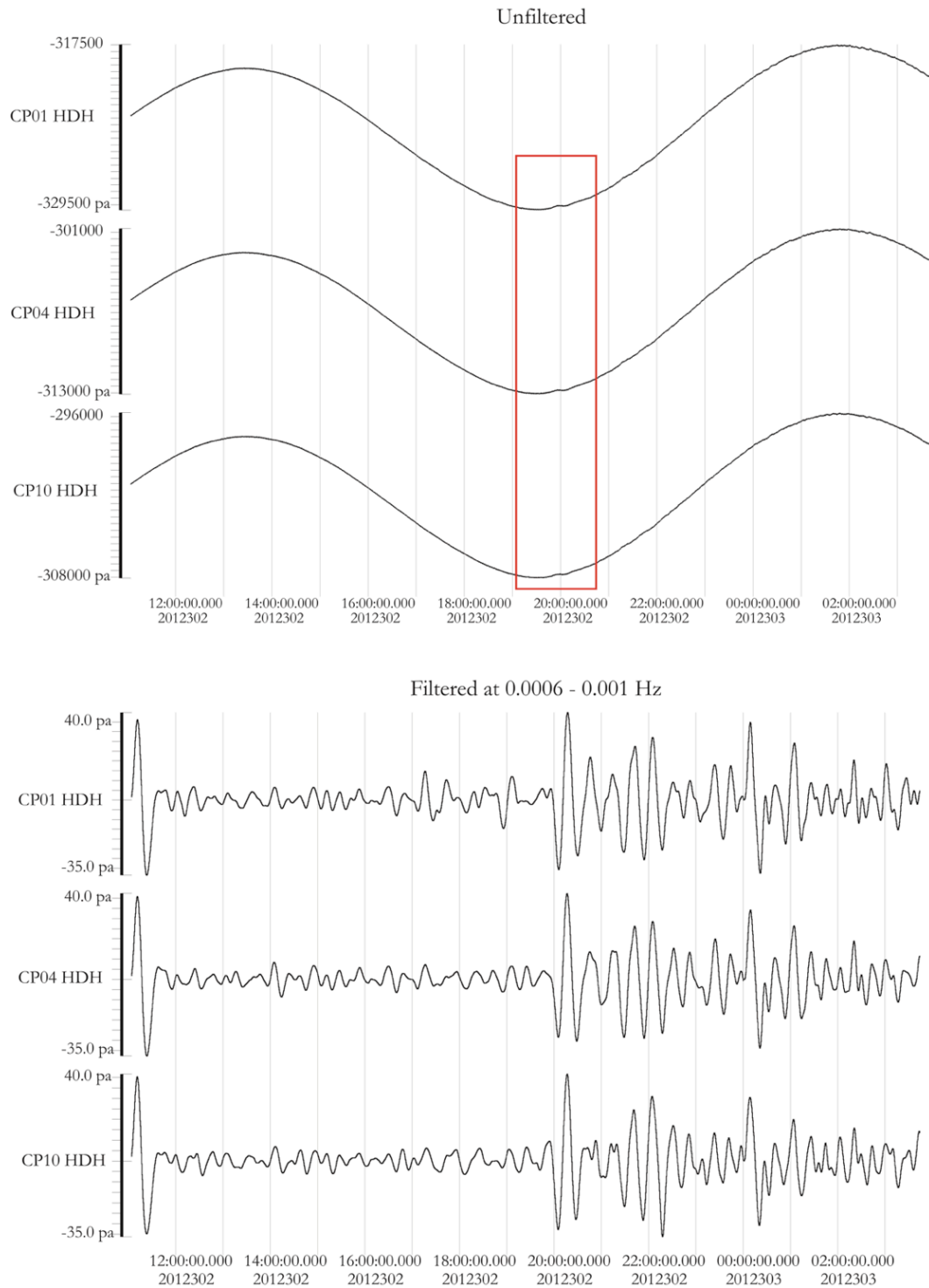


Figure 2-13: Haida Gwaii tsunami captured on ChilePEPPER Absolute Pressure Gauges.

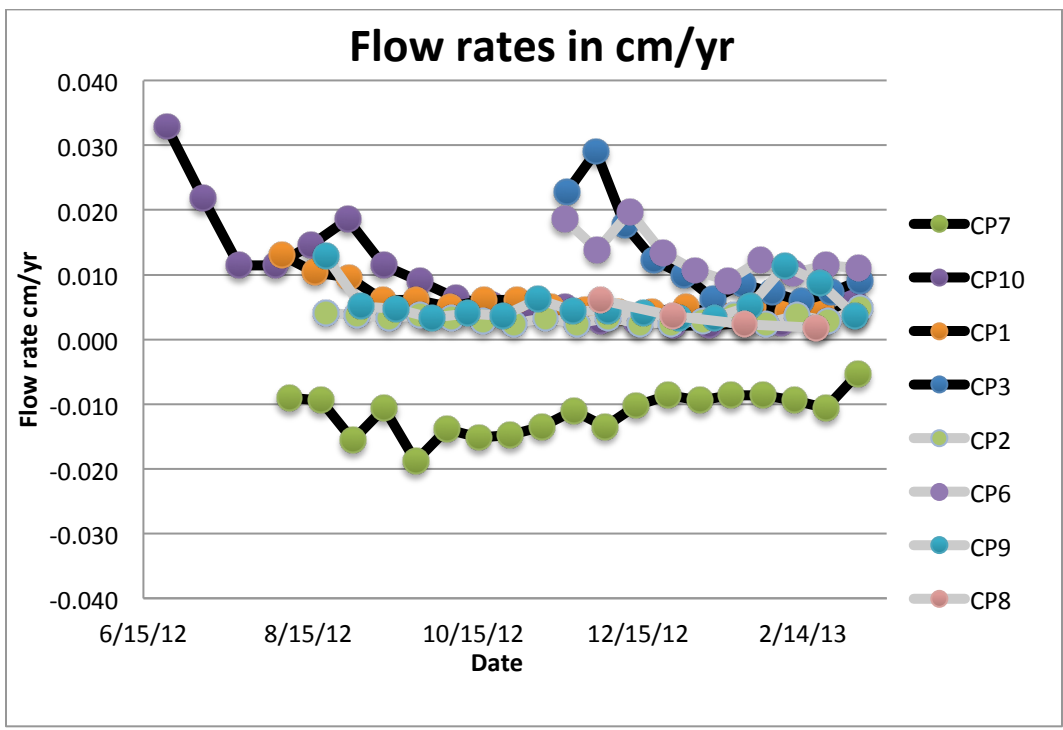


Figure 2-14 Flow meter results from the ChilePEPPER deployment. First order trend is that associated with the settling of the instrument which stabilizes for all instruments at ~0.01 cm/yr.

Event and Magnitude	Depth	Date	Azimuth, Angle of Incidence
Argentina M6.7	586.9	05/28/2012	54°, 63°
Argentina M6.1	585.8	02/22/2013	54°, 63°
Colombia M7.3	170.0	09/30/2012	355°, 42°
Colombia M6.9	145.0	02/09/2013	355°, 42°

Table 2-1 Events used to determine if timing issues were present in well recording stations. Events occurred from two locations at similar depths covering most of the time that stations were recording

	Argentina 05/28/2012	Argentina 02/22/2013	Colombia 09/30/2012	Colombia 02/09/2013
CP01	0.68	1.071	3.21	3.31
CP04	-0.04	-0.01	1.53	1.50
CP09	1.184	1.271	1.13	1.10
CP10	1.8	1.05	2.31	1.83

Table 2-2 Results from cross-correlation of waveforms relative to CP06. For CP01, CP04, and CP09 correlation stays the same for all events. This is not the case for arrivals from CP10 which appears to contain a clock drift amounting to loss of 0.25s ~ every 100 days. Variations in timing between the delays of the Argentinian events and the Colombian events can be attributed to differences in azimuth and angle of incidence. At site CP04 a straight line approximation of arrival times through the Moscoso velocity model were calculated for the two different sources. The results of this calculation were a difference in arrival times of ~1.2s, well within the error of a straight line approximation.

Earthquake	Catalog	Latitude (°S)	Longitude (°W)	Depth (km)
May 12th 18:15	NEIC	34.523	73.269	15
	CSN	34.449	73.385	27.6
	CPEPP	34.495	73.492	5.4
Sept 15th 00:40	NEIC	34.638	72.564	34.1
	CSN	N/A	N/A	N/A
	CPEPP	34.717	73.011	8.3
Sept 15th 00:50	NEIC	34.622	72.923	26.4
	CSN	34.622	72.923	26.4
	CPEPP	34.722	72.993	7.9
Sept 15th 02:31	NEIC	N/A	N/A	N/A
	CSN	34.647	72.987	17.3
	CPEPP	34.713	72.993	7.2

Table 2-3: Locations and depths of well-located events from the National Earthquake Information Center (NEIC), Chilean Seismic Network (CSN) and ChilePEPPER (CPEPP) demonstrating differences in hypocentral locations.

3 ANALYSIS OF BATHYMETRY IN THE NORTH MAULE REGION

3.1 Introduction

Segmentation of the marine forearc has been interpreted in the Maule region immediately to the south of our study region based on characteristic morphoplogy as seen in swath bathymetry and multi-channel seismic data [Geersen *et al.*, 2011]. Based on the analysis by Geersen *et al.* (2011), the Concepcion North segment (-35.1S to -36.2S) is characterized by prominent, landward-dipping thrust ridges (~600 m of surface expression) within the crystalline basement (figure 4-1 and 4-2 a,b). Thrust ridges have been correlated to splay faults, which may transfer coseismic slip during large earthquakes from the plate boundary into the upper plate. This segment shows a distinct lack of normal faulting within the forearc as compared to the South Concepcion segment (-36.1 to -36.7S). The South Concepcion segment also demonstrates prominent thrust ridges; however the morphology in this region is dominated by 500-m high, seaward-dipping escarpments related to normal faulting (figure 4-2 c, d). The proposed mechanism for this change in morphology is a thicker subduction channel to the south, underplating sediment and causing uplift of the crystalline forearc [Geersen *et al.* 2011]. The morphology of the forearc has not been analyzed for the region north of -35.1S, the region correlated to the high slip patch of the Maule rupture. We build on the analysis of Geersen *et al.* (2011) to interpret distinctive features seen in this area.

3.1.1 Data

High-resolution swath bathymetry was downloaded from GeoMapApp (<http://www.geomapapp.org/>) and combined with data collected during the ChilePEPPER cruise.

3.2 North Maule

Here we look at high-resolution swath bathymetry of the North Maule region. The original data are presented in figure 4-1 (whole region) and 4-3 (study area). Trench-parallel horst and graben structures seaward of the trench are present in the bathymetric data and disappear within 20 km of the trench. The structures become buried in sediment as the Nazca plate bends beneath the South American plate. High sedimentation rates linked to deglaciation and erosion of the Andes mountains since the Pliocene [e.g. Kukowski and Oncken, 2006] combined with strong alongshore sediment transport have created an ~2 km thick blanket of sediment on the incoming plate in this area. The

axial channel running south to north along most of the south-central Chilean coast is a prominent expression of the alongshore sediment transport.

The most distinct feature along the deformation front is a 15 km wide indentation at -35°S . The morphology of the incision suggests an entrance scar from a subducting seamount. The width of the scar correlates well to incoming features on the Nazca plate e.g. at -34.5°S -73.9°W (figure 4-4) and is similar to entrance scars seen in other subduction zones correlated to subducting topography (e.g. Costa Rica, *Dominguez et al.*, 1998, Cascadia, *Trebu et al.*, 2012). Just south of this feature is a less well-defined indentation of similar width, which may also be the result of subducting topography. At -34.4°S the deformation front steps ~ 5 km seaward, which is coupled with distinct trench-parallel folding features and the transition from sediment subduction to sediment accretion (figure 4-5).

Three submarine channels cut through the forearc. Channels to the north and south are deeply incised meandering channels that terminate at the deformation front. The northernmost channel shows distinct slope failure features towards its landward extent. The morphology of the middle channel is distinct from the channels that bound it to the north and south as it lacks meanders and terminates 40 km landward of the deformation front. Termination of the channel corresponds to a 500 m fault scarp.

Approximately 34 km landward of the deformation front is a poorly formed trench-parallel linear feature that runs discontinuously 80 km through the entire study area (figure 4-4). This feature contains similarities to the thrust ridges and normal faults that characterize the Concepcion north and south segments. However, this feature lacks lateral continuity and, based on surface morphology, shows aspects of both normal and thrust faulting varying on the order of a few kilometers (figure 4-2 e, f) which is a distinctly different characteristic than the described segments to the south (figure 4-2 a,b).

Other features stand out in the calculated bathymetric gradient field (figure 4-3) that are difficult to resolve from the bathymetric data. To the south of the folding accreting sediments, are strong along-strike lineations within the outer accretionary prism. The morphology of these lineations and their proximity to the accretionary structures just to the north, lead to the interpretation that this was a paleo deformation front accreting sediment similar to the one directly along strike.

North of the rupture zone the morphology of the forearc resembles that of the North Concepcion forearc with a continuous thrust ridge that extends > 80km along strike. This feature has been associated with splay fault activity during the Pichilemu aftershock sequence [*Lieser et al.*, 2014].

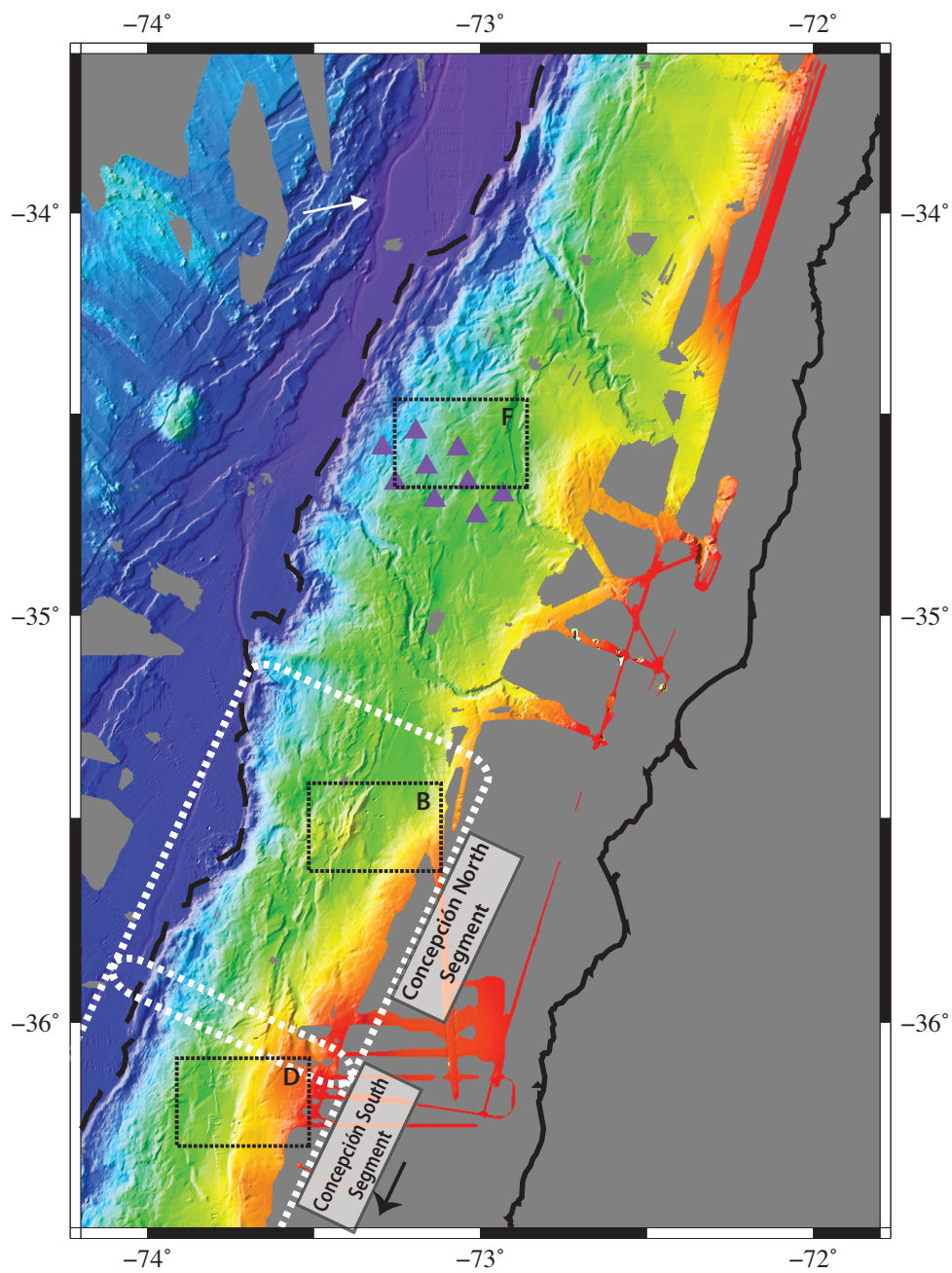


Figure 3-1 High resolution swath bathymetry of the North Mule area. Black squares correspond to figure 4-3.

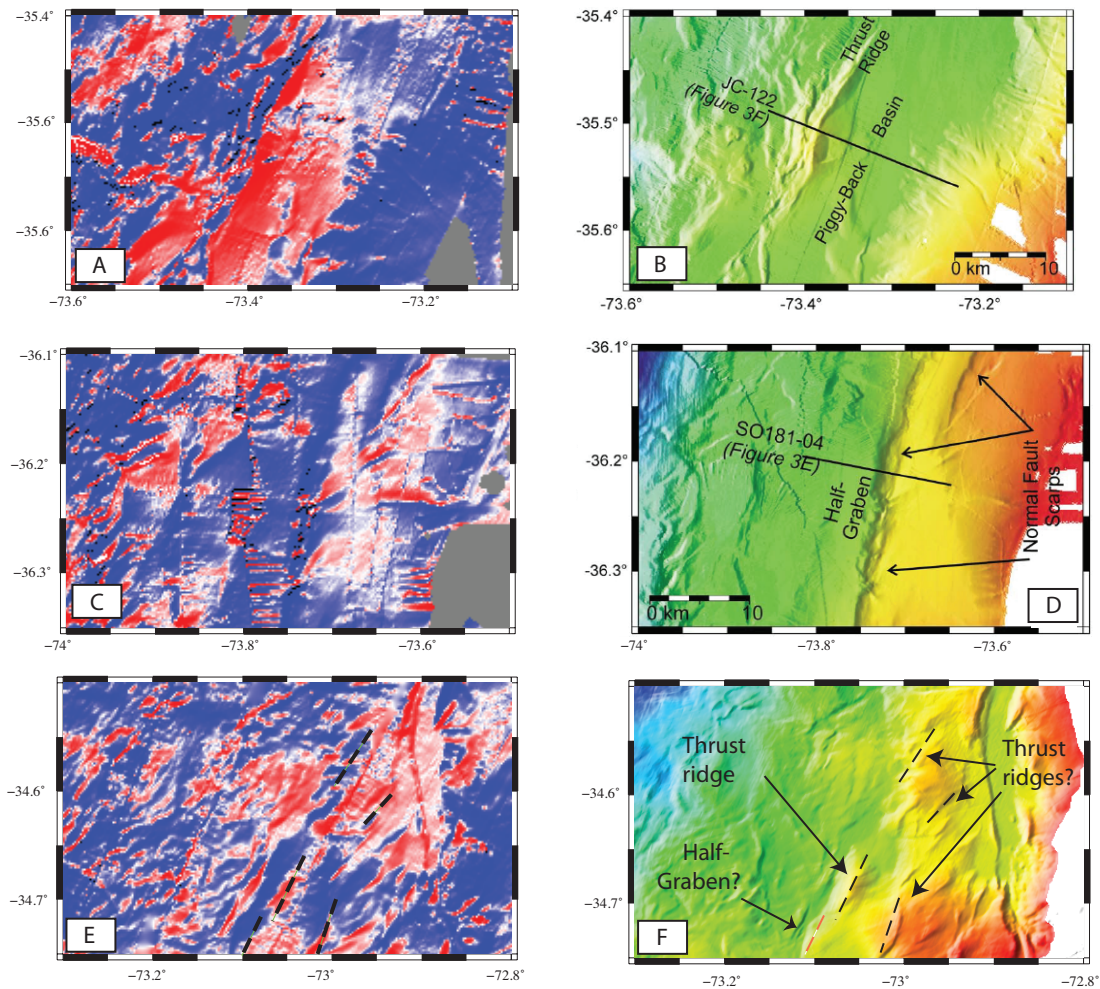


Figure 3-2 Examples of features seen along the Chilean margin. Left panels (A,C,E) are the trench perpendicular gradient of the bathymetry shown on the right (B,D,F). Top two rows are examples from other places along the Chilean margin that show typical examples of thrust ridges (A,B) and normal faulting (C,D). Bottom panel is a linear feature that cuts through the ChilePEPPER study area that shows features of both thrust ridges and normal faults with exposed scarps to the north and south straddling a possible thrust ridge and piggyback basin. This shows that the along strike characteristics of faulting in the ChilePEPPER region vary on the order of < 10 km (scale in bottom right corner of panel B).

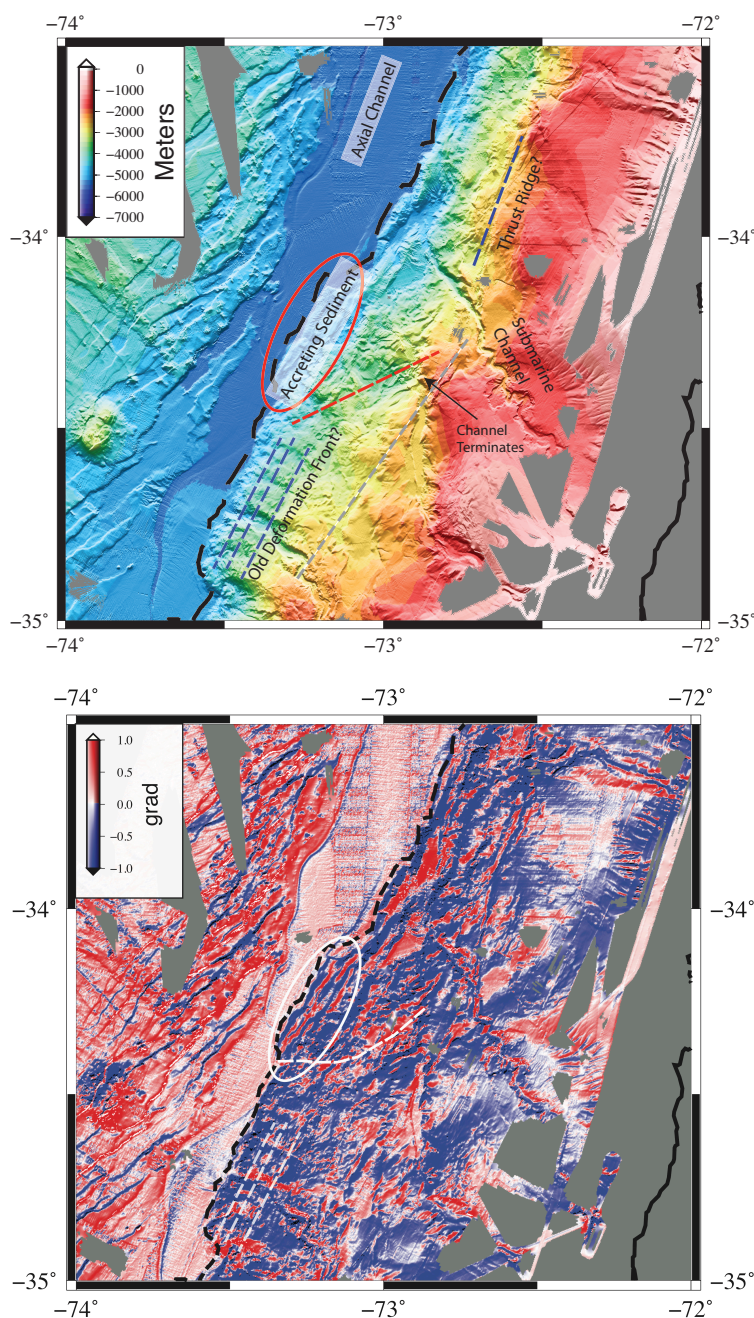


Figure 3-3 (Top panel) Close up of study area with features in the bathymetry outlined. Of particular note the submarine channel that terminates suddenly. The ENE-WSW feature (red dashed line) is a feature seen in the bathymetric gradient map that is not currently well understood. Gray dashed line is an ~80 km feature which cross-cuts the ChilePEPPER array and is discussed in the text. Thrust ridge (dark blue dashed line) described by Lieser (2015), which may be related to the Pichilemu aftershock sequence. (Bottom panel) Gradient of the bathymetry calculated perpendicular to the trench. The white oval shows distinct trench parallel lineations, which can be attributed to sediment accretion at the deformation front. Other trench parallel features to the south are shown in white dashed lines, which may be attributed to a formerly active deformation front. The strong ENE-WSW trending feature (white dashed line) present may be associated with the transition from sediment subduction to accretion, but is not well understood at this stage. A and B in figure correlate to MCS data shown in figure 4-5.

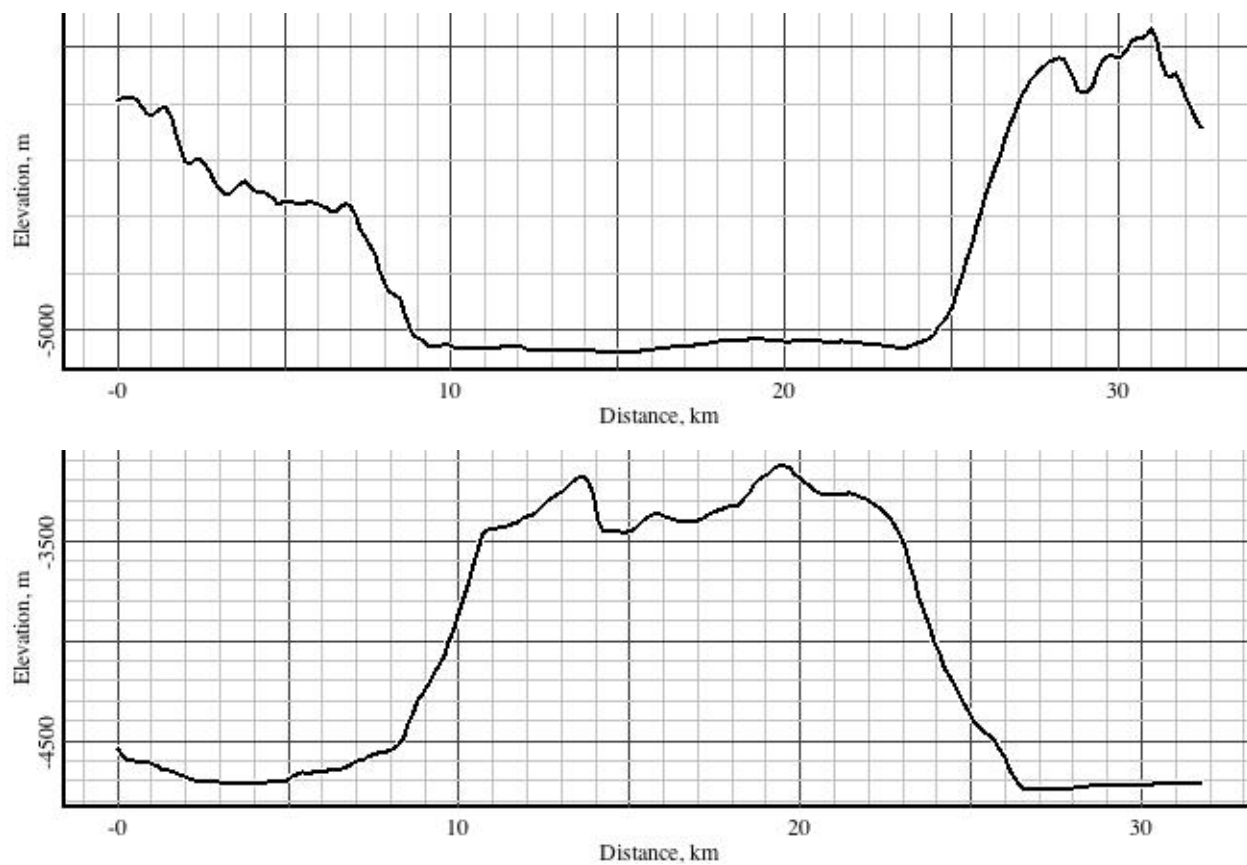


Figure 3-4 Morphology of incision in deformation front at -35S (top panel). Incoming seamount on Nazca plate (bottom panel).

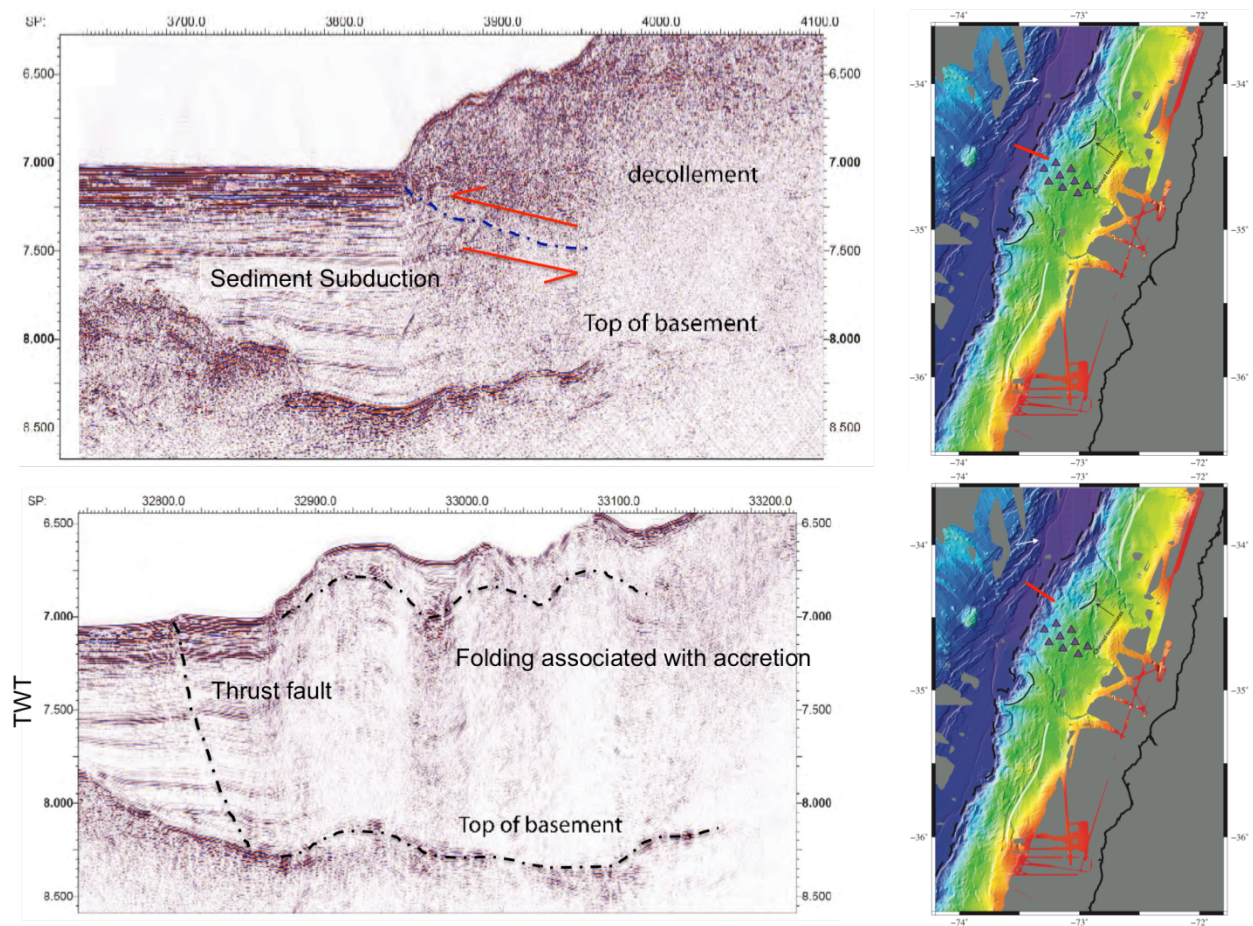


Figure 3-5 Multi Channel Seismic reflection data showing transition from sediment accretion (top panel) to sediment subduction (bottom panel) over the course of a few kilometers. Locations of seismic data acquisition shown in figure to the right.

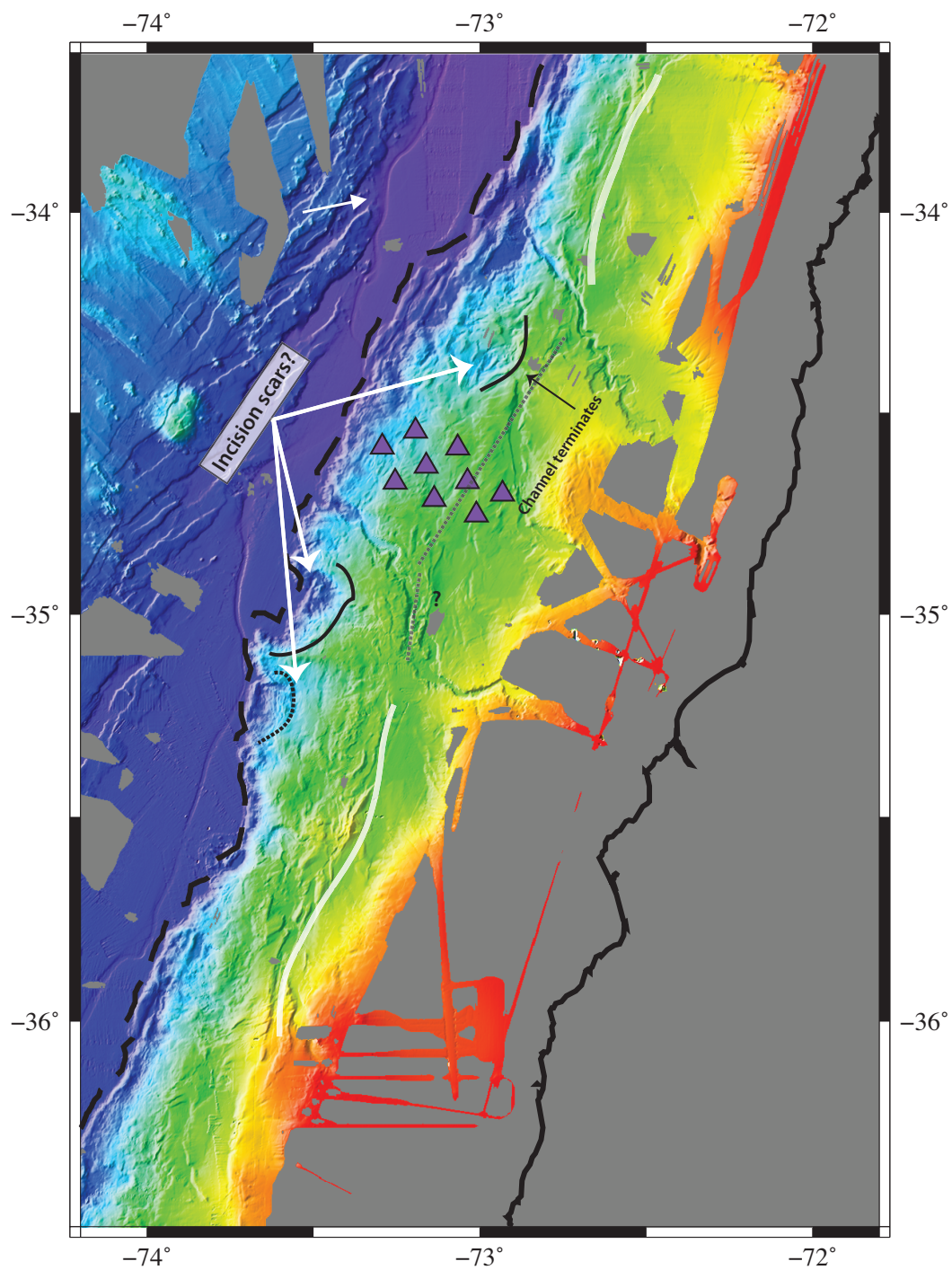


Figure 3-6 Same as 4-1 with features outlined in the North Maule segment. Black lines are projections of the modern convergence rate. Dashed lines correspond to 15 mGal contours associated with bullseye structures from TCBGA

4 GRAVITY

4.1 Introduction

A correlation between gravitational anomalies and slip distribution during earthquakes has been noted since 2003 [Song and Simons 2003, Wells et al., 2003]. Song and Simons (2003) noted that trench parallel gravity lows correlated to areas of high slip during large ($M_w \geq 6.0$) subduction zone earthquakes. They attribute this to higher shear traction on the plate interface, depressing local topography and gravity. Similarly, Wells et al (2003) note that high slip is correlated with fore-arc basins as distinguished by free-air gravity lows, which are likely created due to basal erosion that depresses the overlying forearc. This suggests that fore-arc basins may indicate the presence of asperities on the underlying plate boundary. However, other along strike variability in the gravity field can be associated with subducting features or variations in the rheology of upper plate, which can either promote or limit slip on the seismogenic contact [e.g. Aki, 1979, Sobiesiak et al., 2007, Contreras-Reyes et al., 2011, Wang and Bilek, 2014].

To aid in the interpretation of ChilePEPPER results we provide a terrain and slab corrected bouguer gravity map of the Maule region. Gravitational anomalies may help determine physical factors that play a role in seismogenesis and slip distribution.

4.2 Method

Spatial variations in the observed gravity signal can be caused by a variety of factors, including slab bouyancy, lithology, density anomalies and mantle rheology. This is further complicated for uncorrected free-air gravity data which contains a first order signal of topography. While Bouguer corrections are standard onshore, offshore corrections are rarely done. This is particularly detrimental to understanding gravity signals over the continental margin where there are rapid bathymetric changes and the signal is further dominated by the high amplitude long-wavelength signal from the subducting slab. This obscures smaller wavelength features resulting from topography on the subducting plate and structures within the upper plate. In order to correct for these effects we build on the method of Maksymowicz et al (2015).

4.2.1 Grid Preparation

In order to perform this correction, bathymetric and free-air gravity data are required. For this region, data were downloaded from GeoMapApp [Ryan *et al.*, 2009] with grid resolutions for GMRT bathymetry and *Smith and Sandwell* free air gravity of 440 m and 1,833 m respectively. In order to remove signals from rapidly varying topography, grids were first low pass filtered at 10 km and resampled at 1000 m grid spacing.

4.2.2 PRISM Code

We use the equation for the gravitational attraction of a rectangular prism from *Blakeley* (1995) to produce a terrain corrected gravity anomaly map for both onshore and offshore of the Maule rupture region.

$$g = \gamma\rho \int_{z_1}^{z_2} \int_{y_1}^{y_2} \int_{x_1}^{x_2} \frac{z'}{[x'^2 y'^2 z'^2]^{3/2}} dx' dy' dz'$$

We calculated the effect of 3D rectangular prisms of density 2.7 g/cm³ with a cross sectional area of 1km and height corresponding to water depth (offshore) or altitude (onshore) in that grid point (figure 2-1a). *Makymowicz et al* (2015) performed a similar calculation, however they underestimated the effect by not summing adjacent prisms, which is particularly detrimental at greater water depths. Figure 2-1b shows a test to determine how many kilometers away from the central grid point must be added to the gravitational anomaly. This shows that in order to capture the full effects at water depths equal to the depth of the trench, a 41 x 41 km grid around the observation point must be included. By incorporating prism heights determined by water depth, or topography, this inherently goes beyond a simple bouguer gravity correction and applies a more complex terrain correction both onshore and offshore that seamlessly crosses the coastline. The results of the terrain correction are shown in figure 2-2b.

In order to remove long wavelength effects of the subducting slab, data was low-pass filtered using a 2D convolution filter in matlab with a filter length of 100 km (Matlab function conv2). The low frequency signal was then removed from the terrain corrected gravity anomaly producing a complete gravity correction. A 100 km lowpass filter was determined to be optimal for this region from comparing various filters (50-120 km) to slab structure as determined from Slab1.0 [Hayes *et al.*,

2012]. The 100 km filter contained most of the structures as outlined by the subducting slab without removing higher frequency anomalies that may be caused by structure on the subducting slab or within the upper plate.

4.3 Case Study: Maule Region

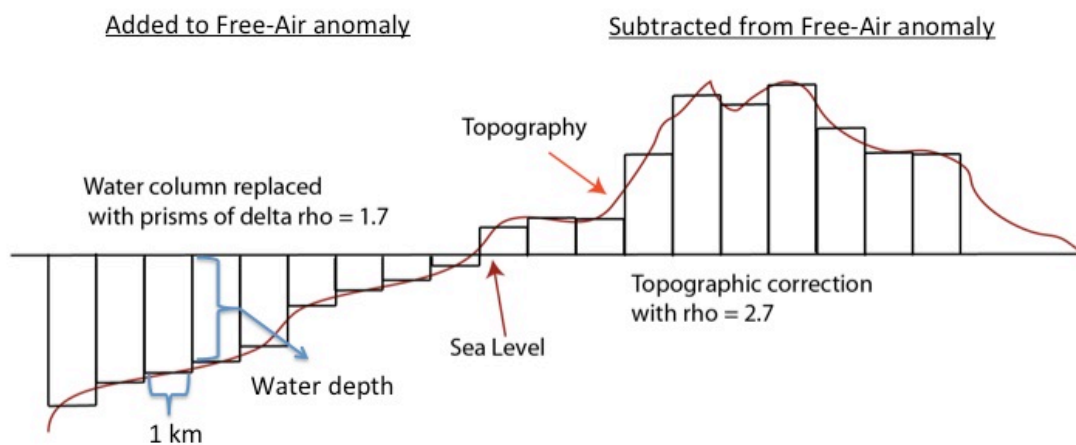
Figure 4-2c shows the 2D convolution, low pass filter for the Maule region. This provides a first order estimation of the gravitational effects of the subducting slab. Trench-parallel variations in the gravity field that diverge from predictions of the slab 1.0 model, particularly near 36°S, may be due to previously unrecognized long wavelength structures either on the subducting plate, or within the upper plate density structure. The gravitational high (~25 mGal difference from surroundings) correlates to an inflection point in margin parallel slab dip as described by *Moreno et al. (2012)* as well as a systematic decrease in depth of aftershock hypocenters as described by *Rietbrock et al (2012)* suggesting subducting plate topography on the order of a few kilometers. However, uncertainty in hypocentral depths offshore is high and the decrease in depths of these hypocenters could result from errors in the velocity model used during hypocentral location.

Figure 4-3 shows the terrain and slab-corrected gravity anomaly for the Maule region. Using tomographic inversions from P-wave arrivals from the aftershock sequence of the Maule earthquake, *Hicks et al (2012)* noted a high P-wave velocity anomaly below the shoreline at -36°S. The interpretation of this feature is a subducting or obducted seamount possibly responsible for nucleation of the Mw 8.8 event due to increased stress at the up-dip limit [*Hicks et al., 2012*]. This feature is seen as a pronounced 25 mGal gravity high in the corrected gravity data.

Other subducting features include the 20 mGal gravitational anomaly located to the NE of the ChilePEPPER array, which has also been interpreted as either a subducting seamount or a local increase in contact friction [*Maksymowicz et al., 2015*]. This feature is in the middle of three other similar magnitude and expression anomalies that form a NE-SW trending trench parallel gravity high. Analysis of these features based purely on the gravity field is not unique. Without incorporation of other data sets, at least three possible interpretations exist of these features. First they could be the expression of the forearc high, which is the outer most expression of the crystalline continental basement being uplifted due to shear traction on the megathrust. These features could also be a set of four distinct subducting or obducted seamounts, or distinct rheological heterogeneities in the upper plate.

The pronounced, elongate trench parallel gravity low within the patch of highest slip is likely associated with a fore-arc basin as noted by *Wells et al., (2003)* in other subduction zones. In this case, high shear traction along the megathrust leads to basal erosion. Basal erosion then depresses the overlying continental basement creating accommodation space for incoming sediments, which expresses itself in the gravity field as a gravity low. High shear traction at the plate along the megathrust is further demonstrated by the correlation of the TPGA low with the 100% interseismic locking described by *Metois et al., (2012)* (figure 2-3b).

A)



B)

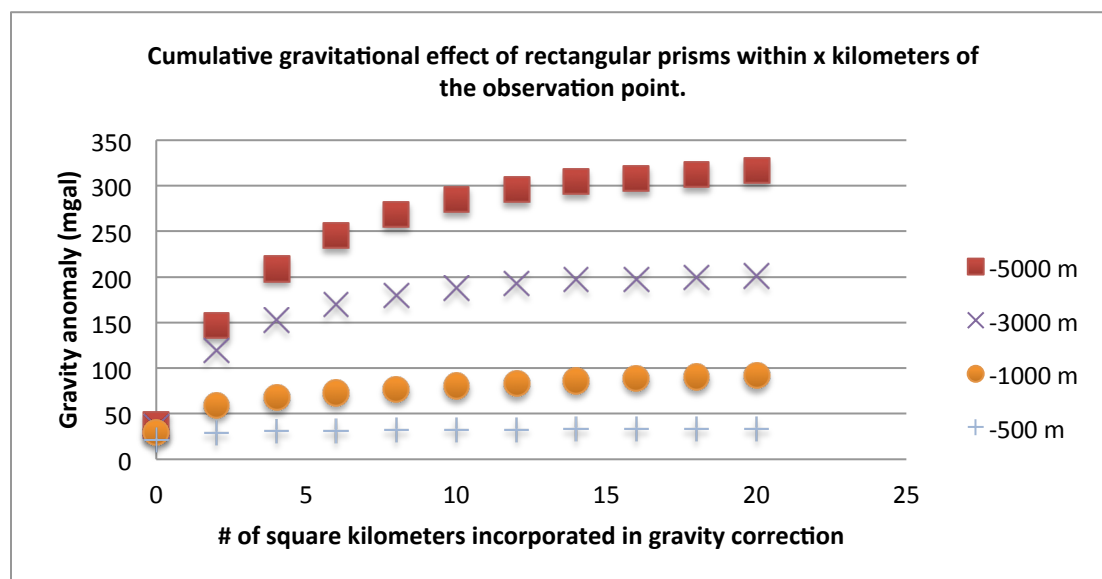


Figure 4-1: 2-D Schematic of the topographic correction applied onshore and offshore (A). The dimensions of each 3D rectangular prism are $1\text{ km} \times 1\text{ km} \times \text{water depth (or altitude)}$. The correction offshore uses a $\Delta\rho$ of 1.7 (density of rock – density of water), while onshore prisms are calculated with $\rho = 2.7\text{ g/cm}^3$. Onshore, the gravitational attraction of the prism is subtracted from the free-air anomaly while offshore it is added in order to correct for either mass excess above sea level, or mass deficiency below sea level. B) Test showing the # of square kilometers away from the observation point need to be incorporated into the complete correction. Prisms over 20 km away add no additional gravitational anomaly.

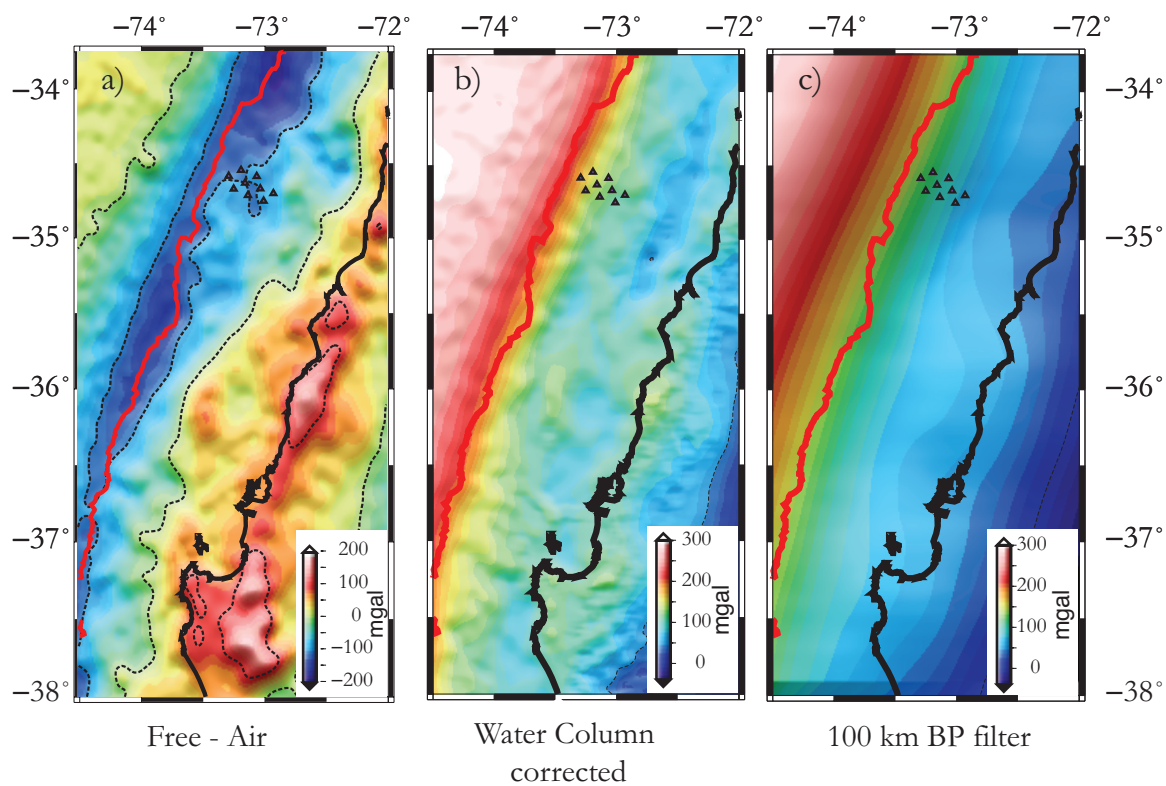
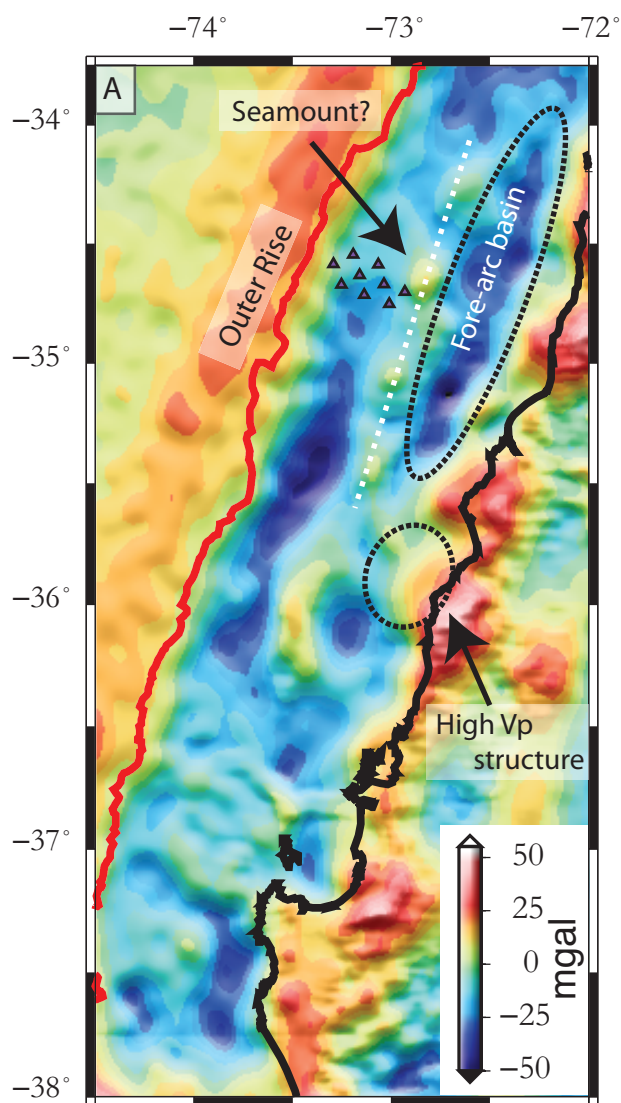
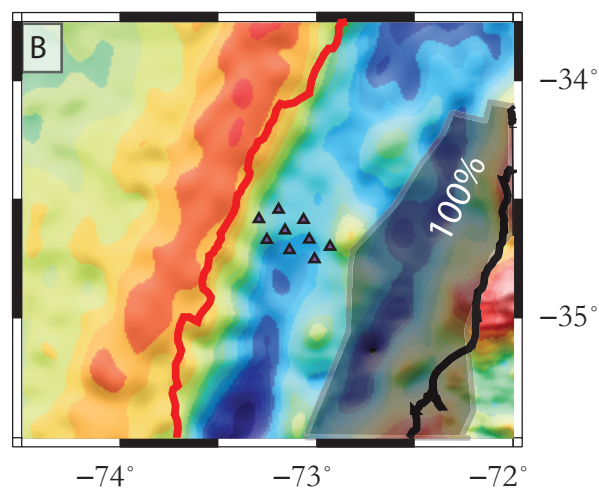


Figure 4-2: a) Original free-air gravity data downloaded from Geomapapp. b) Water column corrected gravity anomaly (see text for details). c) 100 km 2D convolution filter of the water column corrected gravity field that was subtracted from the anomaly in (b)



Complete Gravity Correction

Pre- earthquake Coupling *Metois et al 2012*



Critical taper *Cubas et al 2013*

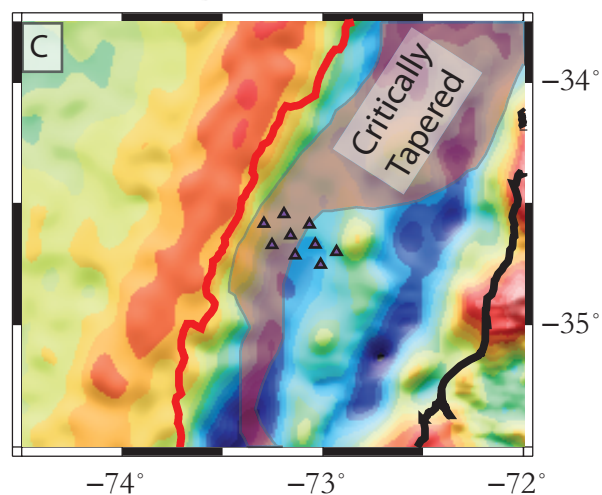


Figure 4-3 A) Terrain and slab corrected bouguer gravity anomalies for the Maule region. The high P-wave velocity feature distinguished by Hicks et al., 2012 correlates to a distinct gravity high extending offshore at 36°S . The proposed obducted seamount at 34.5°S by Maksymowicz et al., (2015) also appears as a 22 mGal anomaly. Similar structures to the proposed seamount are seen in a trench parallel NE-SW trend from 34°S - 35.5°S . Directly down-dip of this feature is the proposed forearc basin, a -25 mGal trench parallel anomaly. B) Coupling from Metois et al (2012) overlain on the corrected gravity data from the ChilePEPPER study area. C) Corrected gravity data overlain by critically taper analysis as described by Cubas et al., (2013). Sections outlined in red are critically tapered while unmasked areas are conditionally stable.

5 DISCUSSION AND CONCLUSIONS

Based on previous studies by *Moscoso et al.*, (2012) and *Lieser* (2015) the outer accretionary wedge remained seismically quiet above the patch of greatest slip for at least eight months after the Maule megathrust event (figure 5-1 a,c). This has previously been interpreted to mean slip did not propagate to the deformation front [*Moscoso et al.*, 2012], a fact that seems to be verified by the analysis of *Cubas et al.*, (2013) demonstrating that the outer wedge is in a critically compressive state. Well-recorded seismicity by the ChilePEPPER array also demonstrates a lack of seismicity occurring within the outer accretionary wedge (figure 5 b,d), with all seismicity occurring either within the outer rise or the paleo-accretionary wedge (critically stable portion of the wedge), meaning that the wedge has not responded in a seismic manner for three years post earthquake. This includes three well located events at or near the plate boundary between the outer wedge, the paleo-accretionary complex and the subducting slab, which show a systematic depth bias in catalog locations (figure 2-7). However, according to dynamic Coulomb wedge theory, the coseismic stress transfer between the down-dip sesimogenic zone and the outer accretionary complex should result in active reverse faulting within the outer wedge. Lack of seismicity in the outer wedge could alternatively be interpreted as the wedge being composed of predominantly velocity strengthening materials that inhibit nucleation of events within the outer wedge. This interpretation is nominally verified by the high V_p/V_s ratio of the outer wedge (figure 2-4) and the poorly formed S-waves recorded on ChilePEPPER instruments. This would then suggest that the dynamic deformation of the outer accretionary wedge is accommodated through alternate methods.

If coseismic stress transfer to the wedge did occur, alternate methods of post-earthquake stress relaxation could include increased pore-pressure with a resultant increase of fluid flow out of the wedge [*LaBonte et al* 2009], or anomalous styles of rupture such as tremor and very low frequency events (VLFs). VLFs have been described as possible mechanisms of interseismic dynamic deformation of the outer wedge in multiple regions of the Japan margin [*Obara et al.*, 2005, *Obana and Kodaira.*, 2009]. The primary interpretation being that increased pore-pressure along pre-existing fractures leads to longer duration ruptures that lack high frequency energy. Band-passing the ChilePEPPER data into typical frequencies associated with these events and manually scanning the data set demonstrated no evidence of ruptures of this type. The only long-period signals recorded by the OBSs were distantly sourced surface waves and the Haida Gwaii tsunami (figure 2-12).

The other method of post-earthquake stress relaxation possible in this section of margin was increased fluid flow at the sediment water interface. Induced fluid flow in the outer wedge in response to seismicity has been demonstrated along the Costa Rican margin with flow rates exceeding 0.1 cm/day [*Desbon et al., 2006*]. However, using the same instruments as those on the Costa Rican margin, flow rates in our study region remained steady at 0.01 cm/yr (figure 2-12), rates three orders of magnitude lower than those measured by *Desbon et al., (2006)*.

The lack of seismicity in the outer wedge, nominal sediment-water interface flow rates and absence of anomalous styles of rupture within the region of our array suggest that there was no coseismic stress state increase within the outer accretionary wedge as was expected based on the model of *Hu and Wang (2006)*. One possible interpretation for this is that no coseismic stress transfer occurred due to slip occurring along a splay fault prior to reaching the outer wedge. However, analysis of high resolution swath bathymetry shows that while splay faulting is prevalent to the north and the south of the study region with fault scarps exceeding 600 m, no evidence of laterally continuous, well developed splay faults can be seen in this region. These lines of evidence suggest that locally, slip propagated through the outer wedge and to the deformation front, an interpretation that may help explain the increased seismicity within the outer rise in this region [*Moscoso et al., 2012*].

Due to a lack of instrumentation along the deformation front and poor resolution of slip models at that distance from the coastline, coseismic slip to the trench (STT) is a poorly understood feature of megathrust subduction zone events. It has been demonstrated that STT does occur from the 2011 M 9.0 Tohoku-Oki earthquake, which showed seafloor uplift of greater than 10 meters which has been interpreted as about 60 m of coseismic slip at the deformation front [*Wang et al., 2015*]. However, along other margins, the accretionary wedge appears to limit the coseismic rupture, with deformation occurring over greater timescales. Post-earthquake stress relaxation in the outer wedge monitored along islands for the 2004 Nias earthquake [*Hsu et al., 2006*] and borehole pressure measurements along both the Costa Rican margin and the Nankai margin, provide evidence for slip halting down dip and deforming during the interseismic [*Davis et al., 2013, Davis et al., 2015*]. The ChilePEPPER array, however, demonstrates that, at least locally, slip likely propagated to the trench coseismically as was suggested by the slip model of *Yue et al., (2014)* (figure 1-4). This has important implications in hazard assessment as it suggests that slip to the trench may not vary at margin scales,

but on much smaller local scales. Local variations for STT may be dependent on the frictional characteristics of the megathrust as determined by the size of the subduction channel and the amount of coseismic slip down-dip of the accretionary wedge.

In the ChilePEPPER study region it was shown that the transition from partial sediment subduction to accretion could vary on the scale of 10 km (figure 3-5). This transition may mark the northern boundary of the outer wedge segment that slipped to the trench during or soon after the main event, releasing strain. However, no data are available to evaluate whether fluid flow signals in response to the Maule earthquake are present north or south of this segment limiting our analysis of the extent of rupture to the deformation front. The thicker subduction channel below the array may act in a velocity-weakening manner at high slip velocities. It has been demonstrated that clay rich fault gouge can propagate significant slip to the trench [Chester *et al.*, 2013]. This is further corroborated by lab experiments of the frictional properties of clays, which show that at high slip velocities, clays demonstrate velocity weakening properties [Faulkner *et al.*, 2011, Ujiie and Tsutsumi, 2010]. Our data suggest that high slip down-dip and STT may be correlated as was demonstrated in the Tohoku-oki earthquake, implying that STT was not an anomalous feature limited to the Japanese margin.

Understanding whether local STT was an anomalous style of rupture for this section of the margin is also an important question to address. Based on the data available, which show different wedge morphologies to the north and south, the rapid transition from sediment subduction to sediment accretion, and the transition from critically stable to critically compressive to the north [Cubas *et al.*, 2013] suggest that this may be a long lived feature. This may be due to the persistence of high slip along the down dip section of the megathrust, a feature that is also likely long lived as is demonstrated by the presence of the trench parallel gravity low seen in the terrain and slab corrected Bouguer anomaly.

In section 4 we presented a refined method for processing offshore free-air gravity data. In order to calculate a topographically corrected Bouguer gravity anomaly (TCBGA) along the continental margin, the effect of all topography within 20 km of the gravity value being corrected must be included in the calculation (Fig 4-1). Similar calculations for residual forearc gravity anomalies have been calculated for this region [Hicks *et al.*, 2012] and highlight similar anomalies in the forearc. The high P-wave velocity structure at -36°S described by Hicks *et al.*, (2012) is

highlighted as a ~ 40 mGal high along the coastline which extends offshore. Additionally, the proposed obducted seamount resolved by *Maksymowicz et al., (2015)* through density modeling of the outer forearc is seen as a ~ 23 mGal high bullseye structure in the TCBGA. However, as shown in figure 4-3, by incorporating a full water column correction our calculated gravity anomaly (compared to the partial correction of *Maksymowicz et al., (2015)*) we highlight smaller scale variations.

As mentioned previously, the primary feature noted is the distinct trench parallel gravity anomaly (TPGA) low associated with the patch of greatest slip (figure 5-2), a feature described in all slip model inversions [e.g. *Moreno et al., 2010, Lin et al., 2013, Yue et al., 2014*] (figure 1-3). We associate this feature with a well-formed forearc basin as has been described throughout circum-Pacific subduction zones [*Wells et al., 2003*]. This interpretation, and the associated high slip patch, is consistent with the findings of *Song and Simons (2003)*, who note that areas within the forearc with strong negative TPGAs correspond to nearly half of the total seismic moment released in subduction zone events $M_w \geq 6.0$. This correlation is attributed to increased shear traction and basal erosion along the plate boundary, depressing the forearc and providing accommodation space for sediment deposition [*Wells et al., 2003*]. The TPGA low correlates directly to the zone of 100% interseismic coupling as described by *Metois et al., (2010)* (figure 4-3) providing a second line of evidence that shear traction along the plate boundary in this area is high. The forearc basin is not a readily apparent feature in either the free air gravity or bathymetric grids, which demonstrates the value of the water column and slab corrections to the free-air gravity data. The magnitude of variation in the gravity field and the presence of a well developed fore-arc basin suggest that this is a long lived feature in this region of the Maule fore-arc and that it is likely that high slip occurs in this region during multiple seismic cycles.

Secondary features noted in the TCBGA are the set of four bullseye gravity highs directly up dip of the trench parallel gravity low. These features, along with the frontal embayments seen in the high-resolution swath bathymetry may be the results of subducting or obducting seamounts (figure 5-3). These features are, at present, poorly understood. However, the fact that slip propagated through this region and was not halted suggests that these are not actively subducting seamounts. The obduction of all or part of the seamount to the front of the paleo –accretionary complex, however, may play a role in localized increased friction along the megathrust leading to these anomalies acting as local asperities, a hypothesis which may help interpretation of seismicity

surrounding the gravity high as seen in figure 5-b. This very localized region may have had increased coseismic slip resulting in a near-field increase of the stress state along the megathrust and increased seismicity along the edge of the asperity. While the effects of actively subducting topography are relatively well understood, as it tends to limit rupture [*Wang and Bilek, 2011, Basset et al., 2015*] the effects of obducted seamounts on the frictional characteristics of the megathrust is a question that remains to be explored. Additionally, their role in the localized segmentation of rupture currently, and active subduction, also poses an interesting research question. Is paleo-subducting topography the cause of the localized heterogeneity in STT in this section of the margin? A detailed plate reconstruction and look at topography on the other side of the Chile Ridge and East Pacific rise may provide insight into this question.

While data drop-outs and instrument failure limited the scope of the work, some important results beyond those previously described were acquired during the ChilePEPPER deployment. Calculating magnitudes of local events surrounding a small aperture array proves difficult due to inconsistent location of the array within P and S wave nodal planes, attenuation of S-wave arrivals due to unconsolidated sediment, and the arrival of the T-phase. However, we demonstrate that with a single onshore station, using band-pass filtered codas can provide stable estimates of earthquake magnitude for events within the accretionary wedge and outer rise, when calibrated to the local magnitude scale (figures 2-11, 2-12). This can be particularly useful for small aperture arrays offshore of poorly instrumented margins.

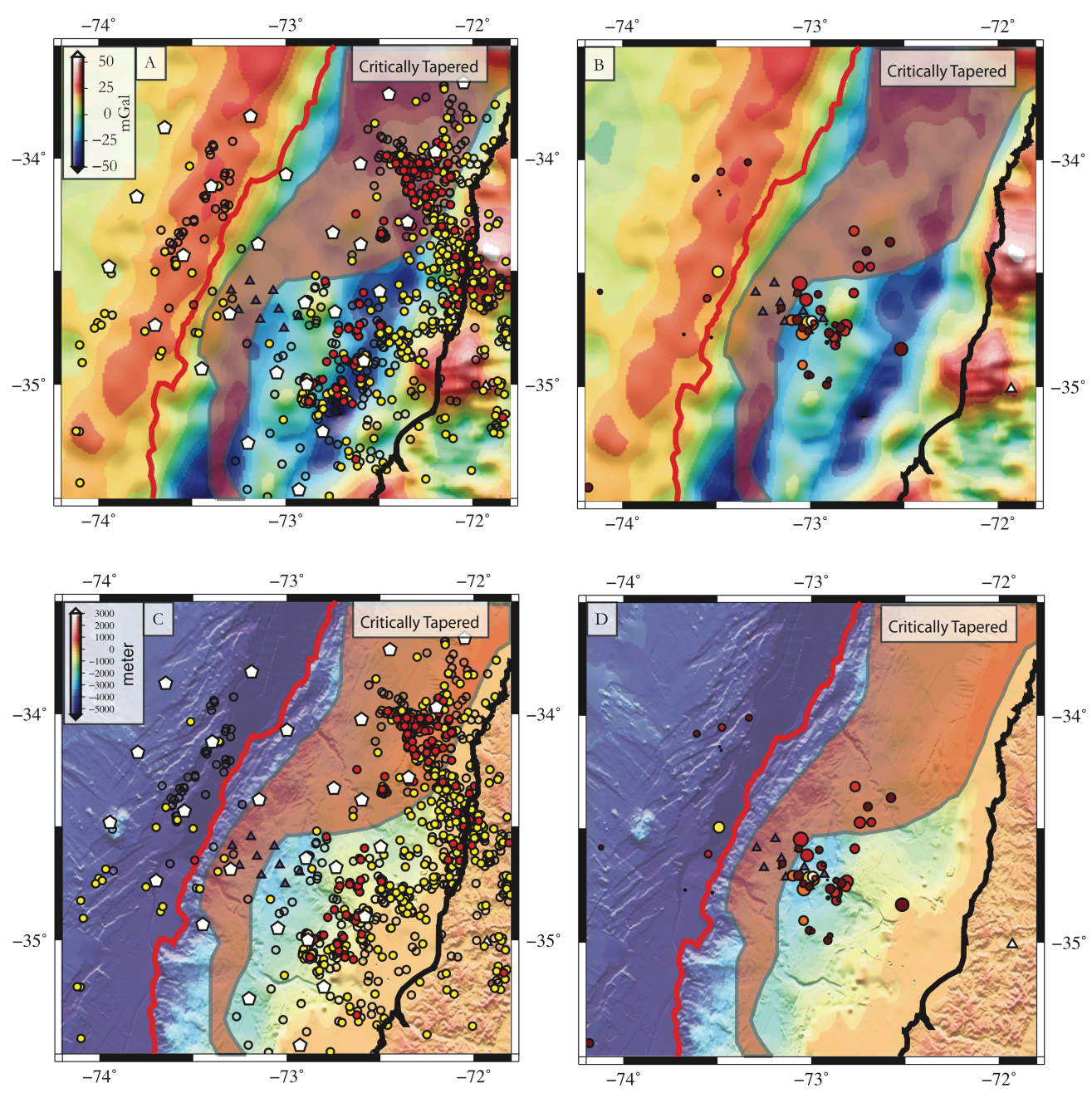


Figure 5-1 Distribution of seismicity from Lieser (2015) on TCBGA (A) and bathymetry (C) with critically tapered sections of the outer accretionary wedge from Cubas et al., (2013) highlighted in red. Distribution of well-located events from ChilePEPPER are shown in figures B and D. White pentagons are the Geomar OBS array used in the Lieser study, Purple triangles are locations of OBS' from the ChilePEPPER array.

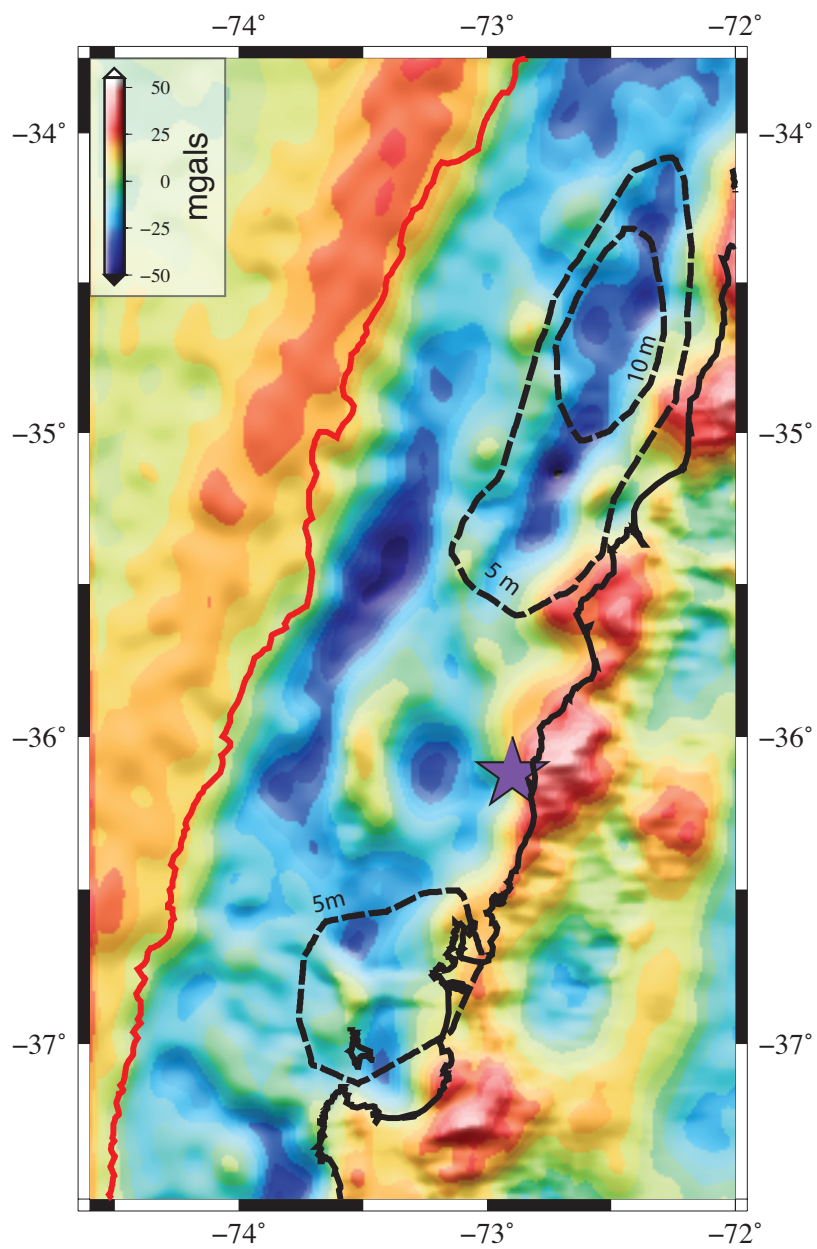


Figure 5-2 Topographically and slab corrected gravity anomalies with overlain slip contours from Moreno et al., (2010). Purple star is the NEIC epicenter.

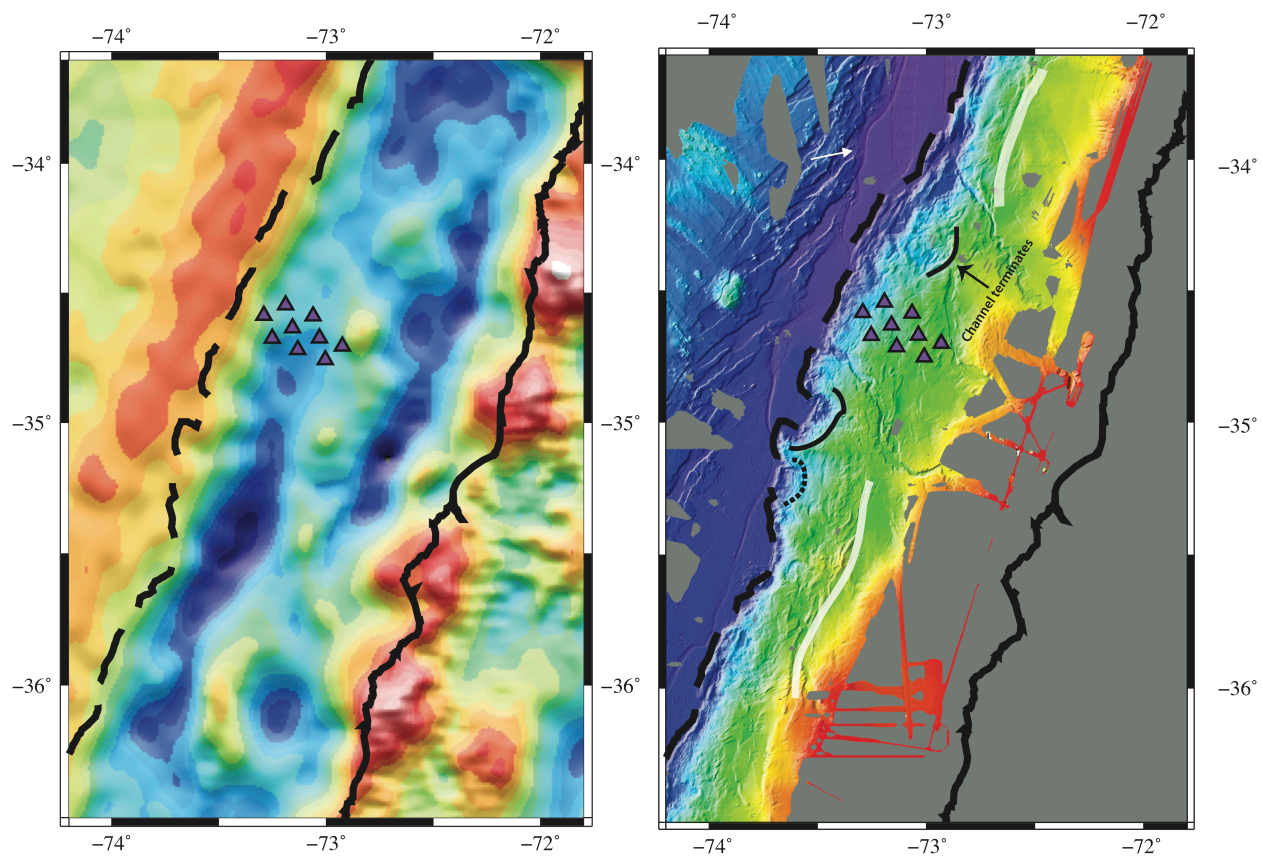


Figure 5-3: Comparison of Complete gravity correction (left) and high resolution swath bathymetry (right).

6 BIBLIOGRAPHY

- Agurto, H., A. Rietbrock, I. Ryder, and M. Miller (2012), Seismic-afterslip characterization of the 2010 *M_w* 8.8 Maule, Chile, earthquake based on moment tensor inversion, *Geophys. Res. Lett.*, *39*, L20303, doi:10.1029/ 2012GL053434.
- Angermann, D., Klotz, J., & Reigber, C. (1999). Space-geodetic estimation of the nazca-south america euler vector. *Earth and Planetary Science Letters*, *171*(3), 329-334.
- Bangs, N.L., and S. C. Cande (1997), Episodic development of a convergent margin inferred from structures and processes along the southern Chile margin, *Tectonics*, *16*(3), 489–503
- Bassett, D., Watts, A., 2015. Gravity anomalies, crustal structure, and seismicity at subduction zones: 1. Seafloor roughness and subducting relief. *Geochemistry, Geophysics, Geosystems*, 2015, **16**, 5, 1541
- Chadwell, C.D., P. Lonsdale, J.W. Kluesner, A.D. Sweeney, W. Weinrebe, J.H. Behrmann, J.L. DiazNaveas, E. Contreras-Reyes, An examination of before and after bathymetry for uplift of the seafloor following the Feb. 27, 2010 Maule, Chile earthquake, Abstract G33A-0851, presented at 2010 Fall Meeting, AGU, San Francisco CA.
- Chester, F., Rowe, C., Ujiie, K., Kirkpatrick, J., Regalla, C., Remitti, F., . . . Toczko, S. (2013). Structure and composition of the plate-boundary slip zone for the 2011 Tohoku-Oki earthquake. *Science* (New York, N.Y.), *342*(6163), 1208-11.
- Campos, J., Hatzfeld, D., Madariaga, R., Lopez, G., Kausel, E., Zollo, A., Iannacone, R., Fromm, R., Barrientos, S., Lyon-Caen, H. (2002). A seismological study of the 1835 seismic gap in south-central Chile. *Physics of the Earth and Planetary Interiors*, *132*(1), 177-195.
- Contardo, X., J. Cembrano, A. Jensen, J. Diaz-Naveas, Tectono-sedimentary evolution of marine slope basins in the Chilean forearc: (33°30' – 36°50'S): Insights into their link with the subduction process, *Tectonophysics*, v. 459, p. 206-218, 2008.
- Contreras-Reyes, E., E. R. Flueh, and I. Grevemeyer (2010), Tectonic control on sediment accretion and subduction off south central Chile: Implications for coseismic rupture processes of the 1960 and 2010 megathrust earthquakes, *Tectonics*, *29*
- Contreras-Reyes, Eduardo, & Carrizo, Daniel. (2011). Control of high oceanic features and subduction channel on earthquake ruptures along the Chile–Peru subduction zone. *Physics of the Earth and Planetary Interiors*, *186*(1), 49-58.
- Comte, D. & Pardo, M., 1991. Reappraisal of great historical earthquakes in the northern Chile and southern Peru seismic gaps, *Nat. Hazards*, *4*(1), 23– 44.

- Cubas, N., Avouac, J.P., Souloumiac, P., Leroy, Y.M., 2013b. Megathrust friction de-termined from mechanical analysis of the forearc in the Maule earthquake area. *Earth Planet. Sci. Lett.* (ISSN0012-821X)381, 92–103. <http://dx.doi.org/10.1016/j.epsl.2013.07.037>.
- Davis, E.E., Kinoshita, M., Wang, K., Asano, Y., Ito, Y., Becker, K., 2013. Episodic deformation and inferred slow slip at the Nankai subduction zone during the first decade of CORK borehole pressure and VLFE monitoring. *Earth Planet. Sci. Lett.* 368, 110–118.
- Davis, E. E., Villinger, H., Sun, T., 2015. Slow and delayed deformation and uplift of the outermost subduction prism following ETS and seismogenic slip events beneath Nicoya Peninsula, Costa Rica. *Earth Planet. Sci. Lett.* 410, 117-127.
- Delouis, B., J-M Nocquet, M. Vallee, Slip distribution of the February 27, 2010 Mw = 8.8 Maule earthquake, central Chile, from static and high-rate GPS, InSAR, and broadband seismic data, *Geophys. Res. Lett.*, v. 37, L17305, 2010.
- Fagereng, A., 2011. Wedge geometry, mechanical strength, and interseismic coupling of the Hikurangi subduction thrust, New Zealand. *Tectonophysics* 507, 26-30. <http://dx.doi.org/10/1016/j.tecto.2011.05.004>.
- Faulkner, D. R., T. M. Mitchell, J. Behnsen, T. Hirose, and T. Shimamoto (2011), Stuck in the mud? Earthquake nucleation and propagation through accretionary forearcs, *Geophys. Res. Lett.*, 38, L18303, doi:[10.1029/2011GL048552](https://doi.org/10.1029/2011GL048552).
- Geersen, J., Ranero, C., Barkhausen, U., Reichert, C., 2015. Subducting seamounts control interplate coupling and seismic rupture in the 2014 Iquique earthquake area. *Nature Communications*, 6:8267. DOI: 10.1038/ncomms9267
- Hashimoto, Y., Tobin, H.J., Knuth, M., and Harada, A., 2011. Data report: compressional and shear wave velocity measurements on sediment in the hanging wall and footwall of megasplay fault, NanTroSEIZE Stage 1. In Kinoshita, M., Tobin, H., Ashi, J., Kimura, G., Lallemand, S., Screaton, E.J., Curewitz, D., Masago, H., Moe, K.T., and the Expedition 314/315/316 Scientists, *Proc. IODP*, 314/315/316: Washington, DC (Integrated Ocean Drilling Program Management International, Inc.). doi:10.2204/iodp.proc.314315316.217.2011
- Hayes, G., E. Bergman, K. Johnson, H. Benz, L. Brown, and A. Meltzer (2013), Seismotectonic framework of the February 27, 2010 Mw 8.8 Maule, Chile earthquake sequence, *Geophys. J. Int.*, 195, 1034–1051, doi:10.1093/ gji/ggt238.
- Hicks, S., A. Rietbrock, C. A. Haberland, I. M. A. Ryder, M. Simons, and A. Tassara (2012), The 2010 Mw 8.8 Maule, Chile earthquake: Nucleation and rupture propagation controlled by a subducted topographic high, *Geophys. Res. Lett.*, 39, L19308, doi:10.1029/ 2012GL053184.
- Kukowski, N., and O. Oncken (2006), Subduction erosion: The “normal” mode of forearc material transfer along the Chilean margin?, in *Frontiers in Earth Sciences*, vol. 3, The Andes: Active Subduction Orogeny, edited by O. Oncken et al., pp. 217–236, Springer, Berlin

- Lallemant, S., Schnurle, P., Malavieille, J., Coulomb theory applied to accretionary and nonaccretionary wedges: Possible causes for tectonic erosion and/or frontal accretion. (1994). *Journal of Geophysical Research: Solid Earth*, 99(B6), 12033-12055.
- Lange, D., F. Tilmann, S. E. Barrientos, E. Contreras- Reyes, P. Methe, M. Moreno, B. Heit, P. Bernard, J.-P. Vilotte, and S. L. Beck (2012), Aftershock seismicity of the 27 February 2010 *Mw* 8.8 Maule Earthquake Rupture Zone, *Earth Planet. Sci. Lett.*, 317–318, 413–425, doi:10.1016/j.epsl.2011.11.034.
- Lay, T., C. J. Ammon, H. Kanamori, K. D. Koper, O. Sufri, and A. R. Hutko (2010), Teleseismic inversion for rupture process of the 27 February 2010 Chile (*Mw* 8.8) earthquake, *Geophys. Res. Lett.*, 37, L13301, doi:10.1029/2010GL043379.
- Lee, W. H., and Lahr, J. C., 1975, HYPO71 (revised; a computer program for determining hypocenter, magnitude, and first motion pattern of local earthquakes: Open-File Report.
- Lin, Y. N. N., et al. (2013), Coseismic and postseismic slip associated with the 2010 Maule Earthquake, Chile: Characterizing the Arauco Peninsula barrier effect, *J. Geophys. Res. Solid Earth*, 118, 3142–3159, doi:10.1002/jgrb.50207.
- Lomnitz, C., 2004. Major earthquakes of Chile: a historical survey, 1535- 1960, *Seism. Res. Lett.*, 75, 368–378
- Lorito, S ; Romano, F ; Atzori, S ; Tong, X ; Avallone, A ; McCloskey, J ; Cocco, M ; Boschi, E ; (2011) Limited overlap between the seismic gap and coseismic slip of the great 2010 Chile earthquake *Nature Geoscience*, Vol.4(3), pp.173-17
- Loveless, J.P., Pritchard, M.E., & Kukowski, N. (2010). Testing mechanisms of subduction zone segmentation and seismogenesis with slip distributions from recent Andean earthquakes. *Tectonophysics*, 495(1), 15-33.
- Maksymowicz, A., Tréhu, A., Contreras-Reyes, E., Ruiz, S., 2015. Density-depth model of the continental wedge at the maximum slip segment of the Maule *Mw*8.8 megathrust earthquake. *Earth Planet. Sci. Lett.* 409, 265–277. <http://dx.doi.org/10.1016/j.epsl.2014.11.005>.
- Maksymowicz, A., The geometry of the Chilean continental wedge: Tectonic segmentation of subduction processes off Chile, *Tectonophysics* (2015), <http://dx.doi.org/10.1016/j.tecto.2015.08.007>
- Metois, M., Socquet, A., Vigny, C., 2012. Interseismic coupling, segmentation and mechanical behavior of the central Chile subduction zone. *J. Geophys. Res.*117, B03406. <http://dx.doi.org/10.1029/2011JB008736>.
- Mix, A.C., Tiedemann, R., Blum, P., et al., 2003. Proc. ODP, Init. Repts., 202: College Station, TX (Ocean Drilling Program).

- Moreno, M., M. Rosenau, and O. Oncken (2010), 2010 Maule earthquake slip correlates with pre-seismic locking of Andean subduction zone, *Nature*, 467, 198–202, doi:10.1038/nature09349.
- Moscoso, E., et al. (2011), Revealing the deep structure and rupture plane of the 2010 Maule, Chile earthquake (Mw=8.8) using wide angle seismic data, *Earth Plan. and Sci. Lett.*, 307, 147-155., doi:10.1016/j.epsl.2011.04.025.
- Pollitz, F. F., et al. (2011), Coseismic slip distribution of the February 27, 2010 Mw 8.8 Maule, Chile earthquake, *Geophys. Res. Lett.*, 38, L09309, doi:10.1029/2010GL047065.
- Pritchard, M.E., Simons, M., 2006. An aseismic slip pulse in northern Chile and alongstrike variations in seismogenic behavior. *Journal of Geophysical Research* 111,B08405.
- Rietbrock, A., I. Ryder, G. Hayes, C. Haberland, D. Comte, S. Roecker, and H. Lyon-Caen (2012), Aftershock seismicity of the 2010 Maule Mw = 8.8, Chile, earthquake: Correlation between co-seismic slip models and aftershock distribution?, *Geophys. Res. Lett.*, 39, L08310, doi:10.1029/2012GL051308.
- Ruegg, J.C. ; Rudloff, A. ; Vigny, C. ; Madariaga, R. ; de Chabalier, J.B. ; Campos, J. ; Kausel, E. ; Barrientos, S. ; Dimitrov, D. (2009). Interseismic strain accumulation measured by GPS in the seismic gap between Constitución and Concepción in Chile. *Physics of the Earth and Planetary Interiors*, 175(1), 78-85.
- Ruff, Larry J. 1989 Do Trench Sediments Affect Great Earthquake Occurrence in Subduction Zones? *PAGEOPH*, Vol. 129, Nos. 1/2
- Russo, R.M., S.L. Beck, A.S. Meltzer, S.W. Roecker, A. M. Reusch, A. Velasco, C. Ebeling, P.M. Bremner, EarthScope participates in open data seismic deployment following 2010 Chile earthquake, in *Sights* (the EarthScope newsletter), winter ,
- Ryan, W.B.F., S.M. Carbotte, J.O. Coplan, S. O'Hara, A. Melkonian, R. Arko, R.A. Weissel, V. Ferrini, A. Goodwillie, F. Nitsche, J. Bonczkowski, and R. Zemsky (2009), Global Multi-Resolution Topography synthesis, *Geochem. Geophys. Geosyst.*, 10, Q03014, doi:[10.1029/2008GC002332](https://doi.org/10.1029/2008GC002332).
- Schnur, S. R., and L. A. Gilbert (2012), Detailed volcanostratigraphy of an accreted seamount: Implications for intraplate seamount formation, *Geochem. Geophys. Geosyst.*, 13, Q0AM05, doi:[10.1029/2012GC004301](https://doi.org/10.1029/2012GC004301).
- Sobiesiak, M.M., Meyer, U., Schmidt, S., Götze, H.J., Krawczyk, C., 2007. Asperity generating upper crustal sources revealed by b-value and isostatic residual anomaly grids in the area of Antofagasta. *J. Geophys. Res.* 112 (B12308) <http://dx.doi.org/10.1029/2006JB004796>.
- Song, T., & Simons, M. (2003). Large trench-parallel gravity variations predict seismogenic behavior in subduction zones. *Science*, 301(5633), 630-633.

- Scherwath, M., et al., (2009), Deep lithospheric structures along the southern central Chile Margin from wide-angle P-wave modelling, *Geophys. J. Int.*, 179, 579–600
- Tong, X., et al. (2010), The 2010 Maule, Chile earthquake: Downdip rupture limit revealed by space geodesy, *Geophys. Res. Lett.*, 37, L24311, doi:10.1029/2010GL045805.
- Tréhu, A., Tryon, M., (2011), Collaborative Research: Post-seismic response updip of the Chilean megathrust earthquake of February 27, 2010. NSF proposal #1129574.
- Tréhu, A., Tryon, M., (2012) Cruise Report R/V Melville MV1206. The 2010 Maule, Chile Earthquake: Project Evaluating Prism Post-Earthquake Response (Chile-PEPPER). <http://www.rvdata.us/catalog/MV1206>.
- Tréhu, A., Blakely, R., Williams, M., 2012. Subducted seamounts and recent earthquakes beneath the central Cascadia forearc, *Geology* 36, 127-130
- Tréhu, A., Braunmiller, J., & Davis, E. (2015). Seismicity of the Central Cascadia Continental Margin near 44.5 degrees N: A Decadal View. *Seismological Research Letters*, 86(3), 819-829.
- Tryon, M., Brown, K., Dorman, L., & Sauter, A., (2001). A new benthic aqueous flux meter for very low to moderate discharge rates. *Deep-Sea Research Part I*, 48(9), 2121-2146.
- Ujiie, K., A. Tsutsumi, and J. Kameda (2011), Reproduction of thermal pressurization and fluidization of clay-rich fault gouges by high-velocity friction experiments and implications in seismic slip in natural faults, *Geol. Soc. Spec. Publ.*, 359, 267–285, doi:[10.1144/SP359.15](https://doi.org/10.1144/SP359.15).
- Vigny, C., et al. (2011), The 2010 Mw 8.8 Maule megathrust earthquake of central Chile, monitored by GPS, *Science*, 332(6036), 1417–1421, doi:10.1126/science.1204132.
- Wang, K., & Hu, Y. (2006). Accretionary prisms in subduction earthquake cycles: The theory of dynamic Coulomb wedge. *Journal of Geophysical Research: Solid Earth*, 111(B6)
- Wang, K., and S. L. Bilek(2014), Invited review paper: Fault creep caused by subduction of rough seafloor relief, *Tectonophysics*, **610**, 1–24.
- Wang, K., and S. L. Bilek(2011), Do subducting seamounts generate or stop large earthquakes?, *Geology*, **39**(9), 819–822.
- Wells, R., Blakely, R., Sugiyama, Y., Scholl, D., & Dinterman, P. (2003). Basin-centered asperities in great subduction zone earthquakes: A link between slip, subsidence, and subduction erosion? *Journal of Geophysical Research: Solid Earth*, 108(B10)
- Williams, M. (2011). Seismicity at the Cascadia plate boundary beneath the Oregon continental shelf. Corvallis, Or.: Oregon State University.

Yue, H., Lay, T., Rivera, L., An, C., Vigny, C., Tong, X., & Bález Soto, J. (2014). Localized fault slip to the trench in the 2010 Maule, Chile $M_w = 8.8$ earthquake from joint inversion of high-rate GPS, teleseismic body waves, InSAR, campaign GPS, and tsunami observations. *Journal of Geophysical Research: Solid Earth*, *119*(10), 7786-7804.

7 APPENDIX A

Here we present some examples of seismicity as observed on the ChilePEPPER array to highlight typical waveforms and show some of the issues with instrumentation that occurred during deployment. Figure 7-1 shows two events that occurred on October 27th that had not been described in either the Chilean or ANSS catalogs. Here we show the vertical components of the SL-OBS sites and the APGs for the CI-OBS stations. As described previously, the APGs only recorded well below 2 Hz, therefore only recording large local and teleseismic events. Additionally, waveform distortion and offsets can be seen at stations CP06 and CP07. While both stations are functioning at this point the signal deteriorates with time as is shown in figure 7-2. With only four stations recording for most small local events, acquiring an adequate number of picks for a location with reasonable uncertainty prove difficult. Four picks are needed for any location and to constrain depth, S-wave arrivals are needed.

Figure 7-3 shows a well-recorded event at station CP08 with a strong impulsive P-arrival and well-formed S-wave. Arrivals were hand picked to minimize uncertainty and a qualitative analysis of pick error was applied to each arrival. When picks were imported into the hypocentral location program Hypo71, picks could be given a weight of 1-4 (or 100% - 0% in increments of 25%). Figure 7-3 shows an event with 100% weighting applied to the P-arrival, which has an error of < 0.1 s. Due to uncertainty in S-arrivals, the maximum weighting applied to S picks is 75%. Picking S-arrivals is further complicated by attenuation within the accretionary prism as seen in figure 7-4 (discussed in 3.1.3).

P-wave arrivals for the M_b 4.7 September 15th event as seen on the APGs are shown in figure 7-5. The proximity and magnitude of this event provided enough energy to rise above the noise level for these instruments. Unfortunately, stations CP02 and CP03 had stopped functioning completely at this point and provided no useful data towards event locations.

Figures 7-6 and 7-7 provide examples of earthquakes that do, and do not, excite T-phases. Figure 7-8 show the frequency spectra for different sections of the earthquake shown in figure 7-6. Note that while the T-phase contains more high frequency energy the spectra for just the earthquake (7-8c) and the for the earthquake including the T-phase (7-8a) look virtually identical. This means that for earthquakes that are located closer to the array where the T-phase and the S-wave coda may

overlap, we cannot distinguish the T-phase by filtering the data or looking at the frequency spectrum.

Figure 7-9 gives an example of a distantly sourced Rayleigh wave, which can be seen in the frequency range of Very Low Frequency earthquakes. This is discussed in section 3.1.6. Figures 7-10 and 7-11 show two events from the September 15th sequence to highlight differences in waveforms between the 00:40 event which has a normal faulting mechanism and the 00:50 event which has a shallow thrust fault mechanism.

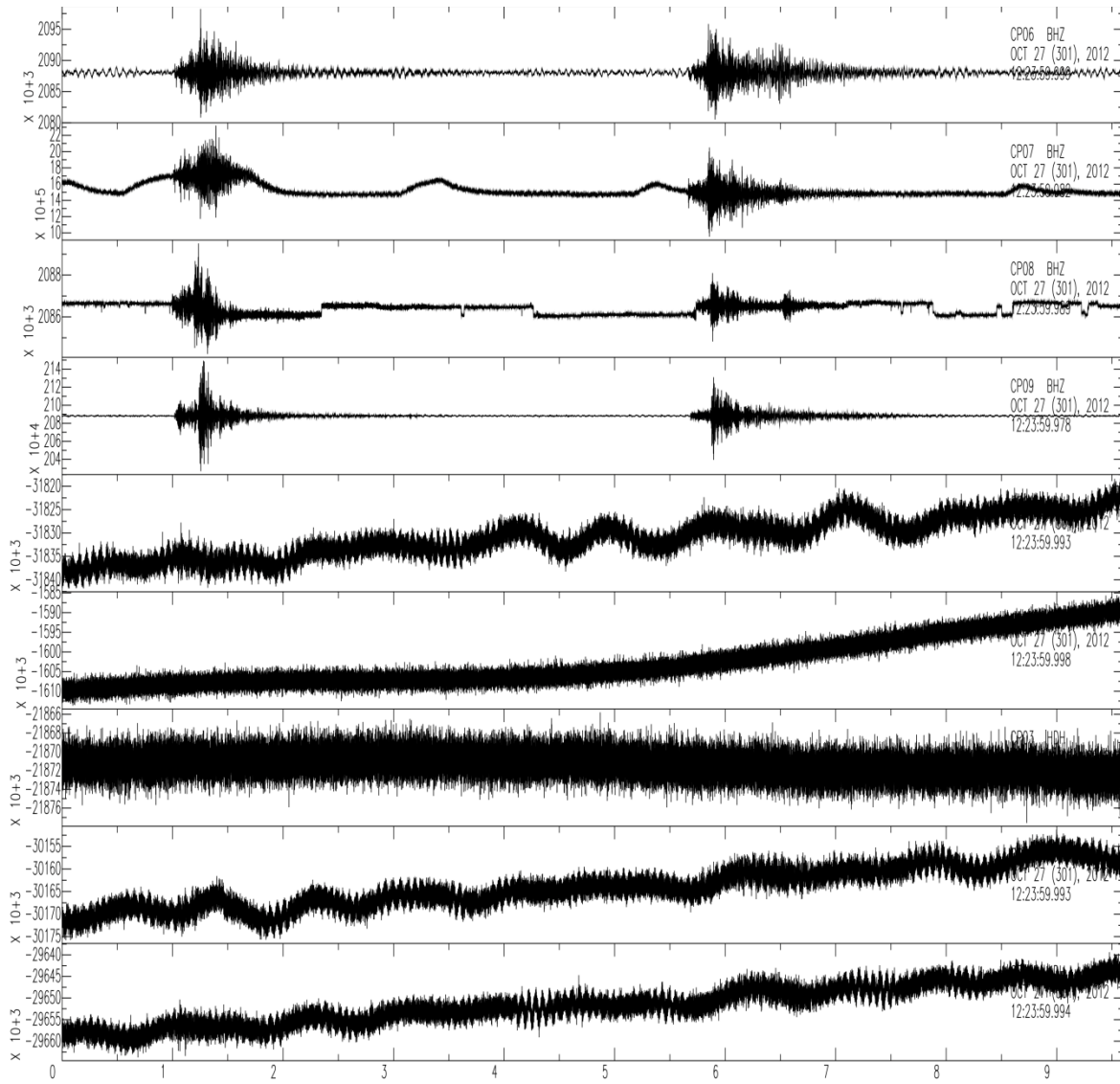


Figure 7-1 Two events $> M_{\text{coda}} 3$ recorded on the ChilePEPPER array not previously described in the Chilean seismic bulletin. As we can see, events are not recorded on the APGs (bottom five panels) due to only recording well below 2 Hz and therefore only recording the largest events. Distortions in the waveforms of CP07 and offsets in CP08 are common and become more prevalent throughout the deployment resulting in unusable data for sections of time.

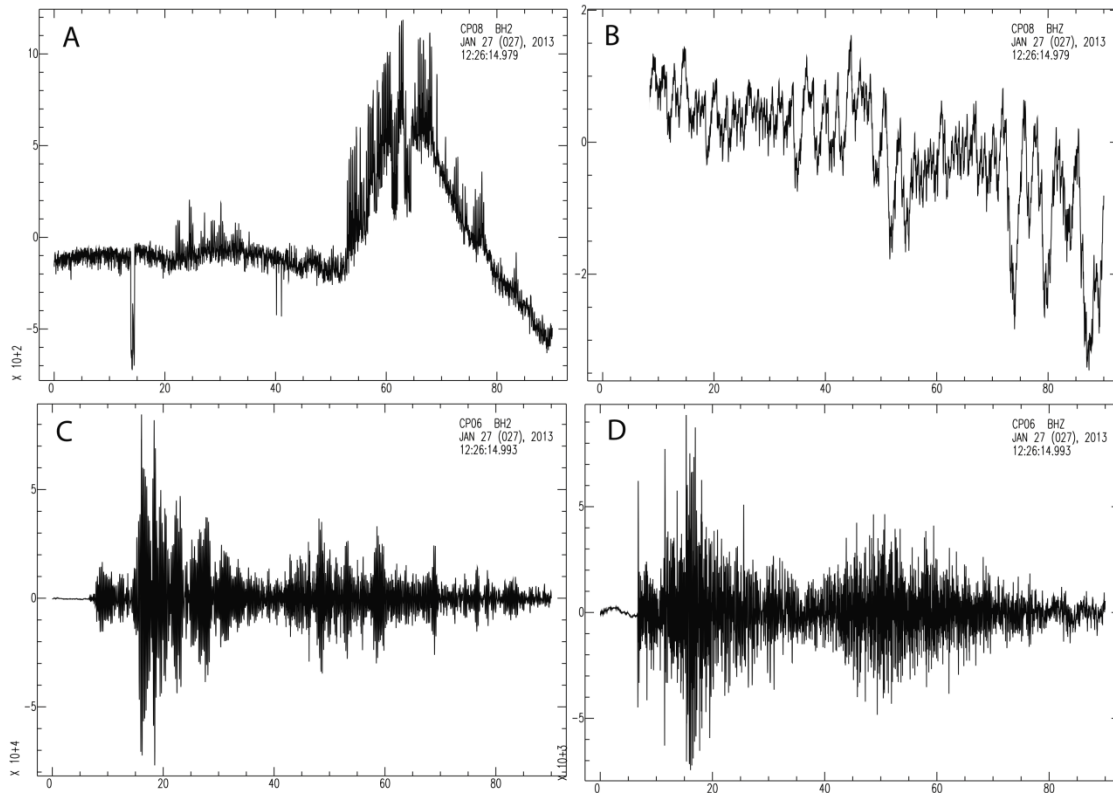


Figure 7-2 Signal quality problems at site CP08 on the horizontal (A) and vertical (B) components during an event occurring on Jan 27. (C) and (D) is the same event recorded on CP06. While data dropouts like this are common throughout the deployment, data quality tends to deteriorate with time.

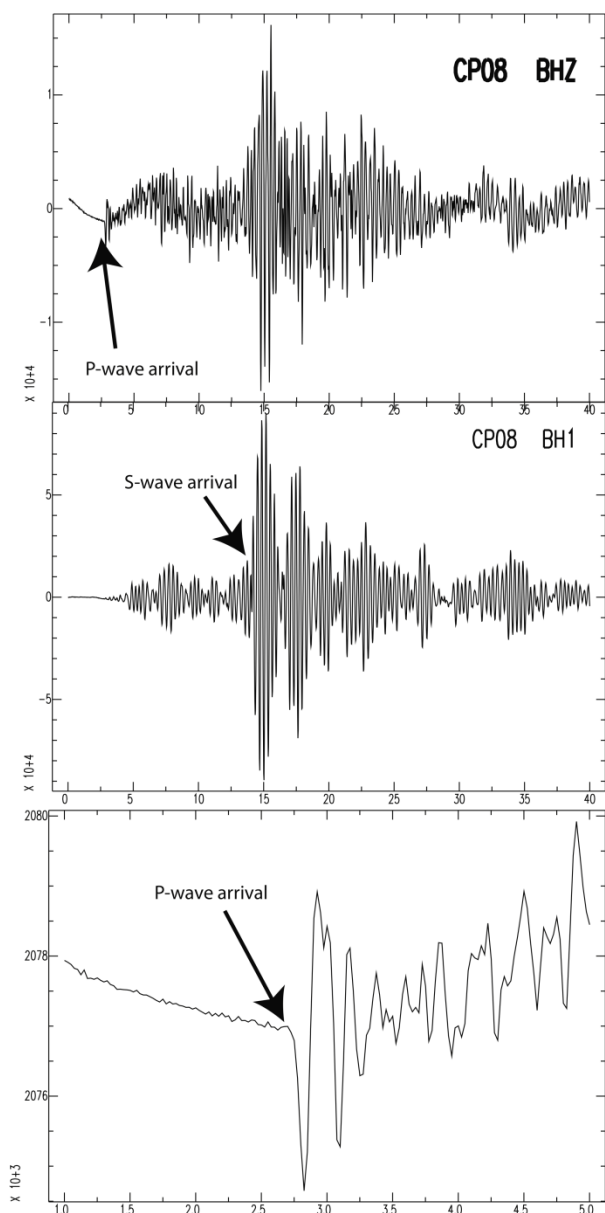


Figure 7-3 Showing P and S-wave arrivals at station CP08. P-picks are made on the vertical component (BHZ) because compressive wave are more impulsive in the Z direction while S-waves are first seen on horizontal components (BH1).

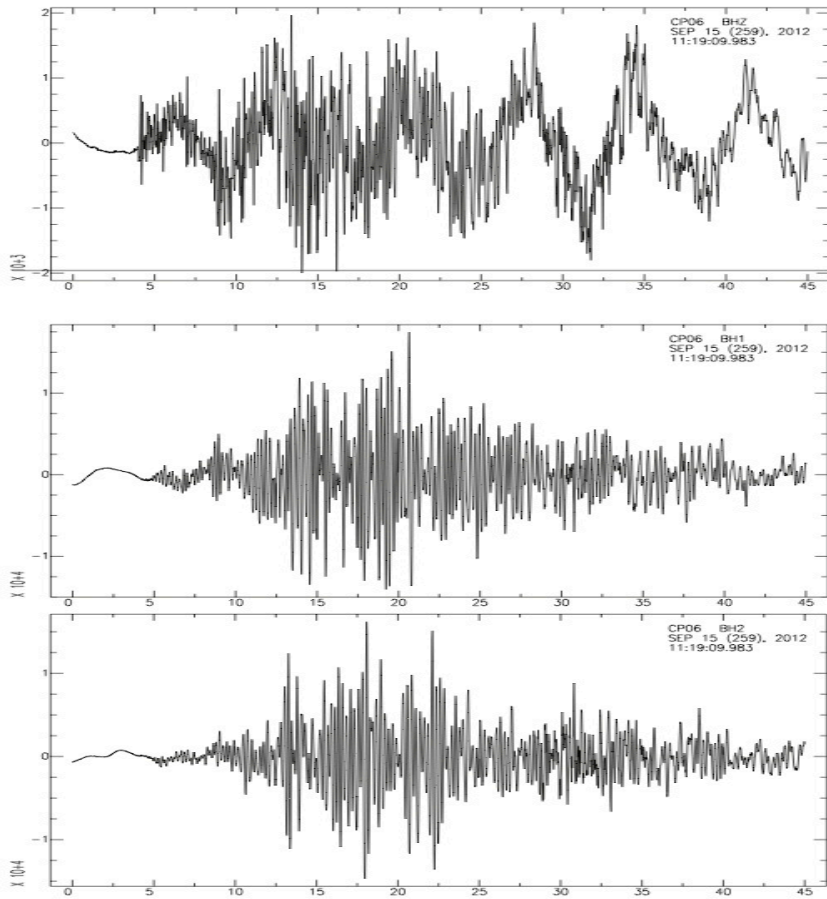


Figure 7-4 Event on September 15th recorded at station CP06. This figure highlights issues with picking *S*-wave arrivals for small events within the accretionary prism. We interpret that highly saturated sediments attenuate *S*-wave arrivals (as shown from the V_p/V_s ratio, section 3.1.3).

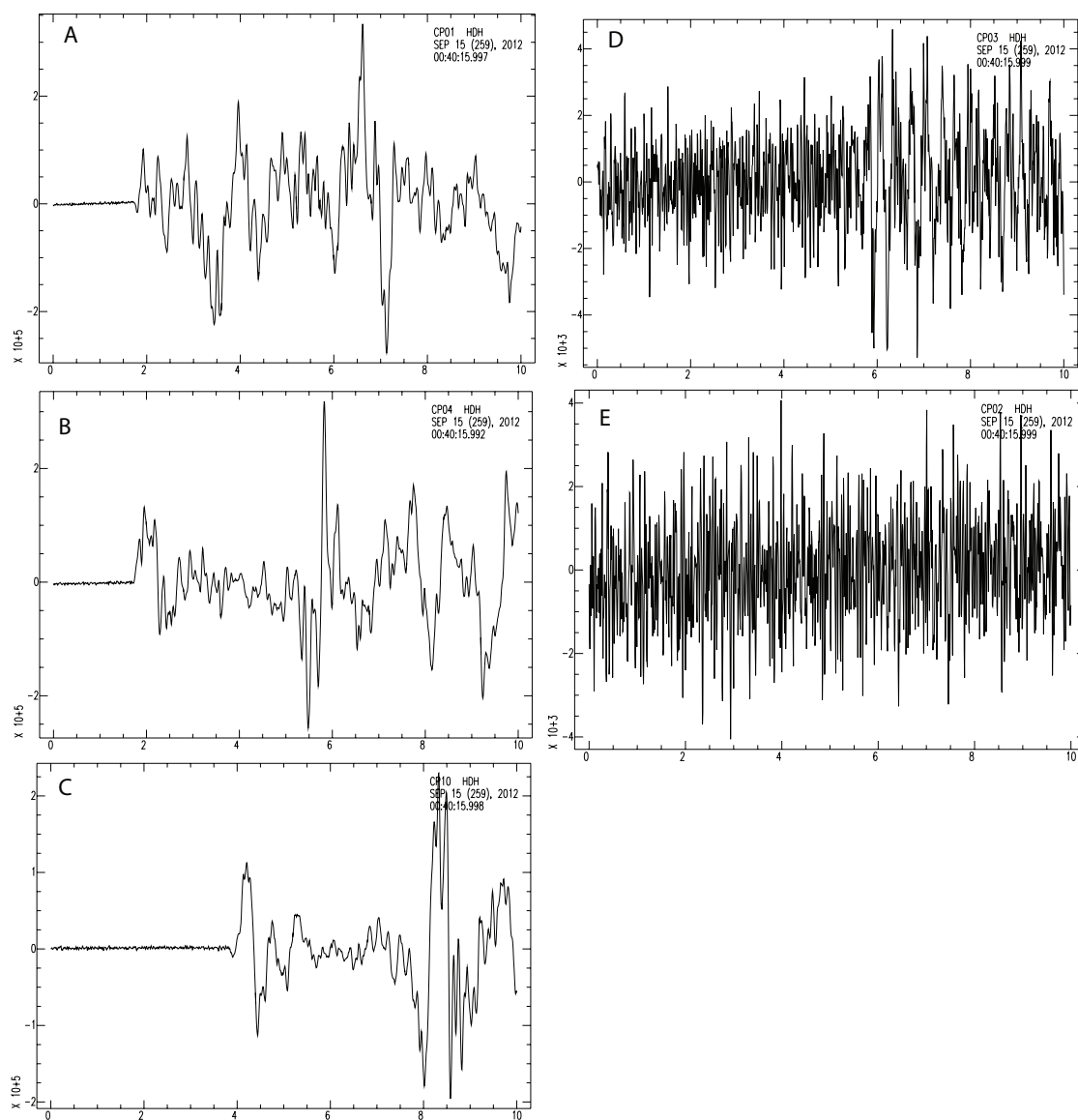


Figure 7-5 P-wave arrivals for September 15th Mb 4.7 event on all APGs. At this stage CP02 (D) and CP03 (E) had stopped functioning even below 2 Hz. Time is measured relative to the time listed in the upper right of each panel

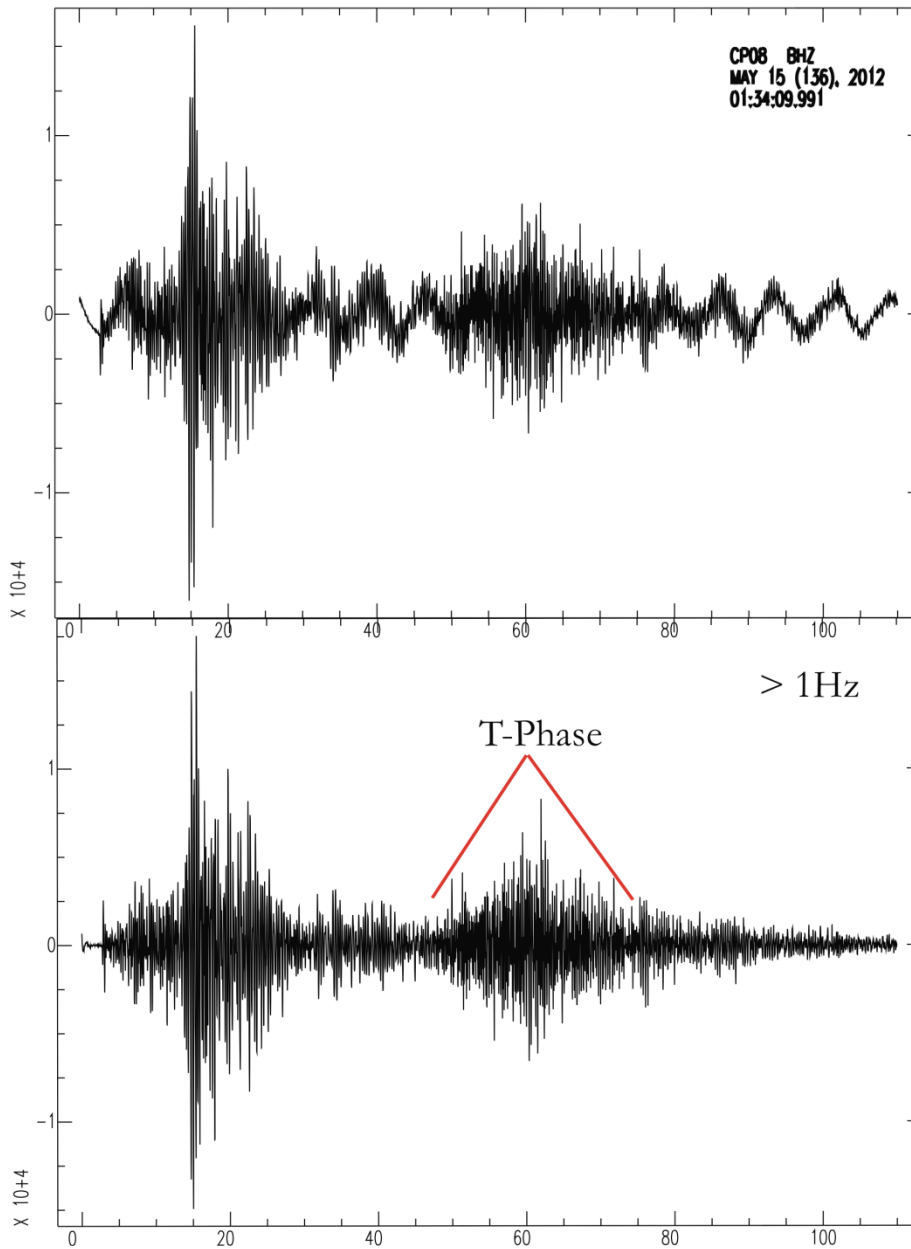


Figure 7-6 Typical waveform of event located in the outer rise that excites a high frequency T-phase. To propagate efficiently in the SOFAR channel T-phases contain high frequency energy and are generally composed of frequencies above 3 Hz. Here the waveform has been high pass filtered at 1 Hz showing a typical t-phase arrival. T-phases arrive at instruments after the P and S waves because slower acoustic velocities in water than in consolidated materials.

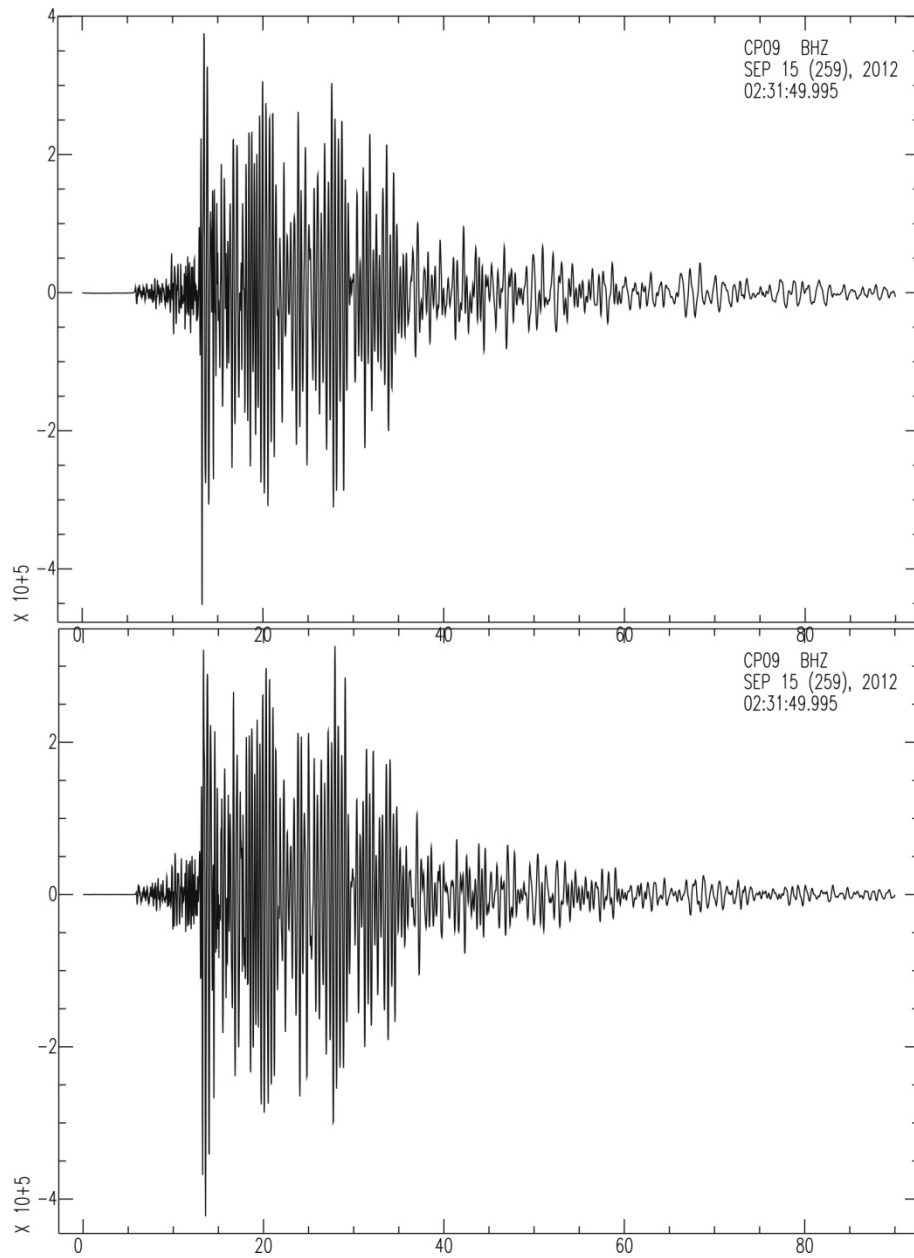


Figure 7-7 M_L 3.4 event located below the ChilePEPPER array. Top panel unfiltered data. Bottom panel high-pass filtered at 1Hz (same as previous figure). This event shows no evidence of T-phase excitation.

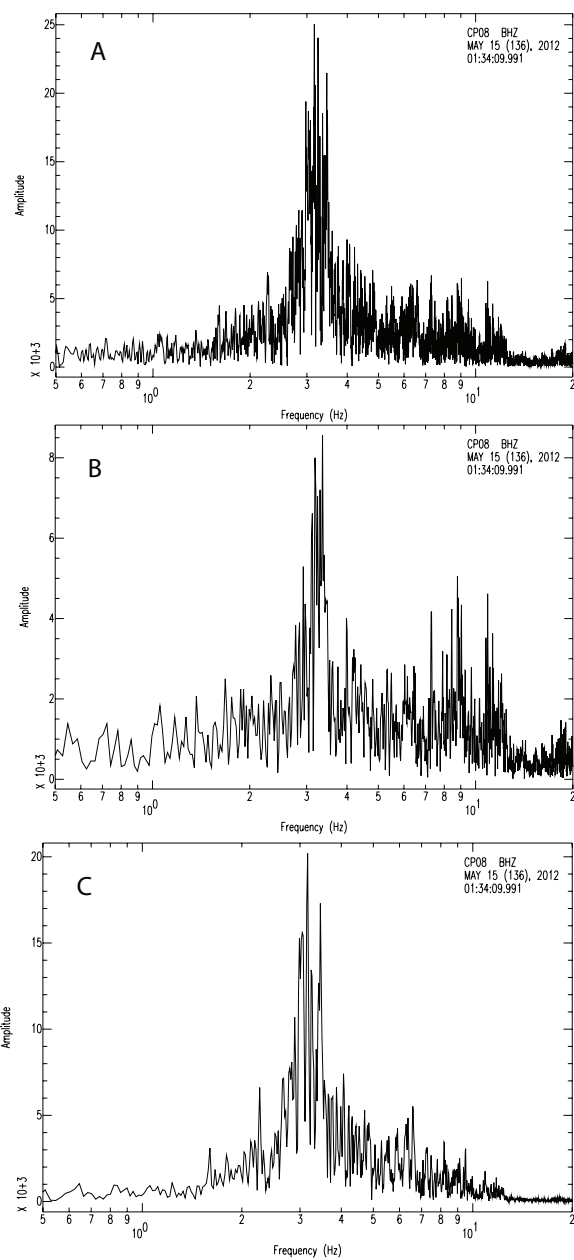


Figure 7-8 Spectrum from earthquake shown in figure 7-6. A) shows the spectrum of the entire earthquake including the T-phase. B) Shows just the spectrum of the T-phase. C) shows spectrum of the earthquake without the T-phase.

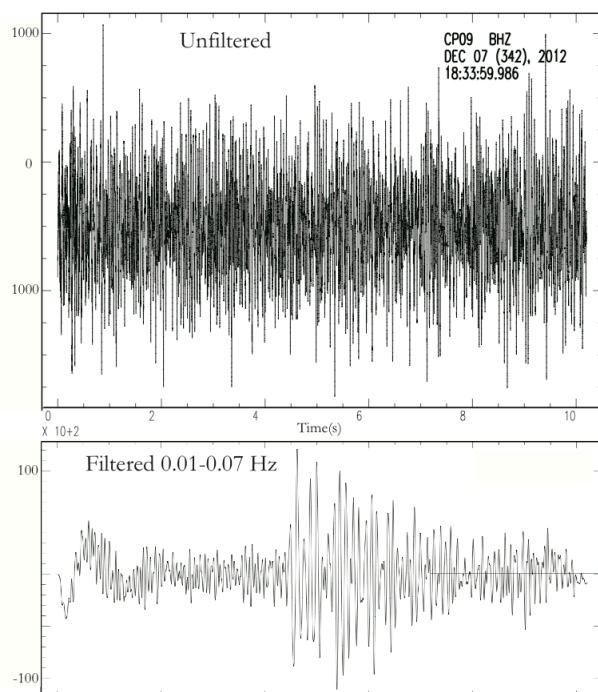


Figure 7-9 Example of distantly sourced Rayleigh waves from a M4.7 event in Tonga at the same frequency band of Very Low Frequency events.

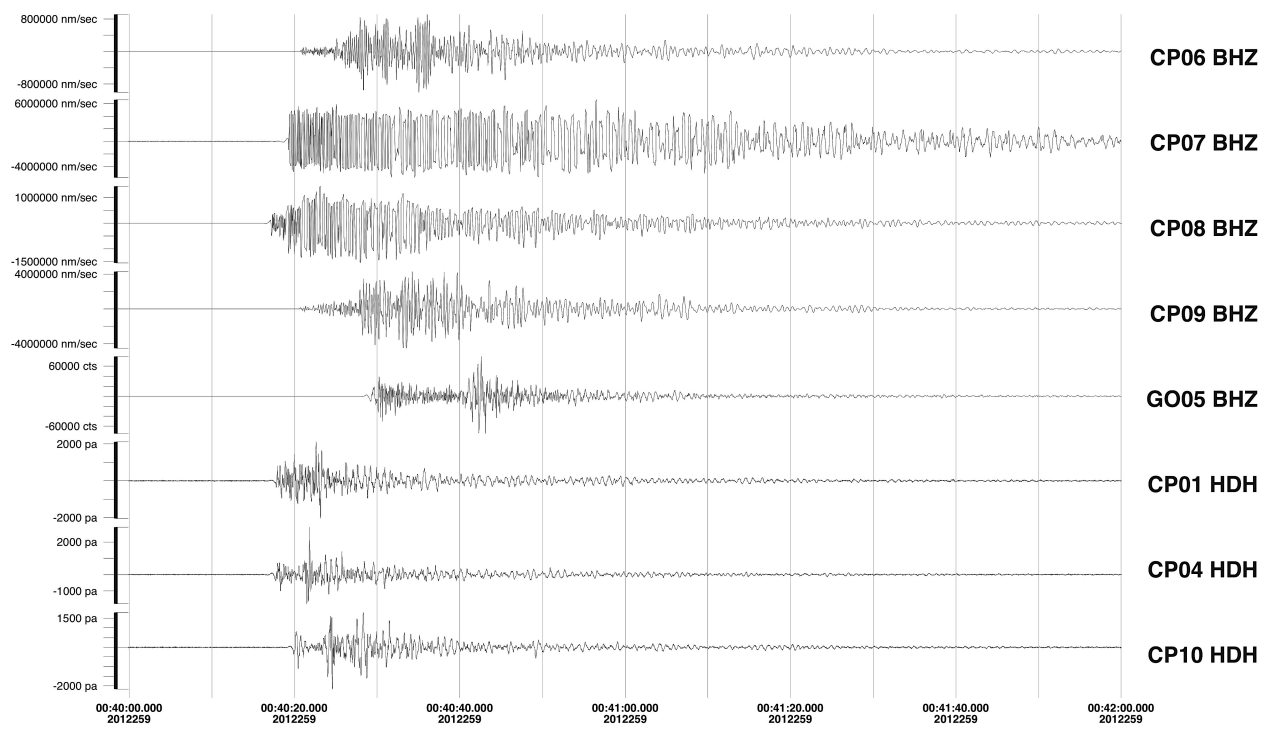


Figure 7-10: Vertical components and APG recordings of September 15th 00:40 event low-pass filtered at 1Hz

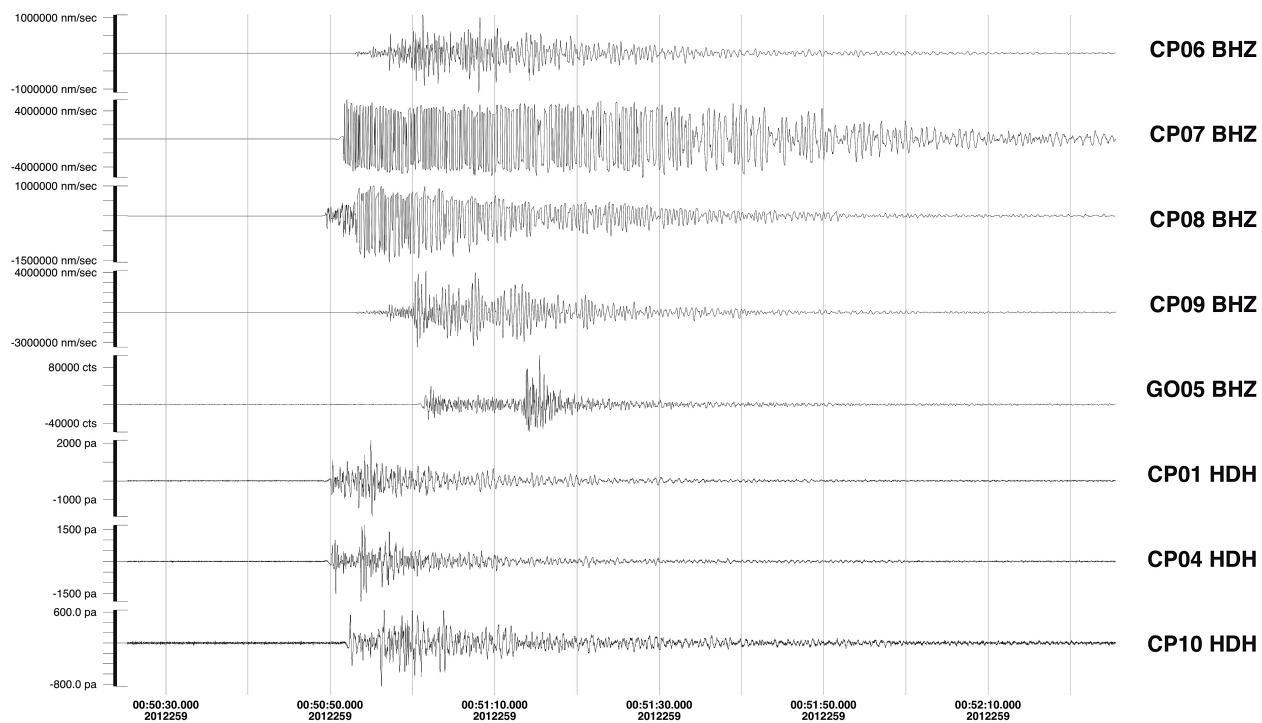


Figure 7-11 Vertical components and APG recordings of September 15th 00:50 event low-pass filtered at 1Hz

8 APPENDIX B

Date (yymmdd)	Time	Latitude	Longitude	Coda Length Magnitude
120620	5:30	-34.61233333	-74.13316667	3.693709958
120620	6:32	-34.69616667	-72.82083333	3.889530622
120620	13:58	-34.63983333	-73.95433333	1.916712784
120622	12:32	-34.57233333	-73.26483333	2.431686592
120625	22:33	-34.6595	-73.9425	2.276107754
120627	9:38	-35.06016667	-73.89183333	1.992887508
120706	15:13	-34.56883333	-73.3	
120707	6:49	-34.56083333	-73.19966667	
120707	20:00	-34.08166667	-73.47633333	
120715	9:37	-34.565	-73.19416667	
120717	14:36	-34.30066667	-73.73183333	1.141888209
120720	8:24	-34.55883333	-74.05	2.124359632
120720	4:43	-34.616	-73.46483333	1.621272376
120724	5:33	-34.583	-74.12083333	1.477726406
120728	7:22	-34.56183333	-72.90033333	2.624992634
120729	9:35	-34.63333333	-73.91383333	1.421675497
120730	21:47	-34.5695	-73.26383333	
120730	21:47	-34.5695	-73.26383333	
120805	13:57	-34.63683333	-74.06933333	
120807	11:44	-34.098	-73.50283333	0.777860592
120808	8:49	-34.01233333	-73.33283333	2.124359696
120809	21:06	-34.57866667	-73.2805	
120811	1:43	-34.60283333	-73.87516667	2.456691561
120813	15:59	-34.90083333	-73.13733333	4.594698369
120818	5:27	-34.231	-73.74266667	2.081306855
120822	12:19	-34.8505	-73.15716667	2.951184831
120825	8:33	-34.581	-73.28516667	
120826	7:20	-34.60466667	-73.17833333	
120827	20:10	-34.54733333	-73.19416667	
120830	6:01	-34.84616667	-73.15366667	3.521841065
120901	15:44	-34.58183333	-73.84033333	1.822096961
120909	9:36	-34.53766667	-73.98616667	1.932136377
120911	18:52	-34.60833333	-73.75016667	3.202816907
120923	9:16	-34.54733333	-73.19416667	
120924	5:58	-34.46233333	-74.04733333	-0.201470055
120925	13:41	-34.13133333	-73.66316667	
120925	22:34	-33.87083333	-73.33533333	2.289452664
120925	19:40	-34.47016667	-74.044	
121004	15:07	-34.91	-74.19416667	
121011	2:38	-34.31366667	-72.69016667	4.02520725
121014	17:34	-33.997	-73.5865	
121014	10:50	-35.3455	-74.26866667	
121015	22:24	-34.53566667	-73.8025	
121110	9:06	-34.675	-73.9095	1.992887345
121113	16:09	-34.5725	-73.83583333	1.962698347

Date (yymmdd)	Time	Latitude	Longitude	Coda Length Magnitude
121114	1:01	-34.59166667	-73.87266667	2.066787878
121114	00:35	-34.155	-73.4795	0.519764625
121120	22:04	-34.08233333	-73.61083333	2.208282305
121120	23:35	-34.07416667	-73.6315	0.321620638
121130	14:05	-34.964	-73.25583333	1.477726177
121130	20:40	-34.4895	-73.65083333	-0.470391416
121207	20:40	-34.64016667	-73.94633333	
121207	7:11	-34.97933333	-73.19416667	0.802249968
121209	7:08	-33.9445	-73.658	1.977838984
121210	00:05	-34.4345	-73.9575	2.110091681
121218	20:29	-34.5275	-74.0025	
121220	1:48	-34.63366667	-73.95266667	1.141888472
121222	14:51	-34.68383333	-74.17083333	1.789737503
121223	8:07	-34.3955	-74.056	1.838119731
121227	2:51	-34.9625	-73.2185	3.447940683
130102	19:14	-34.53766667	-73.83766667	
130102	1:07	-33.94866667	-73.91933333	1.099206551
130102	18:09	-35.86166667	-73.52933333	3.137546416
130104	9:17	-34.7845	-74.13183333	2.249200259
130111	13:09	-34.72166667	-73.76333333	1.901192635
130112	12:41	-33.99766667	-73.43316667	2.235635916
130113	5:50	-34.90283333	-74.4145	3.985279344
130117	22:54	-33.9405	-73.40083333	3.640307626
130120	21:26	-34.481	-73.98583333	-0.351545479
130121	1:21	-34.57733333	-73.29866667	
130124	12:40	-33.3525	-73.3785	
130127	2:24	-34.211	-73.54416667	2.329061289
130127	21:19	-34.98716667	-73.48466667	2.951184659
130129	15:40	-34.60216667	-73.96866667	2.951184785
130203	8:29	-33.91416667	-73.4095	
130211	16:54	-34.0675	-73.61533333	
130222	1:46	-34.40983333	-73.66083333	
130223	15:57	-34.07216667	-73.529	
130224	11:20	-34.41283333	-73.69466667	
130225	00:56	-34.40233333	-73.872	
130301	3:27	-34.48916667	-74.00416667	
130302	17:05	-34.23583333	-73.648	1.992887345
130303	5:52	-34.89866667	-74.131	3.041212124
130305	14:04	-34.03333333	-73.51116667	

Table 8-1: List of all events with identifiable T-phases seen in ChilePEPPER data set.

9 APPENDIX C

VLFE date	Time	Rayleigh location	Time	Lat	Lon	Δ Degree	Mag	
<u>June</u>								
2012 153	5:30	Antarctica	5:07	-77.0	-148.8	53.3	5.5	
2012 156	1:00	Panama	0:45	5.30	-82.6	40.8	6.3	
2012 156	3:30	Panama	3:15	5.50	-82.5	40.8	6.3	
2012 169	21:40	N. Japan	20:32	38.9	141.8	151	6.4	
<u>July</u>								
2012 190	12:40	Kuril	11:33	45.4	151.2	144	6	
2012 193	21:00	S. Peru	20:52	-15.2	-75.2	19.3	5.6	
2012 207	12:15	Solomon Is	11:20	-9.6	159.7	113.3	6.4	
2012 208	6:30	Mauritius	5:33	-17.5	66.3	115.1	6.7	
2012 211	12:45	Guatemala	12:22	14.1	-92.2	52.0	5.9	
<u>August</u>								
2012 223	19:30	Aleutian Is.	18:37	52.6	-167.4	119.32	6.2	
2012 224	13:30	Iran	12:34	38.3	46.74	132.23	6.3	
2012 231	10:50	Indonesia	9:41	-1.3	120.0	142.1	6.3	
2012 239	15:20	Japan	14:30	37.0	142.3	119.52	4.4	
<u>September</u>								
2012 247	19:37	NO RELATED EVENT						
2012 250	23:53	Japan	23:33	-4.6	-105.8	42.5	5.8	
2012 270	0:18	Mexico	23:45	24.6	-110.1	68.8	6.3	
2012 271	0:38	Alaska	23:39	51.5	-178.2	125.2	6.4	
<u>October</u>								
2012 282	1:53	Chile	1:50	-21.7	-68.1	13.5	5.8	
2012 282	7:03	California	6:26	25.1	-109.5	68.9	6	
2012 286	0:50	Papua	00:31	-4.9	134.0	132.9	6.6	
2012 294	23:49	Vanuatu	23:00	-13.5	166.5	105.6	6.2	
2012 298	0:54	Costa Rica	00:45	10.1	-85.3	46.2	6.5	
2012 302	3:18	Haida Gwaii	03:04	52.8	-132.1	101.3	7.8	
<u>November</u>								
2012 315	15:08	Peru	14:57	-8.8	-75.0	6		
2012 316	2:30	Myanmar	01:32	22.6	95.8	4.9		
2012 316	22:24	Guatemala	22:14	14.1	-92.1	6.5		
2012 316	22:31	Guatemala	22:21	14.1	-92.1	6.5		

2012 316	22:39	Guatemala	22:28	14.1	-92.1	6.5
2012 317	11:02	Chile	10:55	-45.9	-76.9	4.7
2012 317	21:10	Japan	20:00	36.1	142.4	4.9
2012 321	19:20	Kuril Islands	18:12	49.2	155.4	6.5
2012 330	22:17	Chile	22:11	-44.3	-77.7	4.8
2012 331	0:36	EPR	0:17	-9.0	-108.3	5.5
2012 334	7:22	Peru	7:09	-6.5	-80.9	5.5
2012 334	20:00	Guatemala	19:32	13.7	-92.1	5.5
<u>December</u>						
2012 336	13:19	Easter Island	13:04	-30.1	-111.2	4.6
2012 337	1:43	Vanuatu	0:54	-16.9	167.6	6.2
2012 342	18:41	Tonga	17:51	-15.9	-173.8	4.7
2012 349	10:48	Vanuatu	9:55	-19.0	169.5	4.7
2012 352	17:55	EPR	17:41	-4.1	-104.4	5.9
2012 352	18:01	EPR	17:46	-3.9	-104.0	5.7
<u>January</u>						
2013 005	9:15	MIR	8:27	-15.0	67.0	4.7
2013 015	16:27	PAR	16:09	-62.5	-161.4	6.1
2013 023	4:43	EPR	4:29	-34.6	-109.1	5.1

Table 9-1 Table describing where in the dataset VLF waveforms were seen. All but one could be associated with distantly sourced earthquakes and their associated rayleigh waves. Table shows time that rayleigh waves arrived at the stations and the associated earthquake.